2012-11-08

A Hybrid Bishop-Hill Model for Microstructure Sensitive Design

Ribeka Takahashi
Brigham Young University - Provo

A Hybrid Bishop-Hill Model for Microstructure Sensitive Design

Ribeka Takahashi

A dissertation submitted to the faculty of
Brigham Young University
in partial fulfillment of the requirements for the degree of

Doctor of Philosophy

David T. Fullwood, Chair
Christopher A. Mattson
Larry L. Howell
Carl D. Sorensen
Eric R. Homer

Department of Mechanical Engineering

Brigham Young University

November 2012

ABSTRACT

A Hybrid Bishop-Hill Model for Microstructure Sensitive Design

Ribeka Takahashi
Department of Mechanical Engineering, BYU
Doctor of Philosophy

A method is presented for adapting the classical Bishop-Hill model to the requirements of elastic/yield-limited design in metals of arbitrary crystallographic texture. The proposed Hybrid Bishop-Hill (HBH) model, which will be applied to ductile FCC metals, retains the 'stress corners' of the polyhedral Bishop-Hill yield surface. However, it replaces the 'maximum work criterion' with a criterion that minimizes the Euclidean distance between the applicable local corner stress state and the macroscopic stress state. This compromise leads to a model that is much more accessible to yield-limited design problems. Demonstration of performance for the HBH model is presented for an extensive database for oxygen free electronic (OFE) copper. The study also implements the HBH model to the polycrystalline yield surface via standard finite element analysis (FEA) tools to carry out microstructure-sensitive design. Anisotropic elastic properties are incorporated into the FEA software, as defined by the sample texture. The derived local stress tensor is assessed using the HBH approach to determine a safety factor relating to the distance from the yield surface, and thereby highlighting vulnerable spots in the component and obtaining a quantitative ranking for suitability of the given design. By following standard inverse design techniques, an ideal microstructure (meaning texture in this context) may be arrived at. The design problems considered is a hole-in-plate configuration of sheets loaded in uniaxial tension and simple compliant mechanisms.

The further improvement of HBH model is discussed by introducing geometrically necessary dislocation (GND) densities in addition to the crystal orientations procedure in standard microstructure-based method. The correlations between crystal orientations and GND densities are studied. The shape of the yield surface most influenced by the texture of the material, while the volume of the envelope scales in accordance with the GND density. However, correlations between crystal orientation and GND content modify the yield surface shape and size. While correlations between GND density and crystal orientation are not strong for most copper samples, there are sufficient dependencies to demonstrate the benefits of the detailed four-parameter model. The four-parameter approach has potential for improving estimates of elastic-yield limit in all polycrystalline FCC materials.

Keywords: Bishop-Hill model, microstructure, FCC metals, elastic/plastic yield limit, design space, stress, yield surface, OFE copper

ACKNOWLEDGMENTS

This project is completed with help from many individuals and I would like to express my appreciation for all those who have helped and inspired me throughout the research.

I would like to express my gratitude to my advisor Dr. David T. Fullwood for his support and his guidance on my research. His patience, devotion and guidance on even the small steps on the research made it possible for me to complete the project.

I also would like to thank my former advisor, Dr. Brent L. Adams for his guidance on a large part of my experience as a graduate student in mechanical engineering. I am grateful for his inspiration on my research topic: the Hybrid Bishop-Hill model.

I am grateful for Dr. Christopher A. Mattson for his support and introducing me to the idea of design in engineering.

I also would like to thank other members of my Doctoral Committee, Dr. Larry L. Howell, Dr. Carl D. Sorensen, and Dr. Eric R. Homer for their support, advice, and willingness to serve on the committee.

This study was a portion of the project called, "Barriers to Reverse Engineering (BRE)." I would like to thank all of the project members for their support: Stephen Harston, Darren Knight, Nicole Anderson, and Dikshya Prasai.

The examples shown in chapter 3 of this dissertation was a collaborative work with Travis Ramption and Darrell Skousen.

I received great support from fellow students in the microstructure research group: Jay Basinger, Sadegh Ahmadi, Stuart Rogers, Ali Khosravani, Dikshya Prasai, Josh Kacher, Timothy Ruggles, Travis Rampton, Mark Esty, Dan Seegmiller, Samikshya Subedi, Jon Scott, Caroline Sorensen, Thomas Hardin, Scott Lemmon, Calvin (CJ) Gardner, Oliver Johnson, Suju Gurung. I cannot list all the names, but I am grateful for their friendship and examples of hard work.

This research was funded by the U.S. National Science Foundation, submitted by Dr. Brent L. Adams and Dr. Christopher A. Mattson, through a grant number CMMI-0800904.

I finally would like to thank my parents, my mother who passed away, my father, and my stepmother for their continuing encouragement and support in my schooling and my life. I am grateful for the Divine guidance and countless blessings throughout all aspects of this research and my life.

TABLE OF CONTENTS

LIST OF TABLES

LIST OF FIGURES

CHAPTER 1. INTRODUCTION

Microstructure Sensitive Design (MSD) is an innovative methodology for incorporating material microstructure information in design. This allows more accurate prediction of physical properties or functionality of products by incorporating the preferred crystal orientations relating to the microstructures, crystal phase, grain size, etc. The method uses a mathematical framework to systematically study potential material microstructures to meet the objectives of a specific design. Furthermore, the MSD method expands design space, and help designers to realize new possibilities in performance, which may have been missed by the standard design approach.

The work presented in this dissertation develops a new mathematical model of evaluating reliable estimates of plastic/elastic yield limit. Although this new method is derived from the theoretical stress corner defined by Bishop and Hill [1,2], the new approach called Hybrid-Bishop-Hill (HBH) model, focuses on stress states rather than strain states of FCC materials. This characteristic enables mechanical designers easier access to the evaluation of yield limit design because many of the mechanical design focuses on stress states on geometries in its design practice. The study applies the HBH model to various examples to demonstrate how mechanical design practice can be improved by the use of HBH model.

The study in this work uses single-phase polycrystalline oxygen free electronic (OFE) copper. Conventional thermo-mechanical treatment using rolling deformation has been applied to the samples to create various microstructures.

The dissertation comprises three sections. The first section focuses on development of the Hybrid-Bishop-Hill model. The section discusses how the idea for the need of stress-based yield model is developed and how it defines its elastic/plastic yield limit. A simple hole-in-plate problem with the use of HBH model demonstrates how anisotropic material properties open up a new design space.

The second section implements the HBH model to various geometrical structures through finite element analysis (FEA) to carry out the MSD. The HBH model is applied to different geometrical structures in this section. One of such geometry is the hole-in-plate problem; the study compares the result obtained from analytical HBH approach and FEA incorporated HBH model. The section also aims to demonstrate how HBH model can be adapted to mechanical design practice through the use of FEA.

The third section further develops the HBH model by incorporating fourth-parameter, geometrically necessary dislocation (GND) densities into its yield surface evaluation technique. The corner stress defined by Bishop-Hill model is carefully scaled by the GND densities to accurately demonstrate its influence on elastic/plastic yield limit. The section also searches the correlations between crystal orientation and GND densities. The study demonstrates how four-parameter approach works superior to standard-microstructure-based HBH model.

The computation and validation of the HBH model is carried out by MATLAB (2009a, 2009b, 2010a, The Mathworks) programing. The OFE copper samples used in this work are prepared by the use of available facilities at BYU, which includes rolling mill, tensile machine, wire EDM, conventional oven, polishing lab, machine shop, etc. The samples are primarily studied under the Phillips XL30 S-FEG scanning electron microscope (SEM). Microstructure data such as crystal orientations and high-resolution electron backscattered diffraction (EBSD) patterns are obtained and analyzed by the use of EDAX/TSL orientation imaging microscopy (OIM^{TM}) software (OIM 5.1, OIM 5.3, OIM analysis 5.0, and OIM analysis 6.0). The FEA-based approaches are studied with ANSYS (ANSYS®Academic Research, Release 13.0).

CHAPTER 2. HYBRID BISHOP-HILL MODEL FOR ELASTIC-YIELD LIMITED DESIGN

2.1 Chapter Overview

Three fundamental and interrelated design parameters affect yielding in materials; they are (1) part geometry, (2) material microstructure, and (3) boundary conditions. In typical design practice, these three types of design parameters lead to specific stress states, which are then compared to simplified yield criteria (e.g., von Mises and Tresca criteria) as a means to predict failure. Even simpler, in the most practiced sense, the largest stress component in a part is compared to a measured yield strength (typically recovered from the standard uniaxial tensile test). Clearly this simple yield-limited approach has been used in the past to create great parts and products [3, 4]. However, for any material that is not isotropic and homogenous, these methods rely upon an over simplification of the yield surface. Reliance upon this simplified approach in yield-limited design is partially due to ready-accessible tabulated yield strength data. But its use typically implies negligible variation of the yield strength with direction in the material. Extending these data sets to include yield anisotropy can be very challenging, and has only been attempted in the most highly constrained design problems. Ultimately, the readily available minimal yield data reduces the design engineer's opportunity to search for optimal material performance, which can only be done by including property anisotropy. This work presents a new, and accessible model for the anisotropic yield surface that can be used to consider first-order anisotropic yield characteristics in design.

The literature provides useful insight into the evaluation and representation of anisotropic yield surface models [5–7]. Through adaptations of the von Mises yield criteria, an empirical representation of the anisotropic yield surface can be developed. This representation however typically assumes material orthrombicity, and requires parameters that can only be found through implementation of a significant testing program. Several microstructure-based theories have been offered for the prediction of yielding in polycrystalline materials, such as the Taylor model [8], the

Bishop-Hill model, [1, 2] and various intermediate or hybrid models [9]. These classical models are focused upon integrating crystallographic texture (preferred distribution of lattice orientations) into yield predictions. Typically they require the input of a 'critical resolved shear stress', in order to properly scale the predictions to measured yield properties.

It is important to note that under the classical Taylor [8] and Bishop-Hill [1, 2] methodologies, plastic strain states must be specified to evaluate the yield stress. The difficulty is that, for design problems focused upon initial yielding, the elastic and plastic components of the total strain are comparable in magnitude and difficult to separate. Thus, the precise condition of plastic strain at initial yielding is not precisely specified. It follows that application of these classical microstructure-based theories of plasticity to initial yielding is a rather imperfect approximation at best.

The new models presented in this work, called the Hybrid Bishop-Hill (HBH) model [1], is closely related to the classical Bishop-Hill model [1,2] in predicting local stress states and mechanical yielding. The HBH model has the advantage, when used in the context of part design, of greatly expanding the design space, thus enabling the designer to reach into traditionally unexplored areas of performance. Because the computational burden associated with the full characterization of the 5-dimensional anisotropic yield surface is prohibitive, we develop a reduced representation of the yield surface that is much more accessible. Typically only a small portion of the complete yield surface is required for part design and the HBH model facilitates rapid access to the pertinent domain of the yield surface.

This chapter (1) describes a stress-focused anisotropic yield limited design approach, incorporating the new HBH model, which (2) does not require an evaluation of plastic strain (or strain rate) at yielding, (3) preserves the characteristic of local grain-scale heterogeneity present in the Taylor and Bishop-Hill models, and (4) efficiently accesses a realistic portion of the anisotropic yield surface pertinent to the mechanical design.

The new methodology is applied to an extensive database of rolled and annealed FCC Cu materials (Oxygen Free Electronic purity grade). Although these materials exhibit the typical orthorhombic symmetry in their crystallographic textures, consideration is also given to rigid body rotations of the principal axes of orthorhombicity, about the rolling plane normal direction. Prop-

[1] This chapter has been published [10].

erty closures, of the type developed by microstructure-sensitive design methodology [11, 12], are utilized to describe the breadth of elastic/yielding performance available within the complete material database. Demonstration of the new methodology is focused upon the common problem of stress concentration about a circular hole in a plate, loaded under uniaxial tension in arbitrary directions with respect to the principal material axes. Analytical solutions to the elastic equilibrium equations, provided by Lekhnitskii, [13] are used in the mechanical analysis.

The remainder of this chapter is presented as follows. In section 2.2, we present the technical preliminaries required to introduce the new methodology. In section 2.3, we present the new approach for the mechanical yield limit design. Section 2.4 presents the application of the approach to the hole-in-plate design problem.

2.2 Background

2.2.1 Property Closure

The simplest form of homogenization relations, associating the distribution of local states of microstructure to estimates of the macroscopic (effective) elasticity, require only volume fraction information on the distribution. Hill-Paul upper- and lower-bounds [12] on the stored elastic strain energy density can be expressed in the following ways.

$$\begin{aligned} \overline{\varepsilon}_{ij}(\overline{S})^{-1}_{ijkl}\overline{\varepsilon}_{kl} \leq \overline{\varepsilon}_{ij}C^{eff}_{ijkl}\overline{\varepsilon}_{kl} \leq \overline{\varepsilon}_{ij}\overline{C}_{ijkl}\overline{\varepsilon}_{kl} \\ \overline{\sigma}_{ij}(\overline{C})^{-1}_{ijkl}\overline{\sigma}_{kl} \leq \overline{\sigma}_{ij}S^{eff}_{ijkl}\overline{\sigma}_{kl} \leq \overline{\sigma}_{ij}\overline{S}_{ijkl}\overline{\sigma}_{kl} \end{aligned} \tag{2.1}$$

Here C^{eff} and S^{eff} are the fourth-order effective elastic stiffness and compliance tensors, S and C are the local ones, ε is the local (second-order) infinitesimal strain tensor, σ is the Cauchy stress tensor, and the bar over the top of any of these tensors indicates the volume average of the same. (Note that the Einstein summation convention has been used in Eq. 2.1, in that repeated indices occurring on the same side of the equation signify summation from 1 to 3 over that index. Thus, each term in Eq. 2.1 contains 81 terms. This same convention is applied throughout the chapter.)

Although Eq. 2.1 rigorously bound the elastic energy density, bounding of the effective stiffness tensor itself is only convenient when the indices k, l are set equal to i, j. In this situation

the following bounds must be satisfied:

$$\begin{aligned} \overline{S}^{-1}_{ijij} \leq C^{eff}_{ijij} \leq \overline{C}_{ijij} \\ \overline{C}^{-1}_{ijij} \leq S^{eff}_{ijij} \leq \overline{S}_{ijij}. \end{aligned} \tag{2.2}$$

Thus, bounds on 9 of the 21 independent effective elastic constants are readily available from simple volume averages over the corresponding local elastic constants, but more complex relations are required to bound the remaining terms [11, 12]. For our purposes in this study, we will focus upon the 'Hill average elastic constants', $C^{eff(Hill)}$ and $S^{eff(Hill)}$, which are defined by the following expressions.

$$\begin{aligned} C^{eff(Hill)}_{ijkl} \approx \frac{\overline{S}^{-1}_{ijkl} + \overline{C}_{ijkl}}{2} \\ S^{eff(Hill)}_{ijkl} \approx \frac{\overline{C}^{-1}_{ijkl} + \overline{S}_{ijkl}}{2} \end{aligned} \tag{2.3}$$

The Hill average constants are an average of the upper- and lower-bounds on the effective elastic constants; and the expressions apply to all 21 independent components.

Refinements in the prediction of elastic constants are available [11, 12], but such require additional information on the spatial placement of local state, in addition to the distribution by volume fraction. For our purposes the Hill average estimates will be sufficient.

2.2.2 Distribution of Local States

The term 'local state' refers here to any local characteristic of the material that affects the property of interest. The 'local state distribution' refers to how the components of microstructure are distributed upon the set of possible local states. A common example of a local state distribution function is the familiar orientation distribution function, used in describing the crystallographic texture of polycrystals [14]. For the materials of interest in this chapter, two types of local state will be important, but only one will be considered to vary. Only one material phase is present in oxygen free electronic (OFE) Cu polycrystals - the FCC Cu phase. Impurity levels in this material are small; and these impurities are typically dispersed in interstitial form within the dominant phase. It is assumed that the local elastic state of the material is determined only by the orientation of the crystal lattice, and by the basic elastic properties of the Cu phase, C^{Cu}. If the direction

cosines, $g(x)$, are known at any local position x, then the local elastic properties are given by the expression.

$$C_{ijkl}(x) = g_{im}(x)g_{jn}(x)g_{ko}(x)g_{lp}(x)C^{Cu}_{mnop} \tag{2.4}$$

The sense of the direction cosines in this expression is a coordinate transformation from the $\langle 100 \rangle$ crystal axes of the FCC unit cell, to the selected orthonormal coordinate system in the macroscopic or specimen frame. Clearly $g(x)$ varies little when x varies within an individual grain, but it jumps as x traverses a grain boundary.

$g(x)$ is the local state variable of principal interest in this chapter. With respect to the Hill average estimates of effective elastic properties, given by Eq. 2.3, Eq. 2.4 can be used as input into volume averaging, if $g(x)$ is known for a sufficient sampling of material points x. Current experimental electron backscatter diffraction (EBSD) techniques [12, 15] are very efficient at measuring $g(x)$ for large numbers of material points.

The second local state variable of interest to the present work is the critical resolved shear stress, τ_{crss}. This reflects the level of shear stress that must be present upon any of the $\{111\}\langle 110 \rangle$ slip systems to cause dislocation slip to occur. It is known that τ_{crss} is proportional to the square root of the local total dislocation density, which typically varies with position x. However, in the present work τ_{crss} will be held constant for any specified material condition within the database. Determination of τ_{crss} will be discussed later.

Various parameterizations of $g(x)$ are available. Of course the full 3×3 matrix of coefficients of the direction cosines, utilized in Eq. 2.4, is an important parameterization; however only 3 of the 9 direction cosines are independent [12, 14]. And for the purposes of defining the range of all possible lattice orientations, it is convenient to reduce $g(x)$ to 3 independent variables. Many choices are possible, but the Bunge Euler angles, ϕ_1, Φ, ϕ_2, are the most common [14]. These define a sequence of three primitive rotations that are required to bring a sample-fixed coordinate frame into coincidence with the lattice fixed frame on $\langle 100 \rangle$. Output of the Bunge Euler angles is common, using established image processing applied to EBSD patterns [15]. When symmetry of the FCC crystal lattice is fully considered, it is convenient to express a 3-fold redundant space of

possibilities for ϕ_1, Φ, ϕ_2 [12]:

$$FZ_{3c} = \left\{ g \equiv (\phi_1, \Phi, \phi_2) \left\| \begin{array}{l} 0 \leq \phi_1 < 2\pi \\ 0 \leq \Phi < \dfrac{\pi}{2} \\ 0 \leq \phi_2 < \dfrac{\pi}{2} \end{array} \right. \right\}. \tag{2.5}$$

The 3-fold redundancy refers to the fact that each physically distinctive lattice orientation appears 3 times in FZ_{3C}. Further reduction to the point that each distinctive orientation appears only one time is possible, but the inconvenience is that the fundamental zone contains a complex surface, which renders partitioning difficult. Experience dictates that it is easier to work with the rectangular 3-fold redundant fundamental zone described by Eq. 2.5. From the experimental point of view, each EBSD-based measurement of lattice orientation will occur 3 times in FZ_{3C}.

The rectangular shape of FZ_{3C} can be split into smaller bins of rectangular shape. All computations of the type required in Eq. 2.3 will be handled discretely, using binned datasets. Suppose that N such bins have been defined, and designated by ω_n, where

$$\omega_n \subset FZ_{3c}, \quad \bigcup_{n=1}^{N} \omega_n = FZ_{3c}, \quad \omega_n \cap \omega_m = \oslash \ (m \neq n). \tag{2.6}$$

Associated with each bin ω_n is an indicator function $\chi_n(g)$, defined by the expression.

$$\chi_n(g) \equiv \chi_n(\phi_1, \Phi, \phi_2) \begin{cases} 1, & if \ g \in \omega_n \\ 0, & \text{otherwise} \end{cases} \tag{2.7}$$

The size of the bins will have an effect upon the errors in forming the averages required by the Hill estimates of effective elastic stiffness.

The pertinent local state distribution is the distribution of lattice orientation among the sampled material points. Imagine that a total of S local orientations have been measured by EBSD-based methods. A condition of statistical sufficiency is assumed for this set of measurements. Roughly, this means that the measurements are taken in a sufficiently large number of components of microstructure (grains) to ensure that the experimental sampling is characteristic of the overall

microstructure. After converting each of the S measurements of orientation into it's 3 equivalent orientations within FZ_{3C}, the $3S$ determined orientations will be distributed among the N defined bins. Let f^n denote the fraction of $3S$ orientations that fall within ω_n.

$$f^n = \frac{1}{3S}\sum_{s=1}^{3S} \chi_n\{g_s\} \tag{2.8}$$

The local state distribution function, in this case closely related to the orientation distribution function, will consist in the set of real number fractions f^n, $F = \{f^1, f^2, \cdots, f^N\}$. From Eq. 2.8 conservation of volume requires that

$$\sum_{n=1}^{N} f^n = 1. \tag{2.9}$$

Approximations to the average elastic tensors required in Eq. 2.3 are readily formed from the local state distribution function via expressions of the form

$$\overline{C}_{ijkl} \approx \sum_{n=1}^{N} f^n C^n_{ijkl} \tag{2.10}$$

where C^n denotes the value of the elastic stiffness calculated by Eq. 2.4 with ϕ_1, Φ, ϕ_2 taken to be a characteristic lattice orientation lying within the associated bin ω_n. Numerical examination of the bin-size dependency of calculations like Eq. 2.10 have determined that numerical errors are $\sim 1\%$ when a bin size of $5^\circ \times 5^\circ \times 5^\circ$ in the three Euler angles is selected within FZ_{3C}; consequently, this bin size was utilized throughout the present work.

2.2.3 Taylor-Bishop-Hill Model

Since its introduction in 1938, the Taylor [8] first-order upper bound on the yield strength of rigid elastic (elastic strains are ignored), perfectly-plastic (strain hardening is not considered) polycrystals [16] has been widely applied to the problem of yielding. Of course these simplified conditions do not accurately reflect the heterogeneous nature of elastic/plastic behavior in polycrystals at the yield point. Essential to the Taylor model is the approximation that all crystallites or grains are subject to the same plastic strain. In the original theory, plastic deformation is constrained to occur by shear on specified slip systems, and the required plastic shear strains on these

slip systems are discovered. In FCC materials like Cu, which has 12 $\{111\}\langle 110\rangle$ slip systems, a large number of choices of 5 slip systems (required to accommodate an arbitrary incompressible plastic deformation) can be discovered from among the 12 available slip systems. At this point Taylor postulates that the correct combination will be the set that accomplishes the required deformation with the least amount of total shear: the so-called minimum work criterion. (Those practiced in the Taylor model will recall that it is often the case that there remains a redundancy in the available sets of slip accommodation. Several choices remain with the same minimum work condition. However, for consideration of yield strength alone, this redundancy is of no further interest.)

The question naturally arose after the emergence of the Taylor model, as to whether or not actual homogeneous stress conditions could be discovered that would activate any particular required set of slip systems for yielding. Thus came the Bishop-Hill model in 1951 [1, 2]. It was discovered that for FCC materials a set of 56 stress states are capable of activating the required combinations of slip for an arbitrary plastic deformation. These 56 stress states are also known as 'stress corners', because they form the vertices of a convex polytope, which is the yield surface in 5-D deviatoric stress space. A maximum work criterion was presented for correctly identifying the pertinent stress corner associated with any particular impressed plastic strain. Later Chin and Mammel showed that the Taylor and Bishop-Hill models are dual solutions to the same linear problem [17]. For this reason some authors refer to these two complimentary models as the Taylor-Bishop-Hill (TBH) model.

These 56 vertices or corners of the yield surface for FCC crystals can be grouped into 5 different types: the first three groups activate 8 slip systems simultaneously; and the fourth and fifth groups activate 6 [1, 18]. According to the TBH model, a slip system is only activated when the resolved shear stress meets or exceeds τ_{crss}. It is also found that the resolved shear stress upon the non-active slip systems is zero [18]. Appendix B lists 28 of the 56 TBH corner stress states; the remaining 28 are simply related to the first 28 by a minus sign.

According to the TBH model, each grain experiences the uniform (macroscopic) imposed strain. TBH theory hypothesizes that the active corner stress state is the one that maximizes the work done. If the local corner stress is σ^C, and the imposed strain increment is $\delta\varepsilon$, then the

increment of plastic work, δW^p for any particular choice of stress corner will be

$$\delta W^p = \sigma_{ij}^C(x)\delta\varepsilon_{ij}(x). \tag{2.11}$$

The correct choice for the active stress corner, within the TBH model, is the one that maximizes δW^p.

First-order estimates of the TBH upper-bound on the yield strength in polycrystals can be computed from the S measurements of lattice orientation, $g(x)$, according to the following expression:

$$\overline{\sigma}_{ij}^Y \approx \sum_{n=1}^{N} f^n \sigma_{ij}^{Cn}(\delta\varepsilon). \tag{2.12}$$

Here $\delta\varepsilon$ is the imposed plastic strain increment, $\overline{\sigma}^Y(\delta\varepsilon)$ is the predicted macroscopic yield stress associated with the selected plastic strain increment, and $\sigma^{Cn}(\delta\varepsilon)$ is the correct TBH stress corner associated with bin n and the imposed plastic strain increment, according to Eq. 2.11. (Note that it is essential that all terms in Eq. 2.12 be expressed in the macroscopic or specimen coordinate frame.)

2.2.4 Estimation of τ_{crss} from the TBH Model

The corner stress states required to implement the yield stress estimation expressed in Eq. 2.12 require knowledge of τ_{crss}. A particular way of estimating the τ_{crss} has been used, and will be briefly described here. It is assumed that experimental uniaxial tensile testing has been conducted on each material of interest.

Tensile samples are cut to a geometry, and loaded in such a way that to a first approximation only a single tensile component of the stress can be present in the gage section of the sample. We designate this tensile axis as the $\hat{e}_1$ direction, with the two transverse directions being $\hat{e}_2$, $\hat{e}_3$. If the tensile testing is conducted with $\hat{e}_1$ aligned with any one of the principal axes of material microstructure, then it is reasonable to expect that the plastic strain increment in the gage section

to have a diagonal form that can be expressed as

$$\delta\varepsilon \equiv \delta\varepsilon_{11}\begin{bmatrix} 1 & 0 & 0 \\ 0 & -\eta & 0 \\ 0 & 0 & -(1-\eta) \end{bmatrix} \tag{2.13}$$

where η is the contractile (plastic) strain ratio, $\eta = \dfrac{\varepsilon_{22}}{\varepsilon_{11}}$. In principle this contractile strain ratio can be measured in the tensile sample after yielding has occurred, when the load has been removed from the sample. Once the relevant contractile strain ratio is known, the appropriate strain increment is known, and Eq. 2.12 can be used to estimate the uniaxial yield strength, $\overline{\sigma}^{Y}_{11}$. This estimate scales linearly with τ_{crss}, and adjustments in τ_{crss} can be pursued until $\overline{\sigma}^{Y}_{11}$ matches with the experimentally measured yield stress. This is the basic approach.

In practice it is difficult to measure the plastic contractile strain ratio at initial yielding, because the plastic strains involved are small, $\sim 10^{-3}$. One approach to overcome this is to deform the sample to larger deformations, and then to assume that the contractile strain ratio observed at these larger strains will be representative of the one at smaller strains. The limitations of this approach are obvious. Another approach, which is numerical, is to take the contractile ratio to be a variable, and then to calculate the estimate of the yield stress tensor for each selected choice of the ratio. When the predicted stress state is as close as possible to the uniaxial condition, it can be assumed that the correct contractile ratio has been discovered. This approach is equivalent to minimizing the average overall plastic work increment, δW^{p}. In the present work, this latter approach has been taken.

2.2.5 Determination of Elastic-Yield Property Closures

Interest in the complete range of elastic/yield property combinations that could occur within all conceivable polycrystalline microstructures of fixed material phase typically occurs during preliminary design. Theoretical methods for constructing estimates of properties closures have been presented in the literature [12, 19–21]. The approach taken is to make use of available microstructure-sensitive homogenization relations for the properties of interest, and then to consider all possible microstructures, beginning with single crystals of an arbitrary lattice orientation.

Details of this approach are not given here; but the interested reader will find the methods detailed in the referenced literature [12, 19–21]. Of interest in this work is a limited, or 'accessible properties closure', comprising the portion of the full elastic/yield closure that is readily accessible with ordinary materials processing.

2.2.6 Anisotropic Properties of Orthotropic Plates Containing Circular Holes

As an example of a simple anisotropic design problem, where microstructure considerations are of paramount importance, the classical problem of 'hole-in-anisotropic-plate' will be revisited. The detailed mechanics of plates containing a circular hole, and with microstructures exhibiting orthorhombic symmetry, was presented by Lekhnitskii [13]. Considering an infinite plate, loaded under uniaxial in-plane tension in an arbitrary direction with respect to a selected principal axis of material orthorhombicity, the tensile stress tangential to the inner surface of the hole is given by the expression:

$$\begin{aligned}\sigma_\theta = p\frac{E_\theta}{E_1}\{&[-\cos^2\phi + (k+n)\sin^2\phi]k\cos^2\theta \\ &+ [(1+n)\cos^2\phi - k\sin^2\phi]\sin^2\theta \\ &- n(1+k+n)\sin\phi\cos\phi\sin\theta\cos\theta\}.\end{aligned} \tag{2.14}$$

In this expression p is the applied stress, exerted a large distance away from the circular hole. θ defines an angle relative to the selected principal material axis (taken to be the rolling direction in this work) that identifies the location of a point on the circumference of the circular hole. This is defined to be the tensile stress tangential to the point of circumference identified by θ. Finally, ϕ denotes the direction of the applied stress with respect to the principal material axis. Other components in Eq. 2.14 are defined by the expressions.

$$\begin{aligned}\frac{1}{E_\theta} &= \frac{\sin^4\theta}{E_1} + (\frac{1}{G} - \frac{2\nu_1}{E_1})\sin^2\theta\cos^2\theta + \frac{\cos^4\theta}{E_2} \\ k &= \sqrt{\frac{E_1}{E_2}} \\ n &= \sqrt{2\frac{E_1}{E_2} - \nu_1 + \frac{E_1}{G}}\end{aligned} \tag{2.15}$$

The symbol ν_1 represents Poisson's ratio perpendicular to the principal material axis, E_1 and E_2 represent Young's modulus in the rolling and transverse directions of the sheet, respectively, and G is the in-plane shear modulus. Given the traction-free condition at the circumference of the hole, and the other geometrical and boundary conditions, σ_θ is the only non-zero component of stress that can occur adjacent to the circular hole. Estimates for each of these effective elastic properties are accessible by calculations of the Hill average properties, using Eq. 2.3 and Eq. 2.10.

Predictions of σ_θ, taken from Eq. 2.14, will be compared to estimates of the yield strength, which also varies with θ, in order to establish the maximum value of the tensile load p that can applied to the plate without causing yielding. The design problem reduces to the matter of determining, for any particular material, the peak load that can be applied and the direction ϕ in which it must be applied. Figure 2.1 depicts the essential geometrical definitions for the anisotropic hole-in-plate problem.

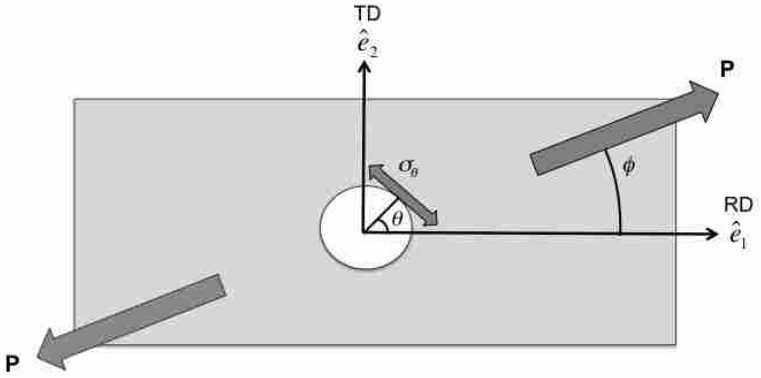

Figure 2.1: A geometry of anisotropic hole-in-plate problem

2.3 Proposed Hybrid Bishop-Hill Model

In most yield limited design problems the interest is in the near-vicinity of the yield surface, where the plastic strain is not dominant compared to the elastic strain. If the spatial character of the strain state is considered, it is not constant, but varies with position in complex ways. These conditions call to question the application of the TBH model for the problem of initial yielding.

For plastic problems where the total strain is dominated by the plastic component, this is not an issue.

Our present purpose is to propose a modified version of the TBH model, which will be named the 'Hybrid Bishop-Hill Model' (HBH model). Importantly, the focus of the HBH model is on the applied stress, rather than on the plastic strain; this makes the model much more accessible to design engineers who focus more upon stress states, rather than strain states. The algorithm for predicting the yield strength of the polycrystalline material via the HBH model uses the same stress corners that were defined for the TBH model. Retaining this characteristic means that there will be a natural heterogeneity of local stress among the constituents of the polycrystal.

A simple assumption is taken that the local yielding at any position in the material occurs at the corner stress state, $\hat{\sigma}_{ij}^{C}$, that lies "closest" to the macroscopic stress, $\hat{\sigma}_{ij}$. The "hat" over the stress symbols signifies the deviatoric stress. Distance between these two stress states is defined by d_{ij}, where

$$d_{ij} = \hat{\sigma}_{ij}^{c} - \hat{\sigma}_{ij}. \tag{2.16}$$

The magnitude of distance between stress states, d, is defined by the Euclidean norm:

$$||d^2|| = d_{ij}d_{ij}. \tag{2.17}$$

Importantly, the distance defined according to Eq. 2.16 and Eq. 2.17 is invariant with respect to coordinate transformation. The selection of stress corner for any particular component (grain) within the polycrystal is taken to be the Bishop-Hill corner stress that minimizes the distance d between the applied stress and the corner stress state.

The estimated (deviatoric) yield strength of the material is obtained from the expression

$$\hat{\sigma}_{ij}^{Y} \approx \sum_{n=1}^{N} f^{n} \hat{\sigma}_{ij}^{Cn} \tag{2.18}$$

$\hat{\sigma}^{Cn}$ denotes the pertinent stress corner associated with bin n in FZ_{3c}. Note that all corner stress states exercised in Eq. 2.18 must be expressed in the macroscopic (sample) frame in order to interpret $\hat{\sigma}_{ij}^{Y}$ as the yield strength. Whereas yield strength is customarily described as the full

Cauchy stress, the deviatoric yield stress must be converted, using the customary definition:

$$\sigma_{ij}^{Y} = \hat{\sigma}_{ij}^{Y} + \frac{1}{3}\delta_{ij}\sigma_{kk}^{Y} \quad \text{(summation over k implied).} \tag{2.19}$$

Exercising Eq. 2.19 to obtain σ_{ij}^{Y} requires additional physical information about the applicable pressure $\frac{1}{3}\delta_{ij}\sigma_{kk}^{Y}$ or some other characteristic of the normal components of σ_{ij}^{Y}. If, for example, the calculations involve estimates of a uniaxial tensile test, then only one component of σ_{ij}^{Y} is expected to be non-zero; and in this case a pressure term $\frac{1}{3}\delta_{ij}\sigma_{kk}^{Y}$ can be applied that renders σ_{ij}^{Y} as close as possible to a uniaxial stress condition. This is the approach taken in the present work.

Recall that the corner stress states of the TBH model are states that are capable of supporting general local states of plastic strain. Consistent with the classical Taylor model, the TBH model defines stresses that are capable of causing an arbitrary plastic strain state, by $\{111\}\langle 110\rangle$ dislocation slip. The TBH model does not satisfy the stress equilibrium condition, although when the macroscopic plastic strain is imposed upon each individual grain within the material, strain compatibility is fulfilled in a trivial sense. The new HBH model fulfills neither stress equilibrium, nor strain compatibility at a local level. However, having utilized the TBH stress corners in the model to estimate local stress conditions, it can be anticipated that complex plastic strain conditions, as required by the equilibrium and compatibility requirements under elastic/plastic loading, could more readily be satisfied by the stress corners. To some extent the HBH model could be compared to the relaxed-constraints model(s) that preserve some features of Taylor-like models, but do not strictly enforce either strain compatibility or stress equilibrium [22].

The basic relations pertaining to the HBH model (Eq. 2.16 through Eq.2.18) can be applied to arbitrarily complex loading states.

2.4 Results and Discussions

2.4.1 Database of OFE Copper Materials

It will be obvious to those familiar with materials processing, that the range of microstructures that are readily accessible to the designer comprise a range of properties that is much smaller than the set considered by the theoretical properties closure, briefly described in section 2.2.5. A

limited, accessible closure for elastic/yield properties has been considered for OFE Cu. Three common processing routes have been considered: rolling deformation, thermal annealing, and rigid body rotation of the material about the normal direction to the rolling plane. Rolled OFE Cu plate (in the as-received 'half-hard' condition), and 6 derivative materials produced there-from by secondary processing steps, and one addition material (very strongly 'cube textured', provided by Oak Ridge National Laboratory), were considered in the database. Table 2.1 Describes the processing conditions for each of these samples.

Table 2.1: Sample description

Sample Description	*Heat Treatment Temperature* (C°)	*Heat Treatment Time* (*Hour*)
As received	N/A	N/A
As received and annealed	191	1
98% cold worked	22	N/A
98% cold worked and recrystallized	225	0.5
58% cold worked	N/A	N/A
58% cold worked and annealed	160	1
58% cold worked and recrystallized	225	1.5
Cube texture	N/A	N/A

Theoretically, each of these 8 materials within the 'accessible' database, were then allowed to rotate around their plane normal, in order to compute the 'accessible properties closure'. The local state distribution can easily be recomputed for an arbitrary rotation angle, and then Eq. 2.10 and Eq. 2.12 can be re-exercised to recover the changed estimates for elastic and yielding properties. Rotations of the sample relative to the loading gives rise to orbits in the properties closure. Further details of this approach are provided in the 2008 paper of Adams et al. [19]. The complete and accessible closure for σ_{θ}^{Y} (in-plane uniaxial yield strength in direction $\hat{\theta}$) versus E_{θ} (Young's modulus associated with the same in-plane direction) is shown in Figure 2.2. The reader should note that E_1 in Eq. 2.14 and Eq. 2.15 is related to this notation by $E_1 = E_0 = E_{\theta=0}$ and $E_2 = E_{\pi/2} = E_{\theta=\pi/2}$.

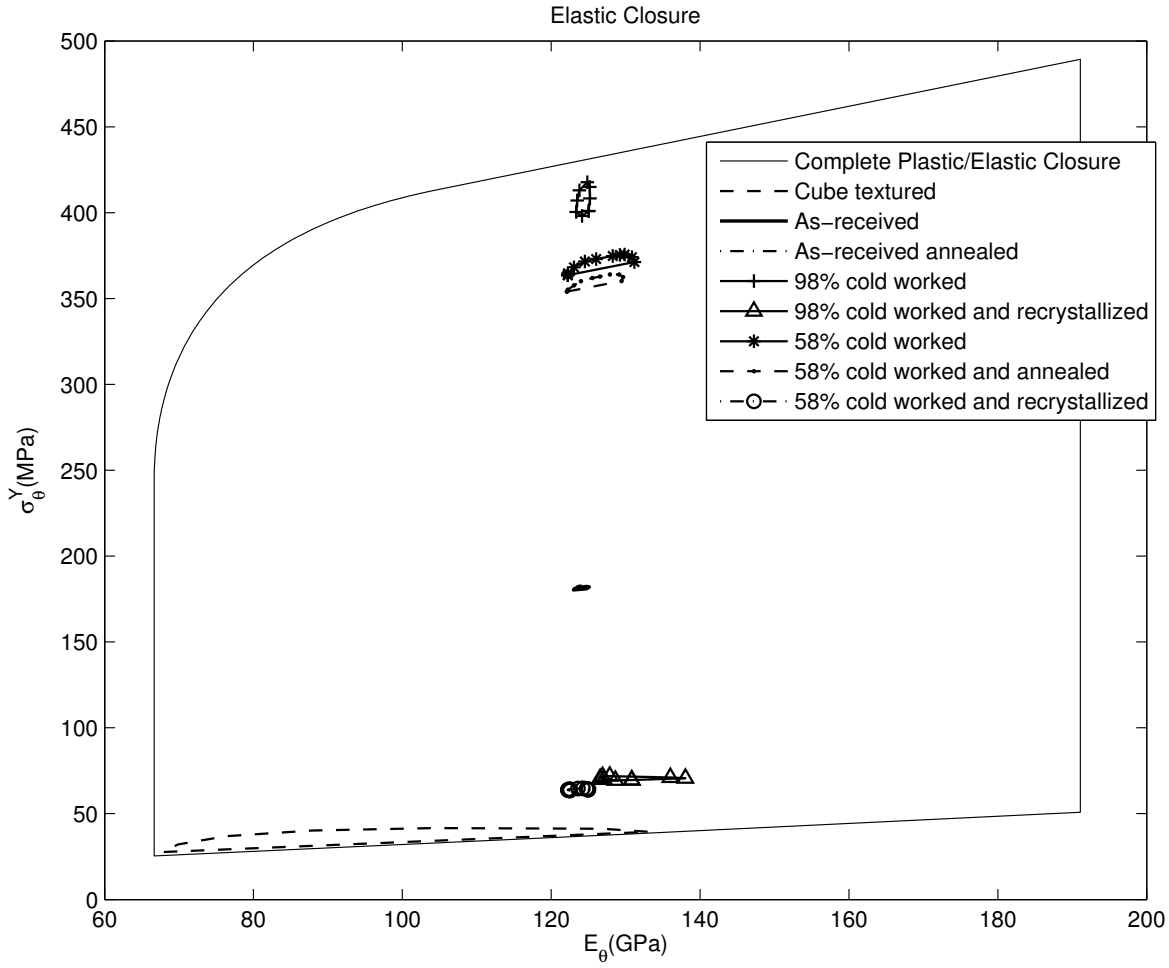

Figure 2.2: Property closure

2.4.2 Comparison of HBH and TBH Models

An accessible comparison is here detailed for the predictions of yield strength for the 8 OFE Cu materials included in the database of this study. The comparison is between predictions based upon the classical TBH and the new HBH models.

Appendix A contains the $\{111\}$ and $\{200\}$ crystallographic pole figures for each material of the database. These were obtained from EBSD data sets comprising a minimum of 2,500 grains for each sample (excluding the 'cube texture' material, which has a large grain size). The peak value for the texture of these materials was measured to be in excess of 37 'times-random', for the cube texture sample, for the $\{100\}\langle 001\rangle$ component. Most of the other materials exhibited the

classical rolling texture, [23] with peak times-random values ranging from 1.6 in the as-received material, upwards to 5.5 in the 98% cold worked sample. It is evident that upon annealing the 98% cold rolled material, a $\{100\}\langle 001\rangle$ cube component develops with an intensity of ~ 3.7 times random.

Standard tensile testing was conducted for the purpose of recovering the yield strength in the rolling direction, RD, in each sample. (The yield strengths reported are the typically average values from 3 tensile tests.) Using the numerical approach described in Sec. 2.2.4, the contractile strain ratio η was varied in connection with Eq. 2.11 and Eq. 2.12 until the macroscopic increment of plastic work, $\delta\overline{W}^p$, estimated from the TBH model, was minimized. Using this estimate for the strain increment, τ_{crss} was estimated from the Taylor factor and the experimental yield strength. The results of this comparison are shown in Table 2.2. It is evident that in most instances the new HBH model more accurately predicts the yield strength in comparison with the TBH model.

Table 2.2: Comparison of experimentally obtained tensile yield strength vs. the numerically obtained yield strength

Samples	*Contractile Strain Ratio* η	*Experimental Tensile Yield Strength (MPa)*	*The TBH Yield Strength (MPa)*	*The Hybrid Yield Strength (MPa)*
As received	0.51	185.40	201.74	181.07
As received and annealed	0.49	185.67	204.05	182.10
98% cold worked	0.43	423.48	436.15	400.95
98% cold worked and recrystallized	0.52	71.93	77.83	69.67
58% cold worked	0.36	377.10	401.11	363.53
58% cold worked and annealed	0.39	363.93	391.08	354.06
58% cold worked recrystallized	0.54	65.43	72.14	63.97
Cube texture	0.39	33.76	50.56	27.65

2.4.3 HBH-Based Design for the Anisotropic Hole-In-Plate Problem

First, consider the plate without a hole. Variation of the uniaxial yield strength, σ_ϕ^Y , with direction of the applied load, ϕ, is shown in Figure 2.3 for each of the 8 materials within the database. The variation of yield strength (σ_ϕ^Y, with respect to ϕ) is as small as $\sim 1\%$ in the as-received and as-received annealed materials, to $\sim 33\%$ in the strongly cube-textured material. In

terms of absolute strength, it is not unexpected that the lowest values of strength are found in the most heavily annealed materials, and the highest values are seen in the most heavily cold-worked material. The range of strength is from $\sim 30 - 425$ MPa.

Next, consider plates containing a circular hole, loaded under uniaxial tension. The simple stress states around the circumference of the hole, are purely uniaxial; and they act in a tangential direction relative to the circumference of the hole. This is expressed by Eq. 2.14, and Eq. 2.15. This stress state can be compared with the theoretical yield stress in the same direction, as determined using the HBH model. Note that σ_θ depends linearly upon the magnitude of the stress p applied in direction ϕ; and the magnitude of σ_θ depends on both variables, ϕ and θ. In this chapter, we are interested in two stress states, σ_ϕ and σ_θ. σ_ϕ denotes a uniaxial stress aligned with the direction defined by ϕ; and with respect to the hole-in-plate problem, $\sigma_\phi = p$. σ_θ, however, in the context of the hole-in-plate problem, is the tangential stress acting at the point identified by θ on the circumference of the circular hole, as shown in Figure 2.1, as evidenced by Eq. 2.14 and Eq. 2.15, $\sigma_\theta = \sigma_\theta(p, \phi)$. The distinction between σ_ϕ and σ_θ is that the former is parallel to the direction defined by ϕ, and the latter is perpendicular to the direction specified by θ. When the superscript Y is used, as with σ_ϕ^Y or σ_θ^Y, what is meant is the uniaxial yield strength of the material for the particular the stress state.

Figure 2.4 compares the θ - dependent yield strength, σ_θ^Y, with the calculated stress state around the circumference of the circular hole for the cube texture OFE Cu plate for constant values of ϕ and σ_ϕ. For this example ϕ was chosen to be 45° (i.e., 45° from RD), and the magnitude of the applied stress, p, was taken at a level that just causes these two curves to touch one another at $\theta = 105°$ and 285°, at a stress level of $\sigma_\theta^Y = 36$ MPa. For stress levels that exceed this it is predicted that plastic yield will occur, first at these two circumferential angles, and then later at other locations associated with minima in the yield stress curve. Note that changes in the angle ϕ of application of the applied stress p will change the form of σ_θ. Peak performance in design with plates containing circular holes will consist in identifying the direction ϕ at which the largest p can be applied without causing plastic yielding at any position θ about the hole.

This same analysis can be performed for all of the plate types found in the database. Let p_ϕ^Y denote the applied stress in direction ϕ where yielding begins. This behavior is shown in Figure 2.5.

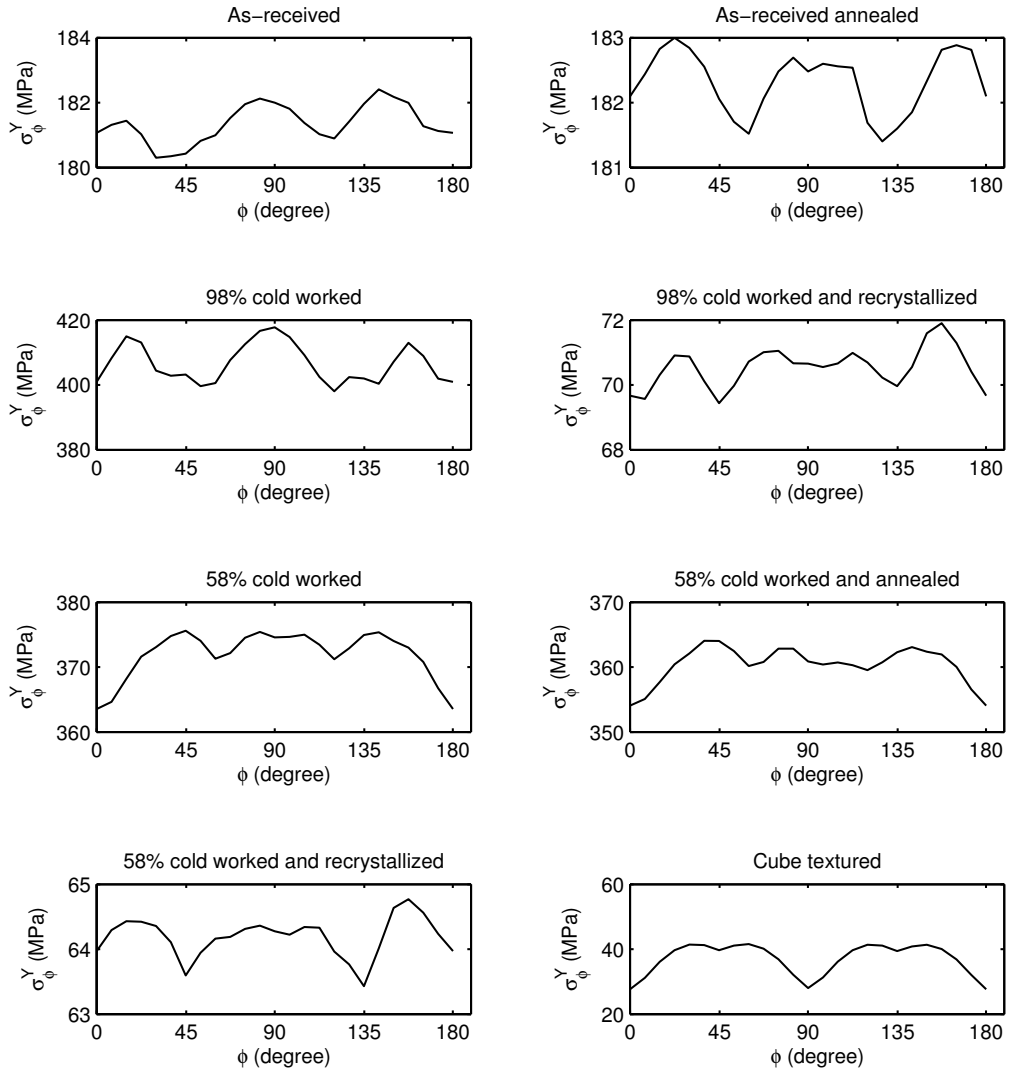

Figure 2.3: A variation in yield strength with respect to the applied tensile load direction in anisotropic plates

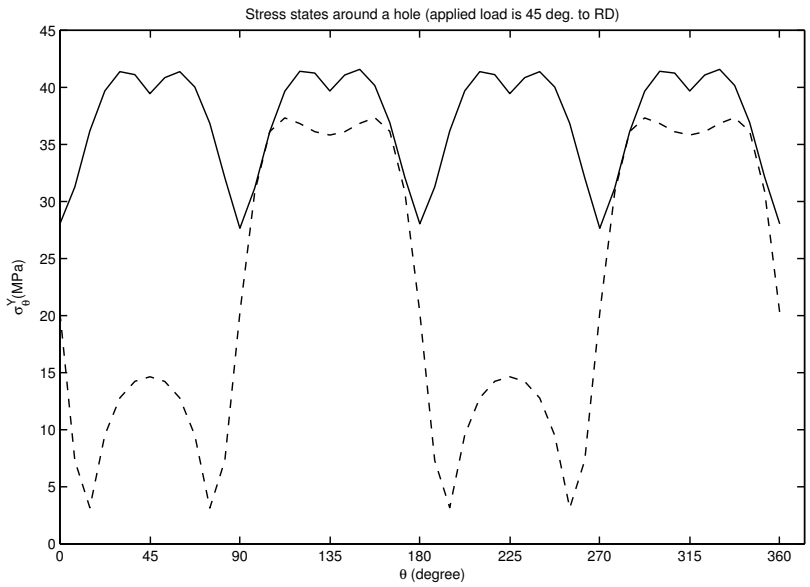

Figure 2.4: The stress states around a circular hole in cube texture plate (the dotted line) and the related yield stress of the material (solid line). When the stress states (σ_θ) touch the yield stress (σ_θ^Y), the material is considered to be yielded. The applied stress is at $\phi = 45^\circ$ to the sample rolling direction.

The best and worst performances can be obtained from Figure 2.5 for the various materials. This minimum performance is interesting from the point of view that an uninformed designer could inadvertently load a plate with circular hole in the direction where minimum strength would be realized. Another way to look at the maximum and minimum performance is in terms of the associated stress concentration factors. An anisotropic stress concentration factor, K_t can be defined as the following:

$$K_t = \frac{\max\ \sigma_\theta}{p_\phi^Y} \tag{2.20}$$

where max σ_θ signifies the peak value of σ_θ that occurs around the circumference of the hole at the applied load at which yielding occurs, p_ϕ^Y. For isotropic materials K_t becomes 3, but for anisotropic materials it can be larger or smaller than 3. A complete listing of the predicted maximum and minimum performance levels, their associated yield strengths p_ϕ^Y, and the angles of load application, and their related stress concentration factors, is presented in Table 2.3.

As-received OFE copper plate and its derivatives gives K_t close to 3; however, the highly cube textured sample gives K_t less than 2.5. The range of predicted maximum and minimum

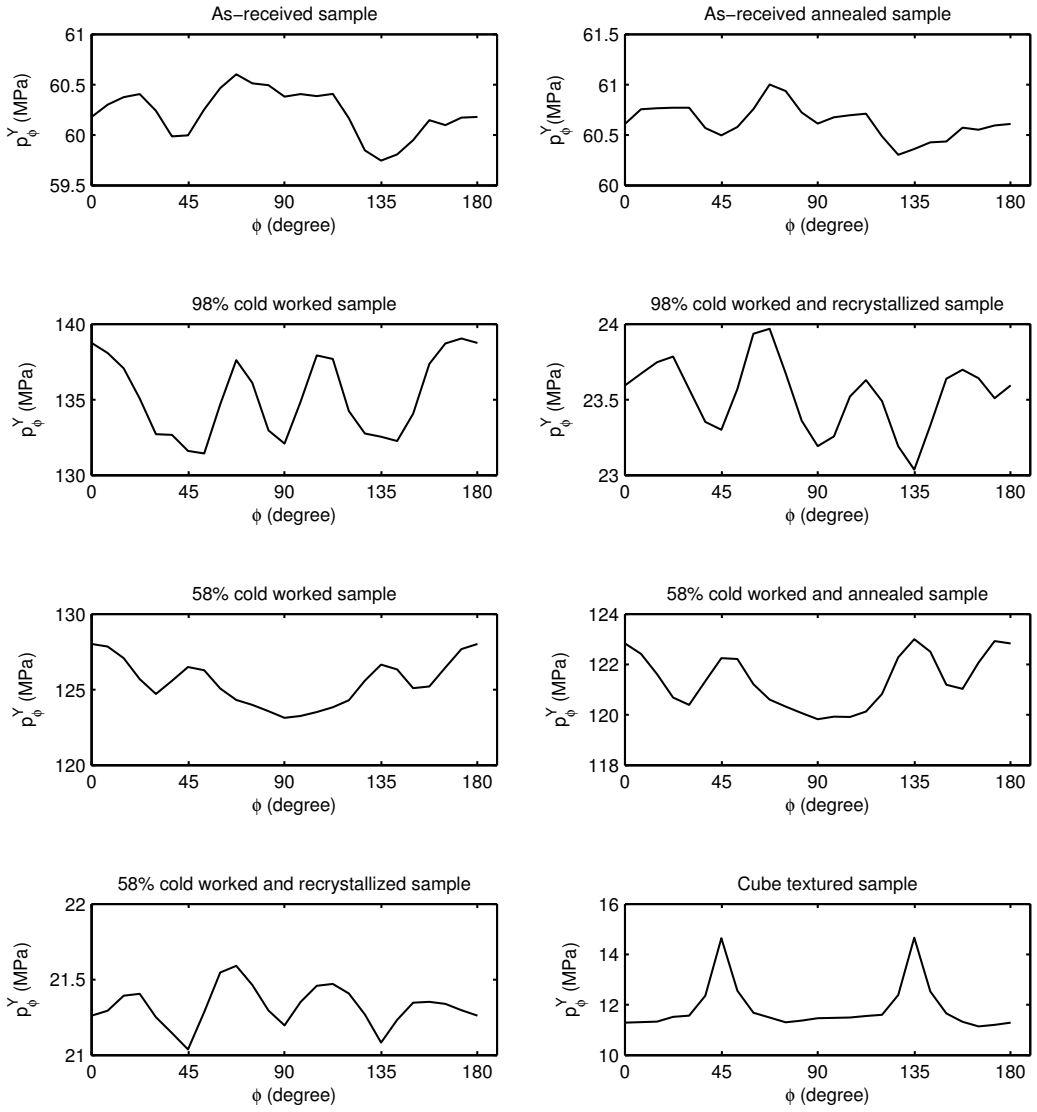

Figure 2.5: A variation in yield strength with respect to the applied tensile load direction in anisotropic plates with a circular hole

Table 2.3: The performance of anisotropic plates with a circular hole

Samples	*Performance*	*Stress Concentration* K_t	*Applied Tensile Yield Strength* (p_ϕ^Y) *(MPa)*	*Angles from the Sample Rolling Direction (degrees)*
As received	max	2.9998	60.6029	67.5
	min	3.0138	59.7461	135
As received and annealed	max	2.9999	61.0013	67.5
	min	3.0087	60.3045	127.5
98% cold worked	max	2.9951	139.0507	172.5
	min	3.0471	131.4412	52.5
98% cold worked and recrystallized	max	3.0000	23.9691	67.5
	min	3.0145	23.0364	135
58% cold worked	max	2.9255	128.0214	0
	min	2.9526	123.1271	90
58% cold worked and annealed	max	2.9596	123.0033	135
	min	2.9543	119.8268	90
58% cold worked recrystallized	max	2.9998	21.5910	67.5
	min	3.0146	21.0382	45
Cube texture	max	2.4672	14.6613	135
	min	2.4823	11.1397	165

performance condition among the materials of the database becomes: $2.46 < K_t < 3.05$ or a factor of 1.2.

2.5 Chapter Summary

This chapter presents a new approach to first-order yield limited elastic/plastic design, by introducing the Hybrid Bishop-Hill model for yielding. The HBH model retains the distinctive corner stress states defined for FCC crystals by the classical Taylor Bishop-Hill model, but differs in focusing the choice of corner stress state upon the macroscopic applied stress. In a comparison between the TBH and HBH models, undertaken for a database of 8 distinctive OFE Cu materials, it was demonstrated that the HBH model performed markedly better than the TBH model when compared with experimentally measured yield strengths.

A semi-complete (complete in the E direction) properties closure for in-plane uniaxial yield strength versus Young's modulus was presented, and compared with an accessible property closure for the database of 8 OFE Cu materials. In addition to the varied secondary processing by thermal-mechanical treatment, rigid body rotation of these sheet materials, about the sheet normal, was

considered. The variation of yield strength and Young's modulus with rotation define orbits within the properties closure. These orbits were detailed in the accessible property closure.

To illustrate the application of the new HBH model to a yield limited design problem of general interest, the problem of yielding in anisotropic plates containing circular hole was considered. Anisotropic plate theory predicts that the location of maximum stress concentration is dependent on material microstructure such that the stress concentration is not necessary located at 90 degrees off the applied tensile load axis, as in the isotropic plate theory, but varies with material microstructure and loading direction in the plate. The study shows that the variation of load capacity is large for highly textured samples. In the identified optimal direction, it is predicted that the applied stress at yield is about 34% of the tensile yield strength in the rolling direction for most samples compared with 33% for isotropic materials. For the cube-textured material, it is about 50% of the tensile strength (ultimate tensile strength for plate with no hole). If the performance of the plates is based upon the stress concentration factor K_t (Eq. 2.20), it does not change significantly with direction of the applied tensile load.

This section of work has presented a new approach for improving the performance of simple mechanical parts by incorporating material microstructure information into a stress-centric framework. Since the stress is much more accessible than the plastic strain, near the yield point of the material, the new approach facilitates a much easier approach to yield limited design. As an example of the application of the new yield theory we have shown that the locations of stress concentration, the optimal/critical applied load directions, and the readily accessible direction-dependent yield strength predictions aid the design for improvement of overall performance of plates containing a circular hole.

CHAPTER 3. HYBRID BISHOP-HILL MODEL COMBINED FINITE ELEMENT ANALYSIS

3.1 Chapter Overview

To achieve excellence in mechanical design, engineers may consider various aspects of design, including geometry of a structure, processing strategy and material microstructure. Optimizing any of these parameters lead to enhancement of performance of products. This chapter will focus primarily on the optimization of material microstructure, termed microstructure sensitive designing [12]. However, in practice none of these design parameters can be treated in isolation; hence the interactions between all three will be considered in a framework focused on design for yield in polycrystalline metals.

In general design practice today, engineers use readily available tables of material data (such as properties derived from standard uniaxial tensile tests) which assume an isotropic nature for materials. In reality, many of the materials have anisotropic properties and preferred crystal orientations relating to their microstructure. By using methodology based upon microstructure sensitive design and introducing the anisotropic properties of materials into the design space, new possibilities arise in performance which may have been missed by the standard design approaches.

An evaluation of the elastic/yield limit is a critical aspect of many mechanical design activities. Several microstructure-based theories have been offered for the prediction of yielding in polycrystalline materials such as Taylors model [8], the Bishop-Hill model [1, 2], and various intermediate or hybrid models [9, 24–31]. These classical models are focused upon integrating crystallographic texture (the preferred distribution of lattice orientations) into yield predictions. Typically a critical resolved shear stress is required as an input to properly scale the predictions of measured yield properties.

It is important to note that under the classical Taylor Bishop-Hill methodologies [1, 2, 8], plastic strain states must be specified in order to evaluate the yield stress. The difficulty is that, for

designing problems focused upon initial yielding, the elastic and plastic components of the total strain are comparable in magnitude and difficult to separate. Thus, the precise condition of plastic strain at initial yielding is not precisely specified. It follows that application of these classical microstructure-based theories of plasticity to initial yielding is a rather imperfect approximation at best.

This section of the work will focus on a Hybrid-Bishop-Hill (HBH) model [10] which is closely related to the classical Bishop-Hill model [1,2] in predicting local stress states and mechanical yielding. The HBH model has the advantage, when used in the context of part design, of greatly expanding the design space, thus enabling the designer to reach into traditionally unexplored areas of performance. Because the computational burden associated with the full characterization of the 5-dimensional anisotropic yield surface is prohibitive, a reduced representation of the yield surface that is much more accessible is developed. Typically only a small portion of the complete yield surface is required for part design and the HBH model facilitates rapid access to the pertinent domain of the yield surface.

One of the most flexible design tools for determining local stress state, as an input to the HBH model, is Finite Element Analysis (FEA). Many physical phenomena are studied through differential equations, with given boundary or initial conditions that may be solved numerically via FEA techniques. FEA allows designers to study distributions of stress and displacement in complex physical/geometrical models which may not have analytical solutions; thus enabling engineers to evaluate structural integrities as part of the design process. Hence the incorporation of an HBH model into the FEA framework is an ideal partnership for studying yield behavior in the context of anisotropic materials.

This chapter will demonstrate the anisotropic material dependent HBH / FEA analysis with three different geometries. The first geometry of this study is the classical 'anisotropic hole-in-plate problem' (3.1). While many geometrical models do not have analytical solutions to the associated stress field, an infinite plate having a circular hole is one of the relatively few geometry problems which have analytical solutions. Lekhnitskii explains that the stress states around a circular hole of infinite plate can be expressed in terms of material information in the following form [13]:

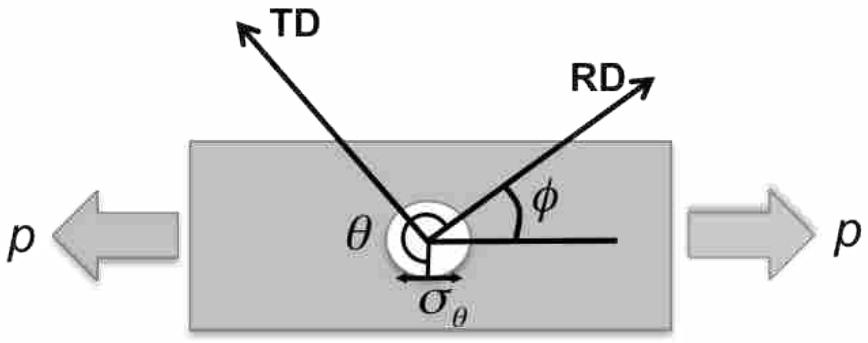

Figure 3.1: A geometry of anisotropic hole-in-plate problem

$$\begin{aligned}\sigma_\theta = p\frac{E_\theta}{E_1}\{&[-\cos^2\phi + (k+n)\sin^2\phi]k\cos^2\theta \\ &+ [(1+n)\cos^2\phi - k\sin^2\phi]\sin^2\theta \\ &- n(1+k+n)\sin\phi\cos\phi\sin\theta\cos\theta\}.\end{aligned} \tag{3.1}$$

In this expression p is the applied stress, exerted a large distance away from the circular hole. θ defines an angle relative to the selected principal material axis that identifies the location of a point on the circumference of the circular hole. σ_θ is defined to be the tensile stress tangential to the point on the circumference identified by θ. ϕ denotes the direction of the applied stress with respect to the principal material axis (Figure 3.1). Other components in Eq. 3.1 are defined by the expressions:

$$\begin{aligned}\frac{1}{E_\theta} &= \frac{\sin^4\theta}{E_1} + (\frac{1}{G} - \frac{2\nu_1}{E_1})\sin^2\theta\cos^2\theta + \frac{\cos^4\theta}{E_2} \\ k &= \sqrt{\frac{E_1}{E_2}} \\ n &= \sqrt{2\frac{E_1}{E_2} - \nu_1 + \frac{E_1}{G}}.\end{aligned} \tag{3.2}$$

The symbol ν_1 represents Poisson's ratio perpendicular to the principal material axis, E_1 and E_2 represent Young's modulus in the rolling and transverse directions of the sheet, respectively, and G is the in-plane shear modulus. Given the traction-free condition at the circumference of the hole,

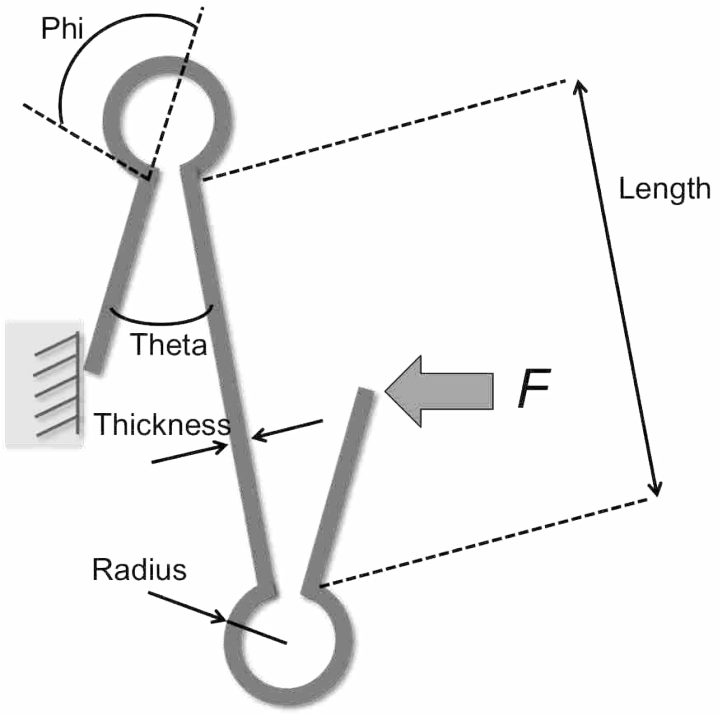

Figure 3.2: Parameters for a stent-like compliant mechanism

and the other geometrical and boundary conditions, σ_θ is the only non-zero component of stress that can occur adjacent to the circular hole.

The second and third examples studied in this work are geometries relating to compliant mechanisms, as illustrated in Figure 3.2 and Figure 3.3. A stent-like geometry (Figure 3.2) experiences displacement loading from an applied force F. A geometrical part from a lamina emergent torsional (LET) joint [32, 33] (Figure 3.3) experiences simple loading conditions which create different complex stress states within the geometry of the part.

The study aims to demonstrate how to achieve excellence in elastic/yield-limited design by introducing material anisotropy using these simple geometries. The FEA is carried out on the geometrical parts for the anisotropic material properties of oxygen free electronic (OFE) polycrystalline copper, which are obtained from microstructure analysis over a range of processing options. The stress states of each node, which are evaluated via FEA, are studied with the HBH yielding model.

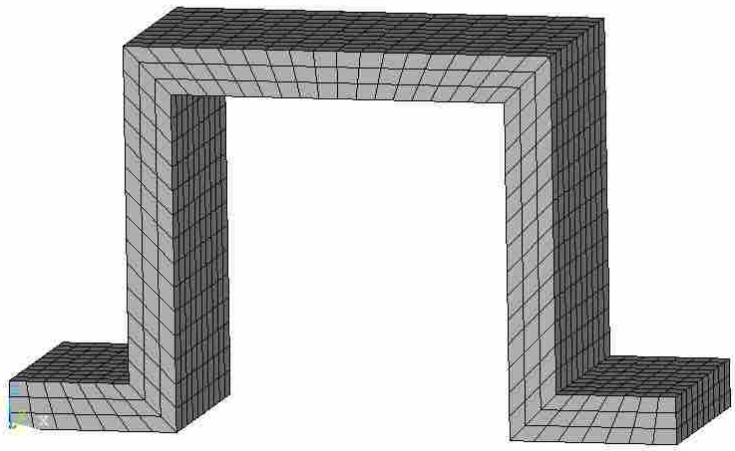

Figure 3.3: A basic unit of a lamina emergent torsional joint

3.2 Methodology

3.2.1 Anisotropic Material Properties

The term 'local state' refers to any local characteristics of materials that affect the properties of interest. The 'local state distribution' refers to how the components of microstructure, such as crystal orientations, are distributed across the set of possible local states. Only one material phase is present in OFE Cu polycrystals - the FCC Cu phase; impurity levels in this material are small. It is assumed that the local elastic state of the materials is determined only by the orientation of the crystal lattice, and by the basic elastic properties of the Cu phase.

The simplest way to connect the distribution of local states of microstructure to estimates of the macroscopic (effective) elasticity is to utilize a rule of mixtures (or an inverse rule of mixtures) approach; i.e. to use only volume fraction information of the distribution. Such information is often referred to as 'first-order' information of the microstructure.

One set of first-order bounding relations on the elastic properties is called the Hill-Paul bounds [11]. The Hill-Paul upper- and lower-bounds on the elastic properties are shown in the following expression where $\overline{S}_{ijkl}$, and $\overline{C}_{ijkl}$ denote the volume averaged elastic compliance tensor and stiffness tensor:

$$\overline{S}^{-1}_{ijij} \leq C^{eff}_{ijij} \leq \overline{C}_{ijij}. \tag{3.3}$$

Because of the assumptions made in the derivation of the above bounding relation, the bounds hold only for the diagonal elements of the elastic stiffness tensor [11,12,20,21]. The derivation for bounding relations for off diagonal elements of the stiffness tensor requires a more sophisticated approach, based upon the positive definite property of the elastic tensor. Taking the arithmetic means of the upper bound and the lower bound is called the Hill average [14,34]. The Hill average applies to both diagonal and non-diagonal components of the elastic properties:

$$C_{ijkl}^{eff(Hill)} \approx \frac{\overline{S}_{ijkl}^{-1} + \overline{C}_{ijkl}}{2}. \tag{3.4}$$

To determine the distribution of local states within the material, it is first necessary to define the pertinent local state space. The crystal orientation, g, governs the anisotropic nature of the material, and is the local state variable of principal interest here. Various parameterizations of g are available, but the Bunge Euler angles, ϕ_1, Φ, ϕ_2 , are the most common [14]. These define a sequence of three primitive rotations that are required to bring a sample-fixed coordinate frame into coincidence with the lattice fixed frame on $\langle 100 \rangle$. Output of the Bunge Euler angles is commonly available using established image processing applied to EBSD patterns [15]. Each data point belongs to the complete Bunge-Euler space (FZ_T) [14]:

$$FZ_T = \left\{ g \equiv (\phi_1, \Phi, \phi_2) \left\| \begin{matrix} 0 \leq \phi_1 < 2\pi \\ 0 \leq \Phi < \pi \\ 0 \leq \phi_2 < 2\pi \end{matrix} \right. \right\}. \tag{3.5}$$

The cubic lattice possesses 24 rotational symmetries; thus a reduced subspace is available within FZ_T that includes only one of the 24 physically equivalent lattice orientations of the local crystal [11]. However, a reduced fundamental zone has a non-rectangular shape that is difficult to deal with for efficient binning and computational operation. When symmetry of the FCC crystal lattice is fully considered, it is convenient to express a 3-fold redundant space of possibilities for

ϕ_1, Φ, ϕ_2: [12]

$$FZ_{3c} = \left\{ g \equiv (\phi_1, \Phi, \phi_2) \left\| \begin{array}{l} 0 \leq \phi_1 < 2\pi \\ 0 \leq \Phi < \dfrac{\pi}{2} \\ 0 \leq \phi_2 < \dfrac{\pi}{2} \end{array} \right. \right\}. \tag{3.6}$$

The 3-fold redundancy refers to the fact that each physically distinctive lattice orientation appears 3 times in FZ_{3C}. Further reduction to the point that each distinctive orientation appears only one time is possible, but the inconvenience is that the fundamental zone contains a complex surface, which renders partitioning difficult. Experience dictates that it is easier to work with the rectangular 3-fold redundant fundamental zone described by Eq. 3.6. From the experimental point of view, each EBSD-based measurement of lattice orientation will occur 3 times in FZ_{3C}.

The rectangular shape of FZ_{3C} can be split into smaller bins of rectangular shape. All computations of the type required in Eq. 3.4 will be handled discretely, using binned datasets. Suppose that N such bins have been defined on FZ_{3C}, with a given bin designated by ω_n, where

$$\omega_n \subset FZ_{3c}, \quad \bigcup_{n=1}^{N} \omega_n = FZ_{3c}, \quad \omega_n \cap \omega_m = \oslash \ (m \neq n). \tag{3.7}$$

Associated with each bin ω_n is an indicator function $\chi_n(g)$, defined by the expression.

$$\chi_n(g) \equiv \chi_n(\phi_1, \Phi, \phi_2) \begin{cases} 1, & if \ g \in \omega_n \\ 0, & \text{otherwise} \end{cases} \tag{3.8}$$

The size of the bins will have an effect upon the errors in forming the averages required by the Hill estimates of effective elastic stiffness.

The pertinent local state distribution is the distribution of lattice orientation among the sampled material points. Imagine that a total of S local orientations have been measured by EBSD-based methods. A condition of statistical sufficiency is assumed for this set of measurements. Roughly, this means that the measurements are taken in a sufficiently large number of components of microstructure (grains) to ensure that the experimental sampling is characteristic of the overall microstructure. After converting each of the S measurements of orientation into it's 3 equivalent

orientations within FZ_{3C}, the $3S$ determined orientations will be distributed among the N defined bins. Let f^n denote the fraction of $3S$ orientations that fall within ω_n:

$$f^n = \frac{1}{3S}\sum_{s=1}^{3S} \chi_n\{g_s\}. \tag{3.9}$$

The local state distribution function, in this case closely related to the orientation distribution function [11, 12], will consist in the set of real number fractions f^n, $F = \{f^1, f^2, \cdots, f^N\}$. From Eq. 3.9, conservation of volume requires that

$$\sum_{n=1}^{N} f^n = 1. \tag{3.10}$$

Approximations to the average elastic tensors required in Eq. 3.4 are readily formed from the local state distribution function via expressions of the form

$$\overline{C}_{ijkl} \approx \sum_{n=1}^{N} f^n C^n_{ijkl} \tag{3.11}$$

where C^n_{ijkl} denotes the value of the elastic stiffness associated with orientation ϕ_1, Φ, ϕ_2, taken to be a characteristic lattice orientation lying within the associated bin ω_n. Numerical examination of the bin-size dependency of calculations like Eq. 3.11 have determines that numerical errors (the error compared with an infinitesimal bin size) are $\sim 1\%$ when a bin size of $9^\circ \times 9^\circ \times 9^\circ$ in the three Euler angles is selected within FZ_{3C}; consequently, this bin size was utilized throughout this chapter.

3.2.2 Elastic-Yield Property Closures

Interest in the complete range of elastic/yield property combinations that could occur within all conceivable polycrystalline microstructures of fixed material phase typically arises during preliminary design. This envelope of property combinations is termed a property closure, and a designer would choose an area of the closure that provides optimal properties for the component to be produced. Theoretical methods for constructing estimates of properties closures have been presented in the literature [11, 12, 20, 21]. The approach taken is to make use of available

microstructure-sensitive homogenization relations of the properties of interest, and then to consider all possible microstructures beginning with single crystals of an arbitrary lattice orientation.

The framework presented in this work will be directly applicable to full property closures. However, one frequently raised issue with full property closures is the lack of defined processing techniques for arriving at any given defined microstructure. Hence, for the test-beds presented here we will utilize only subsets of the full closure that are associated with a limited set of microstructures associated with known manufacturing processes.

3.2.3 OFE Copper Materials

Eight differently textured oxygen free electronic (OFE) copper samples have been prepared for the study using three common processing methods: rolling deformation, thermal annealing and rigid body rotation of the material about the normal direction to the rolling plane. Rolled OFE Cu plate (in the as-received half-hard condition), and six derivative materials produced there-from by secondary processing steps, plus one addition material (very strongly cube textured Cu, provided by Dr. Amit Goyal of Oak Ridge National Laboratory) constitute the database. Table 3.1 describes the processing conditions for each of these samples.

Table 3.1: Sample description

Sample Description	*Heat Treatment Temperature (C°)*	*Heat Treatment Time (Hour)*
As received	N/A	N/A
As received and annealed	191	1
98% cold worked	22	N/A
98% cold worked and recrystallized	225	0.5
58% cold worked	N/A	N/A
58% cold worked and annealed	160	1
58% cold worked and recrystallized	225	1.5
Cube texture	N/A	N/A

Each material is rotated in $\pi/24$ radian ($\phi = 7.5$ degree) steps about the sheet normal direction to give 48 different possible microstructures for a given material type. Anisotropic material properties were obtained from Eq. 3.4 for each given rotation and applied to ANSYS

(ANSYS®Academic Research, Release 13.0). The performance of each design was determined in terms of the minimum safety factor and related configurational yield stress.

3.3 Finite Element Analysis - ANSYS

3.3.1 Hole-in-Plate Problem

To carry out FEA analysis that accurately represents an infinite plate condition the dimensions of the plate and hole are selected carefully. The ratio of circular hole and plate dimension needs to be chosen in a way such that the stress field around the hole of the modeled finite plate is similar to that of an infinite plate. The study will follow St. Venant's Principle to create such a condition. The principle states that the resultant forces become negligible at a large distance away from the dimensions of the part when the system of forces and moments are statistically equivalent. By utilizing St. Venant's principle, the ratio between plate and hole dimensions were determined.

The geometry of the problem is based on the gage length of ASM standard tensile test specimen dimensions. The length of the plate is 2 inch (50.8mm) and the width of the plate is 0.5 inch (12.7mm). Since the stress field due to a circular hole of diameter, d, is localized within $\sim 3d$ from the geometrical discontinuity, the hole needs to be located at least $\sim 3d$ from the discontinuity (the edge of the plate). Hence a $1/6$ inch ($d = 0.794$mm) drill size hole is chosen for the study.

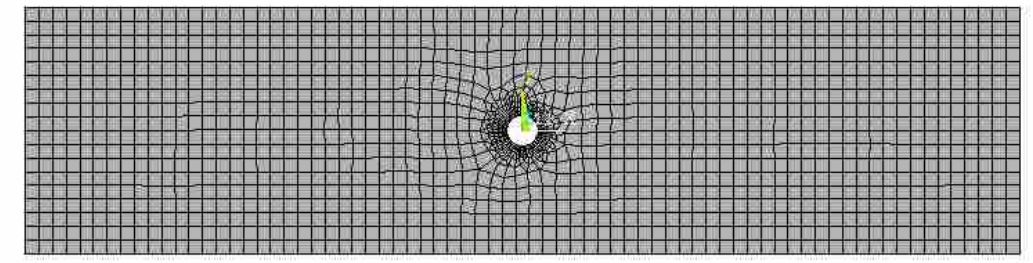

Figure 3.4: Meshing of hole-in-plate example in ANSYS

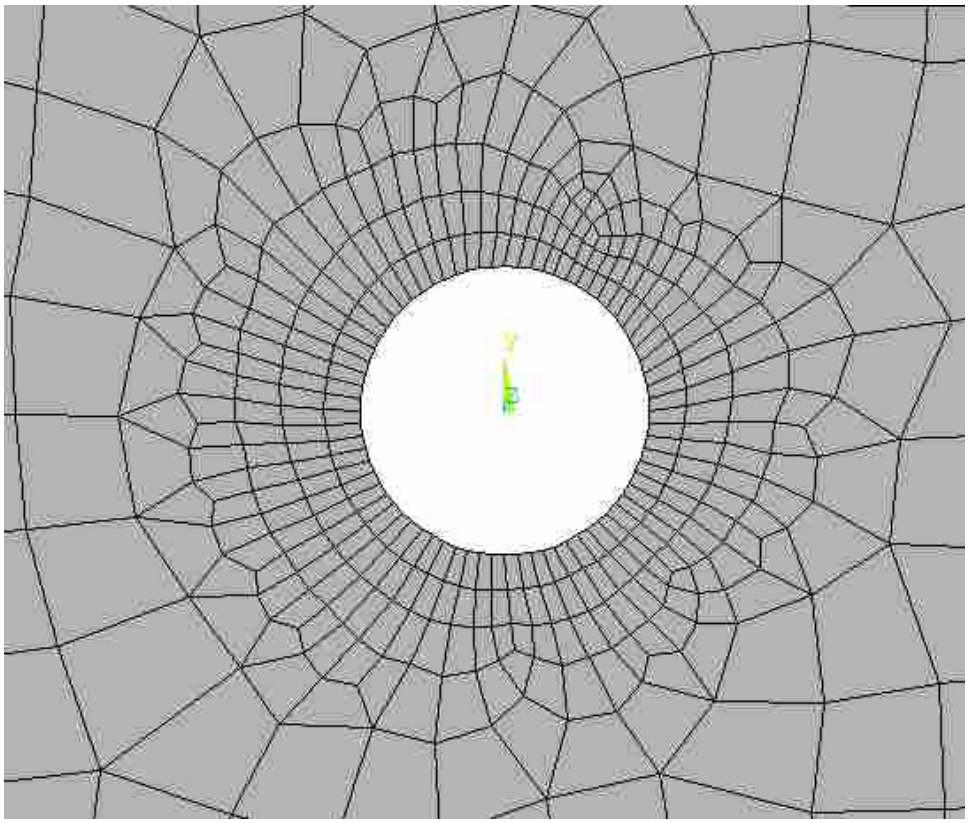

Figure 3.5: Closer view of ANSYS meshing around hole circumference of Figure 3.4

The plate experiences a tensile load which is approximately a plane stress case; thus the study employs two dimensional stress analyses. One end of the plate is fixed in the direction and the other end experiences the applied tensile load which is distributed over the relevant nodes.

The FEA simulations are carried out in ANSYS using element type Plane-183 as 2-dimensional stress analysis with mesh size 0.700 mm quadrilateral shape. The mesh around the hole circumference is refined to give nodes at 5 degree increments. 21 anisotropic properties obtained from Eq. 3.4 are employed in the simulations. The stress states of 72 nodes on the hole's circumference are selected to be further studied by the HBH yield model.

3.3.2 A Stent-Like Compliant Geometry

The dimension of a compliant geometry is shown in Table 3.2 and Figure 3.2. The structure experiences a displacement loading along the x-axis due to an applied force F (Figure 3.2). One end is fixed, and other end segment experiences the applied load in the negative x-direction.

Table 3.2: Dimension of a stent-like geometry

Dimensions	*Value*	*Unit*
Length	1.00	mm
Thickness	$2.50e^{-2}$	mm
Theta	30	degree
Radius	$5.00e^{-2}$	mm
Phi	80	degree

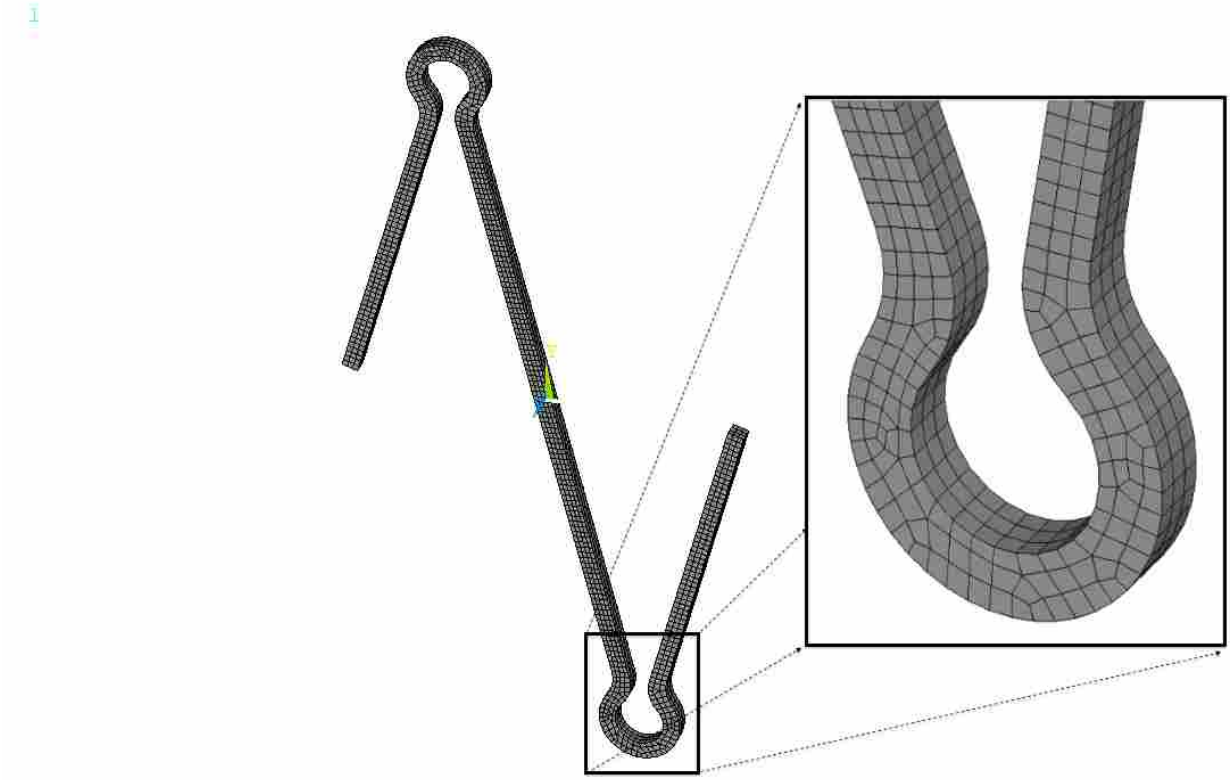

Figure 3.6: ANSYS meshing of a stent-like geometry

The ANSYS model executes FEA analysis with Solid-185 elements with 8-nodes. Only about 5% of the nodes experiences high stress, these being located at the bend section of the geometry; thus, the study focuses on the 70 nodes located in this segment.

3.3.3 A Lamina Emergent Torsional Joint

The dimensions of a single LET joint are shown in Table 3.3. One end of the joint is fixed and the load is applied to the segment at the other end (see Figure 3.7 and Figure 3.8). Two different loading conditions are applied to the compliant joint: loading in the plane of the page and out of the plane of the page. Additionally, each loading condition was applied under homogeneous (texture, and related elastic properties, are constant throughout the sample) as well as heterogeneous (texture, and related elastic properties, vary along the sample) conditions. The homogeneous condition represent a part that is cut out from a sheet of material such that all points in the part have the same rolling direction. Meanwhile, the heterogeneous condition represents a part that is bent to its final shape from a sheet of metal such that the rolling direction follows the direction of each leg, and therefore changes with respect to the global frame along the part. In each condition the rolling direction is rotated in 7.5 degree increments about the sheet normal direction (out of the page direction in Figure 3.7 and Figure 3.8) to test the component response with the accompanying change in texture with respect to the global frame.

Table 3.3: Dimension of a LET joint

Dimensions	*Value*	*Unit*
Length	4.78	mm
Thickness	0.787	mm
Width	6.35	mm
Force (in plane)	1.56	N
Force (out of plane)	1.56	N

The ANSYS model uses the Solid-186 element type. The applied load is decomposed into coupled forces, such that the resulting forces are distributed over all nodes of the relevant surface.

3.4 Hybrid Bishop-Hill Model

The Hybrid Bishop-Hill Model (HBH model) is a modified version of the Taylor-Bishop-Hill (TBH) model. In the TBH model, the yield locus is defined in a five dimensional deviatoric stress space, and each stress state is expressed in term of a critical resolved shear stress. The

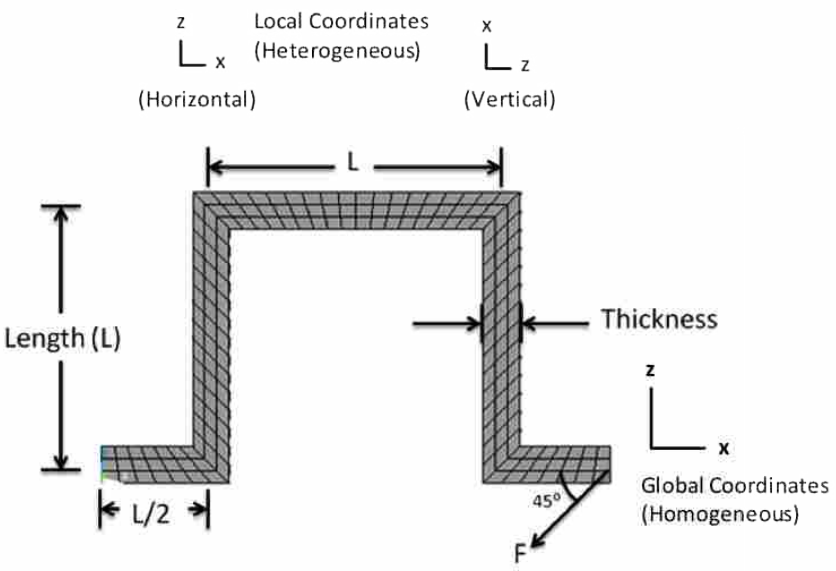

Figure 3.7: In-plane loading with homogeneous vs. heterogeneous coordinates with schematic simplified

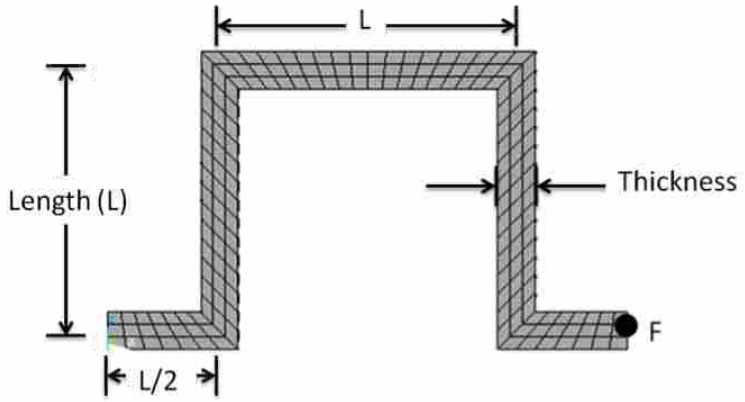

Figure 3.8: Out-of-plane loading with schematic simplified

TBH model predicts the existence of a convex polyhedron shaped yield surface, which has 56 vertices [1] for FCC materials. The TBH model states that for FCC materials a set of 56 stress states (also known as stress corners) is capable of activating the required combinations of slip for an arbitrary plastic deformation. This is a strain-based model: each grain experiences the uniform imposed (macroscopic) strain and the active corner stress state is the one that maximizes the plastic work done.

The HBH model, on the other hand, is a stress-based model and uses the same stress corners defined by the TBH model to predict the yield strength of polycrystalline materials. The model reflects the natural heterogeneity of the constituents of the polycrystal. The magnitude of the corner stress states requires knowledge of a critical resolved shear stress τ_{crss}. This stress defines the level of shear stress that must be present upon any of $\{111\}\langle 110\rangle$ slip systems to cause dislocation slip to occur. It is known that τ_{crss} is proportional to the square root of the local total dislocation density [35] which typically varies with position x. However, in the present work τ_{crss} is obtained from combinations of mechanical tensile test and numerical calculations by the use of a contractile (plastic) strain ratio approach; thus τ_{crss} will be held constant for any specified material condition within the database. For methodologies to determine τ_{crss}, please refer to the following publication [10, 36].

Some of the advantages of using HBH model are that it focuses on applied stress, rather than on the plastic strain; this makes the model much more accessible to design engineers who focus more upon stress states, rather than strain states. Furthermore, HBH model works superior to the TBH model at near-vicinity of the yield surface due to reasons discussed earlier (in Section 3.1).

The HBH model makes a simple assumption that the local yielding at any position in the material occurs at the corner stress states, $\hat{\sigma}_{ij}^{C}$, that lies "closest" (by some definition) to the macroscopic stress, $\hat{\sigma}_{ij}$. The "hat" over the stress symbols signifies the deviatoric stress. Distance between these two stress states is defined by d_{ij}, where

$$d_{ij} = \hat{\sigma}_{ij}^{c} - \hat{\sigma}_{ij}. \tag{3.12}$$

The magnitude of distance between stress states, d, is defined by the Euclidean norm:

$$||d^2|| = d_{ij}d_{ij}. \tag{3.13}$$

Importantly, the distance defined according to Eq. 3.12 and Eq. 3.13 is invariant with respect to coordinate transformation. The selection of stress corner for any particular component (grain) within the polycrystal is taken to be the Bishop-Hill corner stress that minimizes the distance d between the applied stress and the corner stress state.

The estimated (deviatoric) yield strength of the material is obtained by averaging over the texture components in the sample using the expression.

$$\hat{\sigma}_{ij}^{Y} \approx \sum_{n=1}^{N} f^{n} \hat{\sigma}_{ij}^{Cn} \tag{3.14}$$

$\hat{\sigma}^{Cn}$ denotes the pertinent active stress corner associated with bin n in FZ_{3c}. Note that all corner stress states exercised in Eq. 3.14 must be expressed for the current and local stress condition in the macroscopic (sample) frame in order to interpret $\hat{\sigma}_{ij}^{Y}$ as the yield strength.

In this study, we introduce the notion of safety factor, λ, to determine the material tendency to yield. The local stress state from each node in the FEA model is projected on to the closest (active) corner stress state. The stress state is then scaled so that the magnitude of local stress becomes equal to the magnitude of the active corner stress; i.e. the local stress state touches the yield surface defined by the active corner stress. If the safety factor works out to be 1, or smaller than 1, the material has yielded. In other words, when the safety factor is greater than 1, the material won't fail because the stress states are within the yield limit.

For a given design (e.g. a hole-in-plate problem) the smallest safety factor defines the yield limit of the design. An estimate of macroscopic stress that results in yield is obtained by multiplying the applied stress by this smallest safety factor; this is termed the *configurational yield stress*.

The yield stress of a part is dependent on its geometry and how it experiences the external load. ANSYS simulations relate an applied load on the plate to the local stress state. The configurational yield stress indicates the component yield stress by considering the applied stress instead of the local stress. The methodology includes the geometrical information via the safety factors obtained from each node and provides the local stress level. To connect the local stress to the macro level, the applied load is multiplied by the minimum safety factor (or minimum averaged safety factor over a minimum yield area), giving the configurational yield stress.

The process used in the HBH incorporated FEA simulations are follows:

1. Choose the applied load p and the applied load direction ϕ

2. Obtained stress states σ_{ij} in nodes around the hole's circumference from ANSYS

3. Send σ_{ij} to the HBH model to obtain the safety factor λ

   (a) $\lambda \leq 1 \rightarrow$ material has yielded

   (b) $\lambda > 1 \rightarrow$ material has not yet reached the yield surface

4. Choose the smallest safety factor λ_{min} in each ϕ orientation

5. Find the configurational yield stress for each configuration by multiplying each minimum safety factor by applied load: $\lambda_{min} \cdot p$

The magnitude of applied stress p used in ANSYS simulations for the hole-in-plate problem is chosen to give proximity to the elastic/yield limit (Table 3.4), and determination of the values are based on a yield limit study using the analytical approach [10].

Table 3.4: List of applied load in ANSYS simulations

OFE copper materials	*Applied Load: p (MPa)*
As received	60
As received and annealed	60
98% cold worked	135
98% cold worked and recrystallized	23.5
58% cold worked	125
58% cold worked and annealed	122
58% cold worked and recrystallized	21.5
Cube texture	12

In the case of compliant geometries, instead of finding the smallest safety factor λ_{min} in each orientation and sample, the simulations find the average λ to evaluate the overall response of a given mechanical design (for those nodes under consideration). Hence, the HBH approach calculates an average λ in step 4 and determines the overall performance. This provides a different approach to the definition of component failure that may be more appropriate in some instances.

3.5 Validation of FEA Approach

The hole-in-plate problem provides a simple analytical validation of the FEA approach. However, one should keep in mind that the HBH incorporated FEA approach and analytical HBH

model have different approaches. The difference lies in how material information is incorporated into simulations: the difference in how stiffness/compliance tensor elements are used. Recall (from Eq. 3.1 and Eq. 3.2) that the analytical procedure assumes a 2D orthotropic material; i.e. the analytical method assumes only 4 independent components in the compliance tensor. On the other hand, the FEA approach incorporates a full set of 21 (possibly independent) components for the stiffness tensor in its simulations. This difference in approach brings about small variances in yield surface, and from the reasons above, it is natural to predict that FEA approach gives more accurate results than the analytical method.

The stress states around the hole of cube-textured sample using the analytical method (Eq. 3.1 and Eq. 3.2) are shown in Figure 3.9. The stress is shown at every 5 degree increment in θ. Results for applied loads along the rolling direction (RD; $\phi = 0$) and at $\phi = 45$ degrees and $\phi = 90$ degrees from RD are shown. The same stress states calculated using the ANSYS model are shown in the same figure (Figure 3.9); each nodal stress is expressed in terms of the von Mises stress. The analytical method gives much higher peak stress in the 45 degree orientation compared to the FEA simulations. However, in general the figure confirms that the analytical and the FEA gives consistent stress profile.

The result of the ANSYS incorporated HBH simulation is shown in Figure 3.10. The stress on each node is put into the HBH model, and safety factors are obtained. The safety factor of each node is plotted in Figure 3.10; larger safety factors indicate that the material is not likely to yield. A minimum of the graph, or minimum stress, occurs at $\theta = 65$ degree on the hole circumference for $\phi = 0$, and 90 degree orientations. The applied macro stress is 12 MPa, and minimum safety factor at this location is $\lambda = 1.43$ (Figure 3.10). The configurational yield stress is the multiplication of applied macro stress and minimum safety factor; thus the yield stress is 17.2 MPa for this configuration ($\phi = 90$ degree). This configurational yield stress suggests that this is the required macro stress to yield the plate at some point on the component. The minimum safety factors for 45 degree orientation are slightly larger than for the 0 and 90 degree configurations, indicating that a 45 degree orientation is preferable compared to the other two orientations shown here, for a cube-textured material.

Figure 3.11 shows the analytical stress and the FEA calculated stress for the cube texture sample. In general, the analytical and FEA models give similar stress levels. However, close obser-

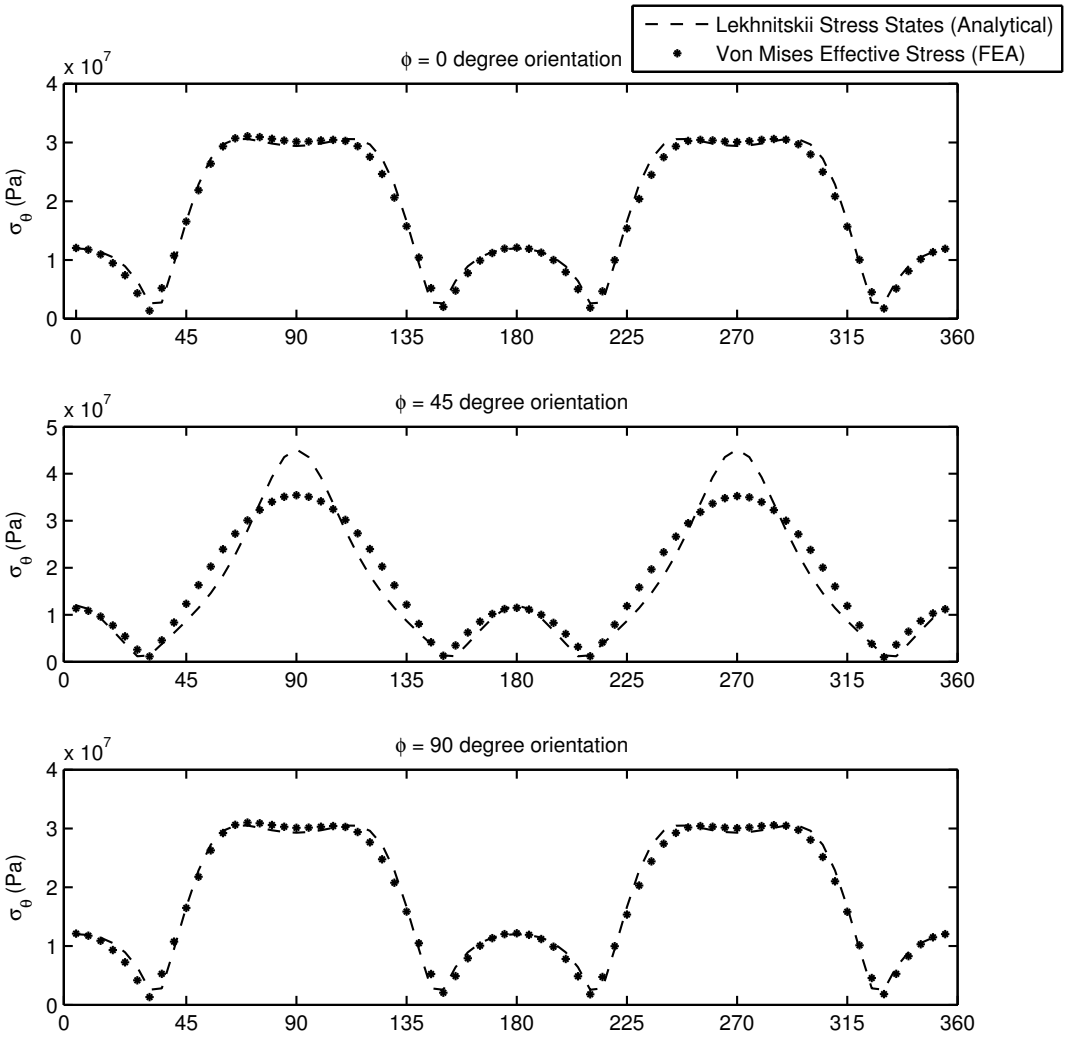

Figure 3.9: Stress states around a hole of cube texture sample

vation near the yield limit (lower peaks) shows that the analytical approach gives lower estimates of stress compared to the FEA approach.

Table 3.5 shows the optimal configurational yield strength of hole-in-plate problems using both the analytical method and FEA method. The optimal yield strength of the plate is the best possible performance obtained from the plate when applying the load from different orientations. In other words, it is the yield strength of plate with orientation ϕ which gives the highest possible yield strength. Observation of the table indicates that the analytical approach consistently gives lower optimal yield strength compared to the FEA approach.

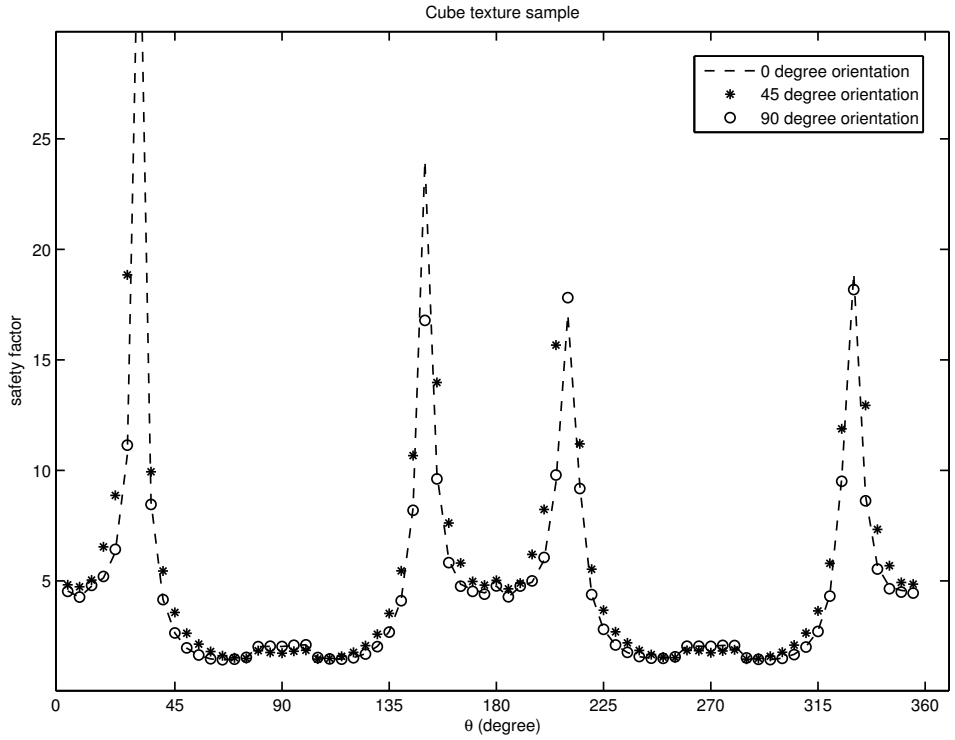

Figure 3.10: Local safety factors around the hole for cube texture sample in various applied load orientation

A previous study also indicated that the analytical HBH approach calculates a lower yield strength compared to the experimental results [10]. Since FEA utilizes all 21 components of the stiffness tensor, we postulate that while the two models are in reasonable agreement, the FEA results are likely to be more accurate.

3.6 Results

3.6.1 A Hole-in-Plate Problem

The locations of most likely failure, so called 'hot spots' around the circumference of the hole, are estimated using the HBH incorporated FEA model and presented in Tables 3.6 and 3.7 for sample with $\phi = 0$ and $\phi = 45$ degree.

When a plate with a circular hole experiences uniaxial tensile load, tangential stress states arise at the periphery of the hole. In the case of isotropic materials the highest tangential stress

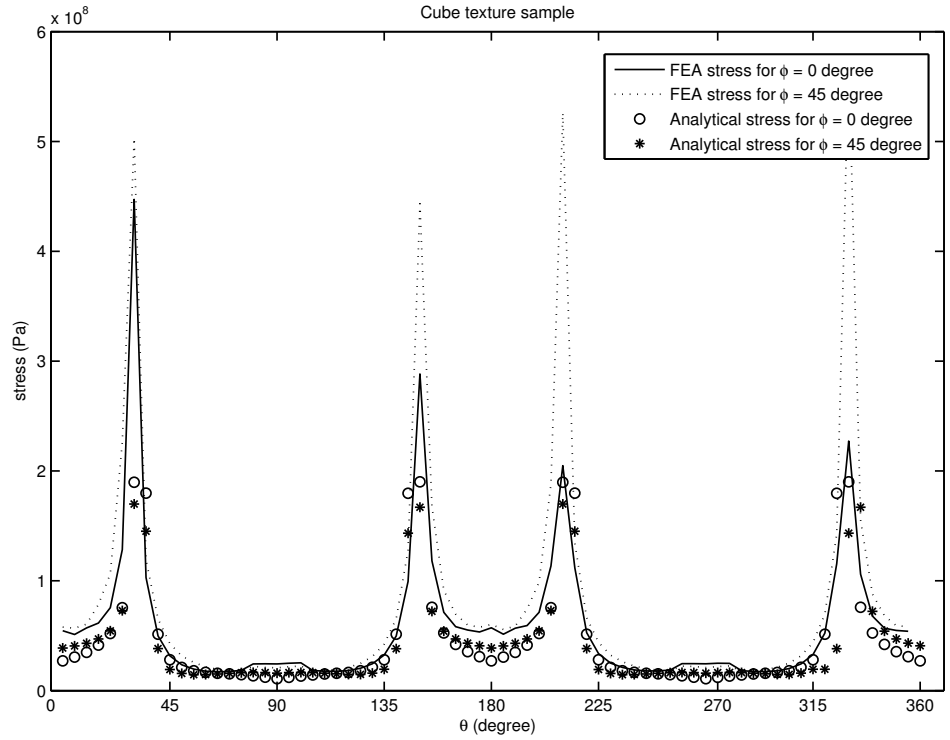

Figure 3.11: Local stress states around the hole for cube texture sample in various applied load orientation

occurs at locations perpendicular to the applied load ($\theta = 90$ and 270 degree). However, in the case of anisotropic materials the maximum tangential stress states may shift from the perpendicular locations. For example, the hot spot in 98% cold worked and 58% cold worked samples are somewhat shifted from the perpendicular locations. The cube-textured sample shows that the hot spots are located between 65 and 75 degrees from the loading direction when the load is applied at $\phi = 0$ and 45 degree from RD. Configurational yield stresses are calculated for each material type and each configuration (i.e. each value of ϕ) as discussed in the previous section. In order to assess the potential performance envelope of the different types of copper in a hole-in-plate situation we consider the property closure of these available materials in all possible configurations, which we term a "configurational sub-closure."

Figure 3.12 shows a configurational sub-closure for OFE copper with configurational yield stress as one of the material properties, and modulus as the other. Each of the 8 materials within the accessible database, are allowed to rotate around their plane normal in order to compute the

Table 3.5: Optimal yield strength of anisotropic plate

OFE copper materials	*Analytical Yield Strength MPa*	*FEA Yield Strength MPa*
As received	60.55	65.94
As received and annealed	60.96	66.70
98% cold worked	138.62	147.75
98% cold worked and recrystallized	23.88	26.50
58% cold worked	127.41	133.97
58% cold worked and annealed	122.75	129.47
58% cold worked and recrystallized	21.53	23.40
Cube texture	14.56	17.75

accessible property closure. Rotations of the sample relative to the loading direction give rise to orbits in the property closure. Further details relating to the production of sub closures are provided in the 2008 paper of Adams et al. [19].

The accessible property closures indicate that highly textured samples have larger closures in both the elastic and the yield limit. 98% cold worked, 58% cold worked, 58% cold worked-annealed, and cube-textured samples are such materials. The cold worked samples give larger variations in configurational yield strength. The percentage difference in performance (relative to the minimum configurational yield strength) is around 1 to 1.5% in cold worked samples and 3.5% in a cube texture sample. Although only small variations are seen, the configurational yield strength does depend on applied load direction (ϕ).

The small elliptical property closures for individual materials in Figure 3.12 imply that as-received samples and recrystallized samples in this study tend to have almost isotropic plastic properties [10, 19], thus the configurational yield strength does not vary very significantly with the direction of applied load.

3.6.2 A Stent-Like Compliant Geometry

A 0.400 mm displacement is applied to the stent-like compliant mechanism described in Section 3.3; the response of various OFE copper materials are shown with the average safety factor over the 72 most highly stressed nodes (Figure 3.13).

Table 3.6: 'Hot spots' of hole-in-plate geometry when applied load is along RD

OFE copper materials	*Location of most likely failure: 'hot spots' θ (degree)*
As received	90 270
As received and annealed	90 270
98% cold worked	95 275
98% cold worked and recrystallized	90 270
58% cold worked	85 265
58% cold worked and annealed	85 270
58% cold worked and recrystallized	90 270
Cube texture	65 115 250 295

The observation of performance with respect to material rotation reveals that highly textured samples, such as cube texture and cold worked samples, show significant directional dependent performance. The variation in performance is most high in the cube texture sample, with up to 34% improvement in performance when compared with the minimum average safety factor; the variation in cold worked samples is 2% to 3%. The difference in safety factors in other samples, such as recrystallized samples and as-received samples, are small; their performances are basically independent of material rotation. In general, improvement in performance due to sample rotation is much smaller than can be achieved by material section; only a few percent improvement results from rotation (except for the cube texture sample).

The best material and orientation for this design is the 98% cold worked material with an applied rotation of 135 degrees. This material selection gives an average safety factor of 0.640. The 58% cold worked and 58% cold worked-annealed material performed almost as well with safety factors of 0.584 and 0.566. The cube texture gives the worst performance ($\lambda = 9.60e^{-2}$)

Table 3.7: 'Hot spots' of hole-in-plate geometry when applied load is 45 degree from RD

OFE copper materials	*Location of most likely failure: 'hot spots' θ (degree)*
As received	90 270
As received and annealed	90 270
98% cold worked	95 275
98% cold worked and recrystallized	90 270
58% cold worked	85 265
58% cold worked and annealed	85 270
58% cold worked and recrystallized	90 270
Cube texture	75 105 255 285

although it has an interesting directional dependent performance. By comparing the best and worst performances, the best selection has 8.5 times the safety factor and can withstand much higher stresses without yielding. This difference in performance reflects both the effects of cold work (dislocation content) and texture. Some idea of the difference in performance that is only due to texture differences can be gained by comparing the results of the recrystallized samples with the cube sample (i.e. two samples with low dislocation content). In this case the best selection from this subset of samples is 98% cold worked-recrystallized sample with an increase in safety factor of 1.5 times over the worst selection (which is again the cube texture).

3.6.3 A Lamina Emergent Torsional Joint

In the first case study of the Laminar Emergent Torsional geometry (LET joint), it is subjected to 1.56N in-plane loading (Table 3.3). 1.56N is arbitrarilt selected to give a stress condition

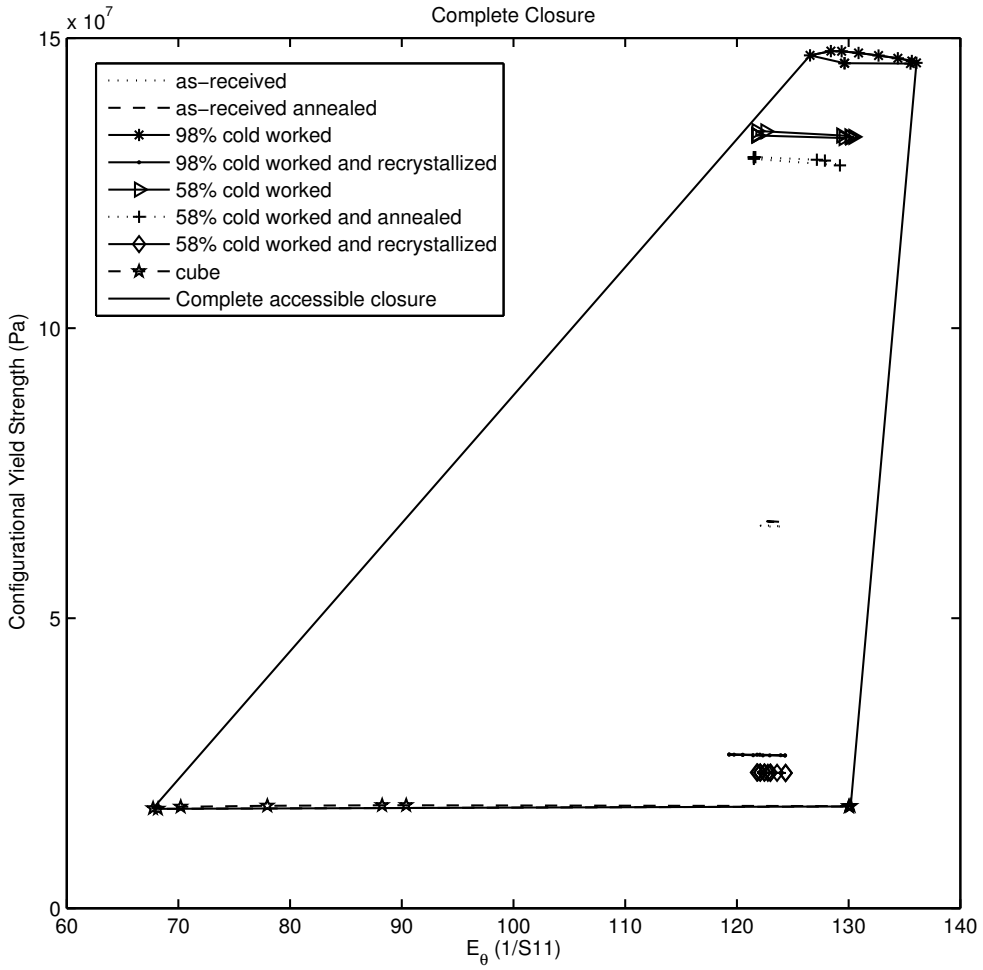

Figure 3.12: Configurational sub-closure of OFE copper samples for hole-in-plate geometry

in the vicinity of the elastic/plastic limit. The average safety factors (over all nodes) of each version of the assumed materials are plotted in Figure 3.14 and Figure 3.15 against the rotation angle of the rolling direction; recall that a safety factor below one indicates that the material has passed its yield point. The optimal performance is given by the cold worked samples which have safety factors between 4 and 5. The 98% cold worked sample gives the best performance ($\lambda = 4.83$) when the component global frame is aligned with the material rolling direction, for the homogeneous condition. For the heterogeneous case $\lambda = 4.65$ when the component frame is 7.5 degree from the rolling direction.

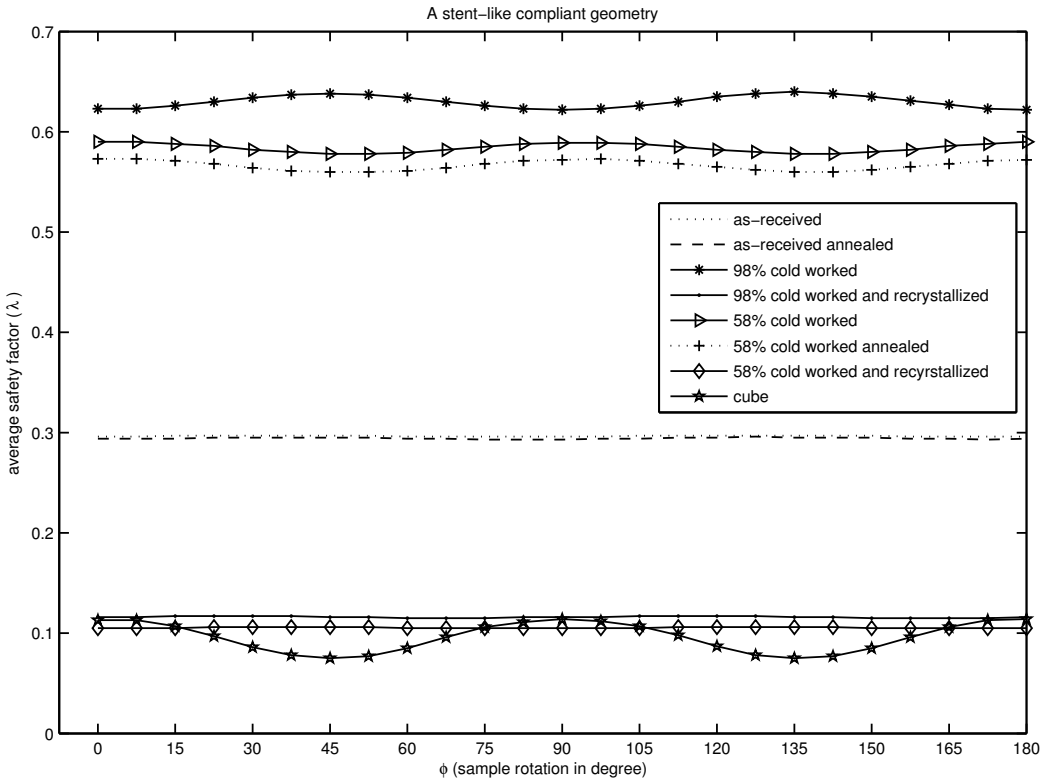

Figure 3.13: A stent-like compliant geometry and its average safety factors

Figure 3.16 and Figure 3.17 show the average safety factor for the homogeneous and heterogeneous components vs. material orientation when 1.56N out-of-plane load is applied to the geometry (Table 3.3). Again, the best performance is given by the 98% cold worked sample ($\lambda = 5.27$) when the component frame is aligned to the material rolling direction.

The directional dependent performance is observed to be inflated in highly textured samples such as cold worked and cube texture samples for both applied load conditions. In-plane loading with the homogeneous condition gives 1 to 4% difference in yield response for derivative materials prepared from as-received OFE copper, and around 30% difference in performance for the cube texture sample. The difference in performance is exaggerated in the heterogeneous condition: 1 to 5% difference in derivative materials and 60% difference in cube texture materials. Out-of-plane loading gives an even wider gap between the optimal and minimal performance. The variation in performance is around 1 to 5% in derivative materials and a little over 30% in cube texture sample

for the homogeneous case. The heterogenous case reads 2 to 7% difference in derivative materials and close to 80% difference in the cube texture sample.

The pattern of results shows that the homogeneous condition gives better average performance while the heterogeneous condition gives stronger directional dependent performance.

3.7 Chapter Summary

This chapter presents FEA-based microstructure sensitive design by incorporating the HBH model into standard FEA tools. The HBH model retains the distinctive corner stress states defined for FCC crystals by the classical Taylor Bishop-Hill model, but differs in focusing the choice of corner stress state upon the macroscopic applied stress. The HBH model uses safety factors to describe the distance of stress states on each node as calculated via FEA, from the material yield surface. The minimum safety factor is multiplied by the applied load to give a so-called configurational yield stress, which readily provides the information of the yield limit for a given geometry with specific material.

The FEA simulations with incorporated HBH model can easily be adapted to the mechanical design practice. The first example given in this chapter (hole-in-plate) demonstrates that highly textured samples such as 98% cold worked, 58% cold worked, cold worked-annealed, and cube texture samples show directional dependent performance; by rotating each sample along the sheet normal direction in ϕ , the performance of the plate can be optimized or minimized. The study also shows that the HBH incorporated FEA approach can show the location of high stress states in the geometry and predicts the most likely location of failure.

A stent-like geometry example also shows that highly textured samples show direction dependent performance. Although the improvement due to material rotation is small, the optimal choice (the combination of material selection and its orientation) can give as high as 8.5 times better performance when compared to the worst selection.

The last example demonstrates how the method can assist the decision of optimal material selection and orientation based on design purposes. For example, if a determining factor of design is yield strength, then the homogeneous condition gives better performance by providing the best combination of choices: the optimal material selection and its material rolling direction. However, if the directional dependent performance is of significant interest for the design (such

as in design for reverse engineering [37]), then a heterogeneous condition gives the ideal choice by providing the best combination of material and its orientation (material rolling direction). The optimal material, its material rolling direction and processing methods can be altered based on design purposes.

Configurational sub-closures can be used to identify regions of material property closures that are accessible to designers using the available materials and for arbitrary rotation of the global texture.

The work presented in this chapter demonstrates how combining information of material microstructure and part geometry can influence the design practice. The method delivers a practical approach to improve the performance of simple mechanical parts by incorporating material microstructure information into a stress-centric framework of HBH model through FEA.

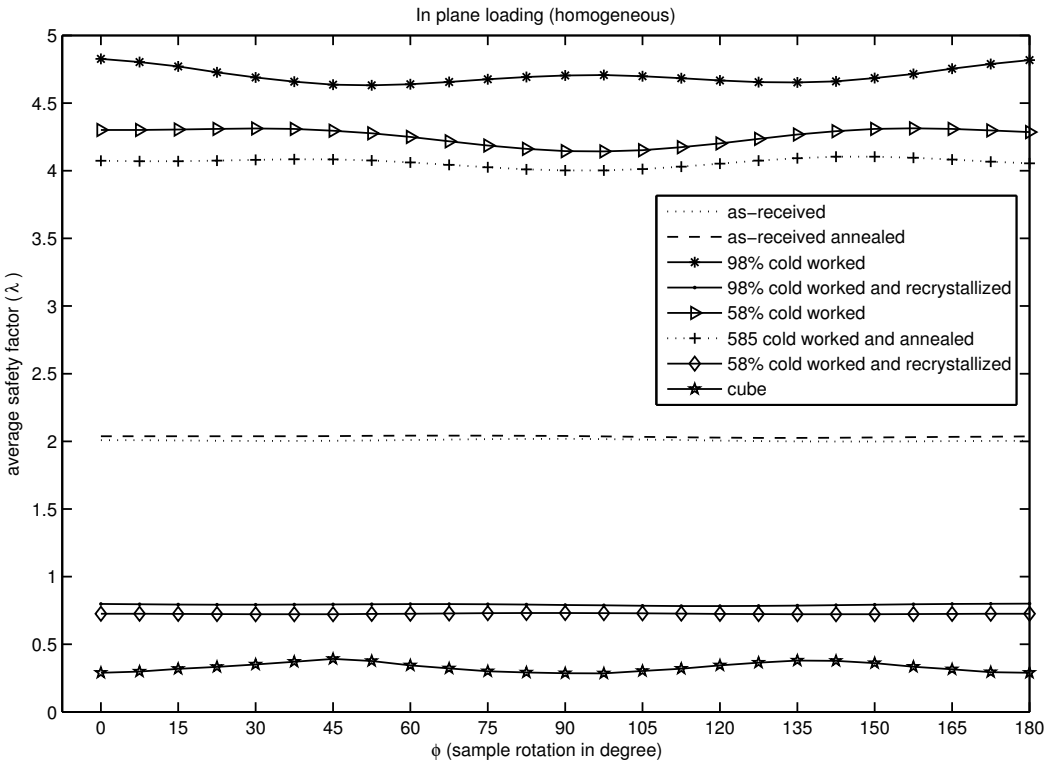

Figure 3.14: In-plane loading with homogeneous condition

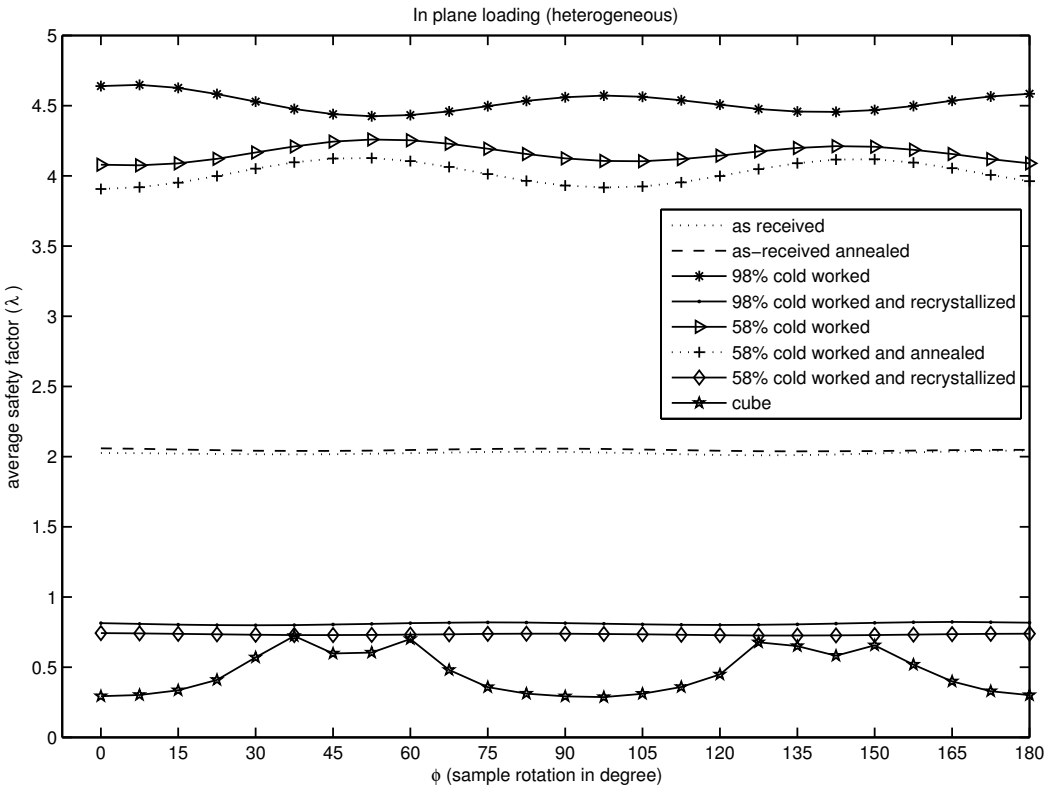

Figure 3.15: In-plane loading with heterogeneous condition

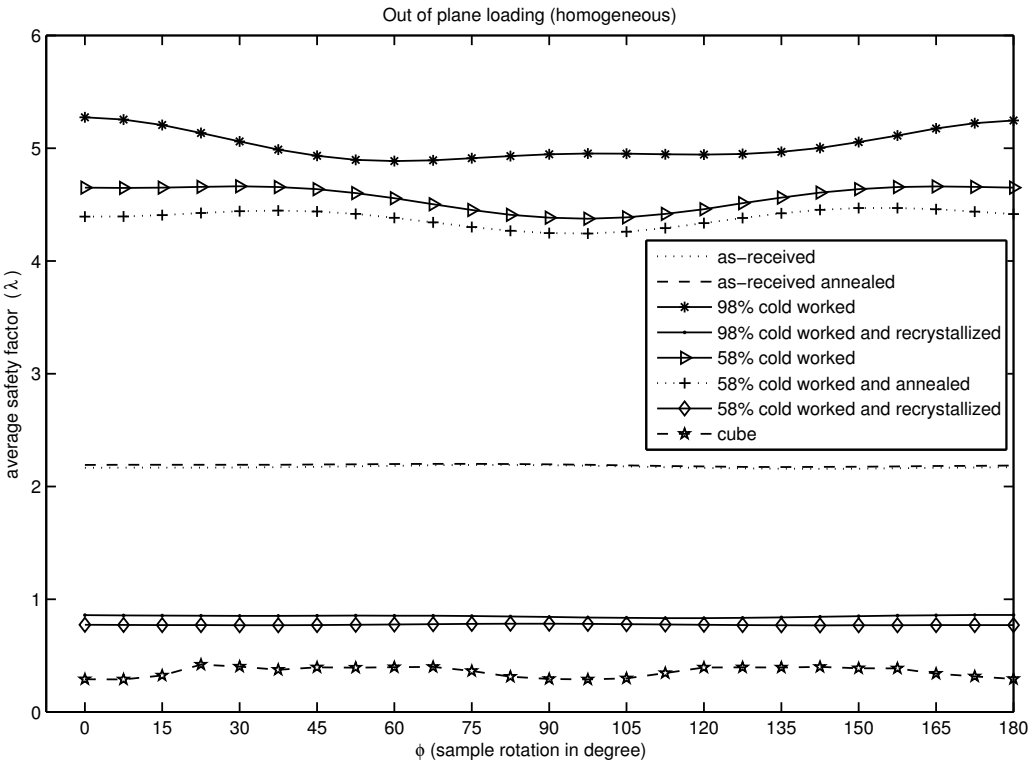

Figure 3.16: Out-of-plane loading with homogeneous condition

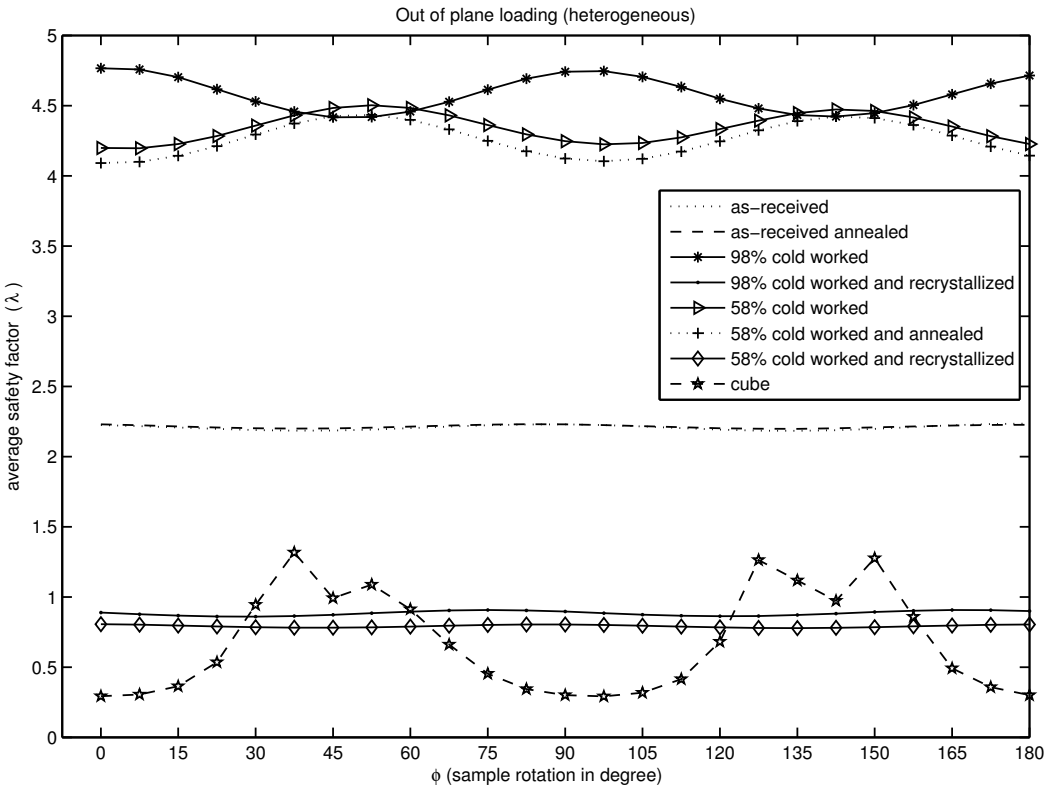

Figure 3.17: Out-of-plane loading with heterogeneous condition

CHAPTER 4. FOUR-PARAMETER HYBRID-BISHOP-HILL MODEL

4.1 Chapter Overview

There are several microstructure-based theories for prediction of yielding in polycrystalline materials. Many of the models are focused upon integrating crystallographic texture (the preferred distribution of lattice orientations) into yield predictions [29, 30, 38–42]. Although the existing microstructure-based models provide acceptable estimates of yield limit, improving these predictions with more sophisticated frameworks may leads to significantly enhanced design practices. One recent study suggested a way for potentially improving the prediction of yield surface by incorporating another physical parameter, in addition to the crystallographic orientations, into the model [43].

The study uses hexagonal materials to show how the prediction of yield strength improves immensely incorporating not only the crystallographic texture alone but also the grain size information. Fromm et al. approached the problem of yielding in α-titanium using the Taylor power-law-visco-plastic model, coupled with the Hall-Petch relation [43] for including information about grain size. Local measurements of the grain size were employed with the familiar evaluation of the Taylor factor as a function of lattice orientation to simultaneously consider the effects of lattice orientation and grain size on yielding. Their study indicates that the prediction of yield strength is improved relative to the Taylor visco-plastic model, by accounting for grain size variations distributed among the orientation components of the crystallographic texture.

Although the Hall-Petch relation used in the study of α-Titanium shows improved predictions for the yield surface, the Hall-Petch slope for copper is relatively small, as it is for all FCC materials, and hence grain size manipulation has limited impact on yielding of copper. Pure FCC materials strengthen mainly by means of dislocation-dislocation interactions [44, 45]. The empirical Taylor relation [35], also known as the Bailey-Hirsch equation, shows a strong relationship

between the shear stress required for dislocation slip, and the dislocation density present within the material.

$$\tau_{crss} = \alpha \mu b \sqrt{\rho} \tag{4.1}$$

In the equation, ρ is the total dislocation density, b is a Burgers vector, μ is the elastic shear modulus, and α is an empirical constant that typically varies from 0.2 to 0.5 [46]. Taylor flow stress is viewed as the stress that is required to induce the next increment of plastic deformation at a material point; thus, it is interpreted to be the current critical resolved shear stress of the material. In this work, we propose to employ an experimentally-determined estimate of geometrically necessary dislocation (GND) density as a fourth parameter associated with the prediction of yield strength in FCC copper.

The classical Taylor Bishop-Hill model [1, 2, 8] is one of the well known yield theories which focuses on plastic strain states to predict yield limits. There are some difficulties of using the classical models in evaluation of elastic/limited design because the elastic and plastic components of the total strain are comparable in magnitude and are generally difficult to separate. Thus the precise condition of plastic strain at initial yielding is not accurately specified. It follows that application of these classical microstructure-based theories of plasticity to initial yielding is a rather imperfect approximation at best. However, a stressed-based yield approach, the Hybrid-Bishop-Hill (HBH) model [10], works nicely in predicting local stress states and mechanical yielding in the near-vicinity of yield surface. This approach is closely related to the classical Bishop-Hill model [1, 2]. This chapter will demonstrate the improvement of yield limit prediction by using the HBH model coupled with four physical parameters: three crystal orientations plus the geometrically necessary dislocation density. The study uses database of rolled and heat-treated oxgen-free electronic copper shown in Table 4.1.

Table 4.1: Sample description

Sample Description	*Heat Treatment Temperature (Celsius)*	*Heat Treatment Time (Hour)*
98% cold worked	22	N/A
98% cold worked and recrystallized	225	0.5
58% cold worked	N/A	N/A
58% cold worked and recrystallized	225	1.5

4.2 Methodology

4.2.1 The Distribution of Local States

The term 'local states' refers to any local characteristics of material that affect the properties of interest. The 'local states distribution' refers to how the components of microstructures such as crystal orientations and dislocation densities are distributed across the set of possible local states.

Local material properties need to be linked via some relations to macro level effective properties of interest in the design problem. Theses microstructure-properties relations are homogenization relations that relates the microscopic details of the microstructure to effective properties at the macroscale. For the purposes of this study the homogenization relations of interest will require only volume fraction information of the local state distribution. Such information is often referred to as 'first-order' information on the microstructure.

The elastic and plastic (yielding) properties are the two main properties of interest in this work. Not all features and characteristics of microstructure are of equal importance to the elastic and yield properties of polycrystalline materials. Rigorous bounds on elastic properties require, at a minimum, information about the distribution, by volume fraction, of the components of microstructure by lattice phase and lattice orientation, and they are insensitive to dislocation density (at ordinary levels of density). On the other hand, plastic properties require the local dislocation density distribution in addition to the distribution of lattice phase and orientation.

One set of first-order bounding relations on the elastic properties are called the Hill-Paul bounds [11]; the simplified Hill-Paul upper- and lower-bounds on the elastic properties are shown in the following expressions where $\overline{S}_{ijkl}$, and $\overline{C}_{ijkl}$ denote the volume averaged elastic compliance

tensor and stiffness tensor:

$$\overline{S}_{ijij}^{-1} \leq C_{ijij}^{eff} \leq \overline{C}_{ijij}. \tag{4.2}$$

Because of the assumption made in the derivation of above bounding relation, the bounds hold only for the diagonal elements of the elastic stiffness tensor [11,12,20,21]. The derivation for bounding relations for off diagonal elements of the stiffness tensor requires a more sophisticated approach, based upon the positive definite property of the elastic tensor. Taking the arithmetic means of the upper bound and the lower bound is called the Hill average [14, 34]. The Hill average applies to both diagonal and non-diagonal components of the elastic properties:

$$C_{ijkl}^{eff(Hill)} \approx \frac{\overline{S}_{ijkl}^{-1} + \overline{C}_{ijkl}}{2}. \tag{4.3}$$

To define the distribution of local states within the material, it is first necessary to define the pertinent local state space. The lattice orientation (g) is conveniently specified by a set of three (Bunge) Euler angles, ϕ_1, Φ, and ϕ_2; these define a set of three rotations that are required to bring a sample-fixed coordinate frame into coincidence with the lattice-fixed frame [14]. The Euler angles are readily determined from the electron backscatter diffraction (EBSD) patterns acquired at material points sampled in spot mode using a scanning electron microscope (SEM) [15]. Each data point belongs to the complete (total) Bunge-Euler space (FZ_T) [14]:

$$FZ_T = \left\{ g = (\phi_1, \Phi, \phi_2) \left\| \begin{matrix} 0 \leq \phi_1 < 2\pi \\ 0 \leq \Phi \leq \pi \\ 0 \leq \phi_2 < 2\pi \end{matrix} \right. \right\}. \tag{4.4}$$

For copper, the space of Euler angles can be reduced because of lattice symmetry. The cubic crystal lattice possesses 24 rotational symmetries; thus a reduced subspace is available within FZ_T that includes only one of the 24 physically equivalent lattice orientations of the local crystal [11]. However, a reduced fundamental zone has a non-rectangular shape that is difficult to deal with for efficient binning and computational operation. It is convenient to use a 3-fold redundant subspace,

FZ_{3C}, which is rectangular [12]. The space spanned by FZ_{3C} is:

$$FZ_{3c} = \left\{ g = (\phi_1, \Phi, \phi_2) \left\| \begin{array}{l} 0 \leq \phi_1 < 2\pi \\ 0 \leq \Phi < \dfrac{\pi}{2} \\ 0 \leq \phi_2 < \dfrac{\pi}{2} \end{array} \right. \right\}. \tag{4.5}$$

The rectangular shape of FZ_{3C} facilitates an easy partitioning of the fundamental zone into cubical bins, which is discussed later.

Bunge-Euler space is useful to represent crystal orientations because of its naturally inherent periodicity. However, the volume of an infinitesimal region of Euler space must be scaled by the so-called invariant measure in order to arrive at the true volume in rotation space; i.e. the space is somewhat distorted.

$$dR = \frac{1}{8\pi^2} sin\Phi d\phi_1 d\phi_2 \tag{4.6}$$

The use of the invariant measure in scaling the volume of the space complicates the analysis for microstructure design, and loses the useful characteristics of periodicity in Euler space [20]. In this study, we ignore the small error associated with overlooking the invariant measure for the sake of simplicity, and use a rectangular space defined by the three Euler angles, allowing some distortion in orientation space similar to the approach published by Kalidindi et al. [20, 21].

The other local state variable used in this work is the geometrically necessary dislocation (GND) density, ρ. The local state space of GND density can be expressed as a line segment, since dislocation density adds only one scalar variable to the local state space. The symbol h is used to represent all four of the local state variables of interest: $h = (g, \rho)$. Thus $h \in FZ_{3C} \times \triangle$ where $\triangle = \{\rho \mid \rho_{min} \leq \rho \leq \rho_{max}\}$.

The convenient approach to partitioning this space utilizes uniform rectangular bins within FZ_{3C} for lattice orientation, and line segments of equal measure in GND density. Thus, the tessera associated with $FZ_{3C} \times \triangle$ are of 4-dimensional rectangular character. Euler angles and GND densities at the center of each 4-D bin are used to approximate the lattice orientation and GND density for each measurement point falling within that bin.

For crystal orientation space, the discretization is expressed using indicator function; ω_n represents the nth bin in FZ_{3C}, and the indicator function takes the value of 1 if $g \in \omega_n$, and 0 otherwise.

$$\chi_n(h) = \begin{cases} 1, & if\, g \in \omega_n \\ 0, & otherwise \end{cases} \tag{4.7}$$

In the case of GND density, the line segment of the local space is partitioned with κ_m where m represents the mth bin of discretized dislocation density space. The indicator function for dislocation density space is similar to the one for orientation space.

$$\eta_m(h) = \begin{cases} 1, & if\, \rho \in \kappa_m \\ 0, & otherwise \end{cases} \tag{4.8}$$

Although not required in this study, this approach of discretization is compatible with the use of Fast Fourier Transformation (FFT) method for computing average tensors [11, 12].

Suppose that the local state is determined at S points of a sample via EBSD, with the state at point s being h_s. Then the orientation distribution function for the sample can be defined via:

$$f^n = \frac{1}{S}\sum_{s=1}^{S} \chi_n(h_s) \tag{4.9}$$

and the sum over the local state distribution is unity: $\sum f^n = 1$.

The elastic nature of pure FCC material depends only upon crystal orientations; thus, the effective stiffness tensor ($\overline{C}_{ijkl}$) is obtained by weighting the local stiffness tensor (C^n_{ijkl}) by means of the orientation distribution. The local stiffness tensor is associated with the center of each orientation bin, and the weighting is done by taking the number fraction of the total measurement points associated with the assigned bin:

$$\overline{C}_{ijkl} \approx \sum_{n=1}^{N} f^n C^n_{ijkl}. \tag{4.10}$$

Because the plastic properties of FCC materials depend on both lattice orientations and GND density, the distribution function of interest requires the product of both orientation and GND local state spaces. By using the previously introduced indicator functions, the distribution

function is expressed as:

$$f^{nm} = \frac{1}{S}\sum_{s=1}^{S} \chi_n(h_s)\eta_m(h_s) \tag{4.11}$$

where S is the total number of measurements of local state, and n and m are associated with bins in each component of the local state space. The sum over the total local states gives unity: $\sum_n \sum_m f^{nm} = 1$.

The effective yield stress ($\overline{\sigma}_{ij}$) is obtained by weighting the local yield stress (σ_{ij}^{nm}) with the overall distribution function:

$$\overline{\sigma}_{ij} \approx \sum_{n}^{N}\sum_{m}^{M} f^{nm}\sigma_{ij}^{nm}. \tag{4.12}$$

Numerical examination of the bin-size dependency of calculations like Eq. 4.12 have determined that numerical errors are less than 1% when a bin size of $5^\circ \times 5^\circ \times 5^\circ$ in the three Euler angles in FZ_{3C} and 100 division in dislocation densities binning is selected; consequently, this bin size was utilized throughout this chapter unless otherwise specified.

4.2.2 Geometrically Necessary Dislocation (GND) Density

Dislocation density quantifies crystallographic defects, and based on a Taylor assumption, the plastic deformation in materials is almost entirely caused by dislocation slip [44]. Slip occurs when dislocations experience an increment of flow stress in excess of that shown in Eq. 4.1.

There are two different types of dislocations commonly referred to: the statistically stored dislocations (SSD) and geometrically necessary dislocations (GND). The former (SSD) have a net signed density of zero within the Burgers circuit due to the equal and opposite sign of dislocations. On the other hand, the GND densities do not cancels out within the Burgers circuit, and this dislocation density causes long range stress fields in materials [47].

The idea of the dislocation density tensor α_{ij} was first introduced by Nye [48], and further developed by Kroner [49]. Kroner added the effect of lattice strain into the dislocation density tensor α_{ik}:

$$\alpha_{ik} = \kappa_{ki} - \delta_{ki}\kappa_{pp} + \in_{klj} \varepsilon^{e}_{ij,l} \tag{4.13}$$

where κ is the lattice curvature, δ_{ki} is the Kronecker delta, $\in_{klj}$ is the permutation tensor, and $\varepsilon^{e}_{ij,l}$ represents the elastic strain gradients [48–51]. The lattice curvature κ can be obtained taking the

derivatives of the lattice rotation θ_k on the Burgers circuit, with respect to the neighboring scan points:

$$\kappa_{ki} = \frac{\partial \theta_k}{\partial x_i} \tag{4.14}$$

where x_i indicates a vector between the scan points [51]. When a surface is scanned using EBSD, the scan points are placed along two directions: x and y. Since the lattice curvature is defined by taking the derivatives of lattice rotations with respect to the direction of neighboring scan points, only six out of nine components of lattice curvature are defined; the curvature which requires the neighboring points in the z direction is not obtainable due to the lack of scan points.

If the elastic strain gradient term in Eq. 4.13 is negligible, five components of the dislocation density tensor are obtained from the available six components of lattice curvature. By the use of mathematical intuition, the difference of two other components of dislocation density tensor is also obtained [51]. The full dislocation density tensor is not obtainable because of these limitations; but the incompletely measured tensor can nevertheless be used in a particular way to estimate the overall GND density [52].

The dislocation tensor may also be expressed in terms of the distortion tensor β, also called the displacement gradient.

$$\beta_{ij} = \frac{\partial u_j}{\partial x_i} \tag{4.15}$$

The distortion tensor takes the spatial derivatives x_i of displacement field u_j. The total distortion β^T is the addition of plastic and elastic components: $\beta^T = \beta^P + \beta$ where β is the elastic distortion. The field must be continuous and differentiable within the body; thus the condition $\nabla \times \beta^T = \nabla \times (\nabla \cdot u) = 0$ is applied [49, 53–55]. This gives $\nabla \times \beta^T = -\nabla \times \beta$. The dislocation density tensor can then be simply expressed by taking the curl of the distortion tensor β.

$$\alpha = \nabla \times \beta \tag{4.16}$$

The above relation is called the fundamental equation of continuum dislocation theory [54,55]. The equation suggests that the presence of dislocation densities creates geometrical distortion within materials; thus, it conveys the information of GND densities. In this regard, the terms “dislocation densities” and “GND densities” are used in the same context in this work and used alternately.

The potential difference between the measured GND content and the overall dislocation density is discussed later in the chapter (in section 4.4).

The recent development of high-resolution EBSD (HREBSD) analysis enables the measurement of the complete distortion tensor components by comparing the shift of Kikuchi band in EBSD patterns in neighboring scan points [52,54–57]. Various approaches have been developed to obtain the elastic distortions and strain of material based upon this idea [50, 52, 53, 55, 56, 58, 59]. This study uses an extension of these method which provides accurate local displacement gradient to express Nye dislocation density tensor [54], and suites the calculation of GND densities. In this work a full nine component average of the dislocation density tensor is used as an estimate of the overall dislocation density used within the Bailey-Hirsch relation (Eq. 4.1).

The Nye dislocation density tensor expresses the GND densities within the single Burgers circuit [60]. The HREBSD method uses two neighboring scan points to create an imaginary Burgers circuit; thus to have an accurate estimate of GND measurement requires careful consideration of scan step size. Increasing step size leads to the loss of dislocation network information; on the other hand, reducing the step size amplifies noises in the dislocation density data [60].

Kysar et al. suggest a meaningful scan step size L for estimating GND densities with HREBSD analysis:

$$\frac{1}{\sqrt{\rho_{grid}^{total}}} \ll L \ll \frac{1}{\sqrt{\rho_{grid}^{total} b}} \tag{4.17}$$

where ρ_{grid}^{total} is the total GND density and b is the Burgers vector [47]. The relation (Eq. 4.17) indicates that the relevant step size needs to be located between a maximum limit, significantly larger than the average distance between dislocations, and a minimum limit, significantly smaller than that relating to notable variations in the plastic deformation field [47]. With this notion in mind, the step size of each OFE copper sample's scan is decided and it is shown in Table 4.2.

4.2.3 The Hybrid Bishop-Hill (HBH) Model

The Hybrid Bishop-Hill (HBH) model is a modified version of the Taylor-Bishop-Hill (TBH) model. In the TBH model, the yield locus is defined in a five dimensional deviatoric stress space, and each stress state is expressed in term of a critical resolved shear stress. The TBH model predicts the existence of a convex polyhedron shaped yield surface, which has 56 vertices [1] for

Table 4.2: HREBSD scan step size

Samples	*HREBSD scan step size (μm)*
98% cold worked	1
98% cold worked and recrystallized	1
58% cold worked	1
58% cold worked and recrystallized	2.5

FCC materials. The TBH model states that for FCC materials a set of 56 stress states (also kwon as stress corners) is capable of activating the required combinations of slip for an arbitrary plastic deformation. This is a strain-based model: each grain experiences the uniform imposed (macroscopic) strain and the active corner stress state is the one that maximizes the plastic work done.

The HBH model, on the other hand, is a stress-based model and uses the same stress corners defined by the TBH model to predict the yield strength of polycrystalline materials. The model reflects the natural heterogeneity of the constituents of the polycrystal. The magnitude of the corner stress states requires knowledge of a critical resolved shear stress τ_{crss}. This stress defines the level of shear stress that must be present upon any of $\{111\}\langle 110\rangle$ slip systems to cause dislocation slip to occur. It is known that τ_{crss} is proportional to the square root of the local total dislocation density as in Eq. 4.1 which typically varies with position x.

Some of the advantages of using the HBH model are that it focuses on the applied stress rather than on the plastic strain; this makes the model much more accessible to design engineers who typically focus more upon stress states, rather than strain states. Furthermore, the HBH model works superior to the TBH model at near-vicinity of yield surface due to reasons discussed earlier (in Section 4.1).

The HBH model makes a simple assumption that the local yielding at any position in the material occurs at that corner stress states, $\hat{\sigma}_{ij}^{C}$, that lies "closest" to the macroscopic stress, $\hat{\sigma}_{ij}$. The "hat" over the stress symbol signifies the deviatoric stress. The distance between these two stress states is defined by d_{ij}, where

$$d_{ij} = \hat{\sigma}_{ij}^{c} - \hat{\sigma}_{ij}. \tag{4.18}$$

The magnitude of distance between stress states, d, is defined by the Euclidean norm:

$$||d^2|| = d_{ij}d_{ij}. \tag{4.19}$$

Importantly, the distance defined according to Eq. 4.18 and Eq. 4.19 is invariant with respect to coordinate transformation. The selection of stress corner for any particular component (scan point) within the polycrystal is taken to be the Bishop-Hill corner stress that minimizes the distance d between the applied stress and the corner stress state.

The estimated (deviatoric) yield strength of the material is obtained by averaging over the texture and GND densities components in the sample using the expression

$$\hat{\sigma}_{ij}^{Y} \approx \sum_{n}^{N}\sum_{m}^{M} f^{nm}\sigma_{ij}^{nm} \tag{4.20}$$

where σ_{ij}^{nm} denotes the pertinent stress corner associated with bin nm in local state space. Note that all corner stress states exercised in Eq. 4.20 must be expressed in the macroscopic (sample) frame in order to interpret $\hat{\sigma}_{ij}^{Y}$ as the yield strength. Where yield strength is customary described as the full Cauchy stress, the deviatoric yield stress must be converted using the customary definition:

$$\sigma_{ij}^{Y} = \hat{\sigma}_{ij}^{Y} + \frac{1}{3}\delta_{ij}\sigma_{kk}^{Y} \quad \text{(summation over k implied).} \tag{4.21}$$

Exercising Eq. 4.21 to obtain σ_{ij}^{Y} requires additional physical information about the applicable pressure $\frac{1}{3}\delta_{ij}\sigma_{kk}^{Y}$ or some other characteristic of the normal components of σ_{ij}^{Y}. If, for example, the calculations involve estimates of a uniaxial tensile test, then only one component of σ_{ij}^{Y} is expected to be non-zero; and in this case a pressure term $\frac{1}{3}\delta_{ij}\sigma_{kk}^{Y}$ can be applied that renders σ_{ij}^{Y} as close as possible to a uniaxial stress condition. This is the approach taken in this chapter.

The dislocation density scales the magnitude of each corner stress in HBH model (or TBH model) via the critical shear stress in Eq. 4.1; thus, the magnitude of active corner stress varies based on the amplitude of dislocation density level. Three different HBH approaches are exercised in this study to observe the influence of dislocation densities on yielding. The first approach is the full four-parameter approach given in Eq. 4.20. This approach fully considers the effect of both the crystal orientation and the dislocation densities influence on yielding. The second approach

is to use the average dislocation densities in designated crystal orientation bins to scale the active corner stress in the HBH model. The active corner in each orientation bin, $\hat{\sigma}^C(n)$, is independently scaled (via Eq. 4.1) based on the dislocation density average associated with the particular crystal orientation, and Eq. 4.22 is applied to obtain the sample yield stress:

$$\hat{\sigma}^Y_{ij} \approx \sum_{n=1}^{N} f^n \hat{\sigma}^C_{ij}. \tag{4.22}$$

The third approach uses the overall average of dislocation densities of the sample to scale the active corner stress: i.e. each $\hat{\sigma}^C(n)$ is scaled by the same value. Then, Eq.4.22 is employed to obtain the yield limit of the sample.

4.3 Yield Surfaces of FCC Metal Texture

FCC metals possess unique textures. Some of the well-known FCC crystal textures and corresponding dominant crystal orientations are shown in Table 4.3.

Table 4.3: Common FCC metal texture

Texture Components	$\{hkl\}$	$<uvw>$	ϕ_1	Φ	ϕ_2
Copper, C	$\{112\}$	$<111>$	90	35	45
S	$\{123\}$	$<634>$	59	37	63
Goss, G	$\{001\}$	$<100>$	0	45	90
Brass, B	$\{001\}$	$<211>$	35	45	90
Cube	$\{001\}$	$<110>$	0	0	0

The yield surfaces for the above FCC crystal textures were determined using TBH corner stresses. The corner stress states in crystal frames are scaled by unity (i.e. dislocation density is ignored; $\tau_{crss} = 1$), and are transformed to the sample frame using FCC texture crystal orientations. The yield surface obtained this way show only the crystal orientation dependence.

Table 4.4 shows the volume of yield surface in each texture. The cube texture has the largest yield surface envelope volume; indicating the material will not easily yield, compared to the other

textured samples. The same observation suggests that a material having dominantly copper texture will fail the earliest for a random applied stress state.

The yield surface of brass texture and cube texture are shown in Figure 4.1 and Figure 4.2. The shapes of the yield surfaces are markedly different, based upon the different textures. These observations highlight the fact that crystal orientation strongly influences the shape of a given yield surface.

However, the critical shear stress in each corner stress states is a function of the local dislocation density. As a result, the accurate calculation of yield limit requires the consideration of dislocation densities.

The relationship between the critical shear stress and the dislocation density is given by a square root (Eq. 4.1). Thus, the higher the value of dislocation density, the larger the magnitude of corner stress, contributing to a larger yield surface. The volume of yield surface is thus a function of both the crystal orientations and the dislocation density.

Let us assume a hypothetical FCC material which has a mixture of two textures: 50% cube texture and 50% brass texture. First, consider a case when the effect of crystal orientation alone is considered. When the sample experiences pure shear (Sy_{12}), the cube texture withstands the stress up to a normalized value of 2.3, and brass texture is elastic up to 1.9 (Figure 4.1 and Figure 4.2). In this condition, the failure is dominated by the brass texture because it has the smaller yield limit.

Now, take the effect of dislocation density into consideration in addition to the texture of samples. Suppose that the cube texture grains have dislocation densities of 1e15 m^{-2}, and brass texture crystals have dislocation densities of 5e14 m^{-2}. The smaller dislocation densities in brass

Table 4.4: The yield surface envelope volume of well-known FCC texture: the τ_{crss} is normalized to unity

Texture Components	*Volume of Yield Envelope*
Copper, C	26.720
S	31.383
Goss, G	27.713
Brass, B	27.713
Cube	34.293

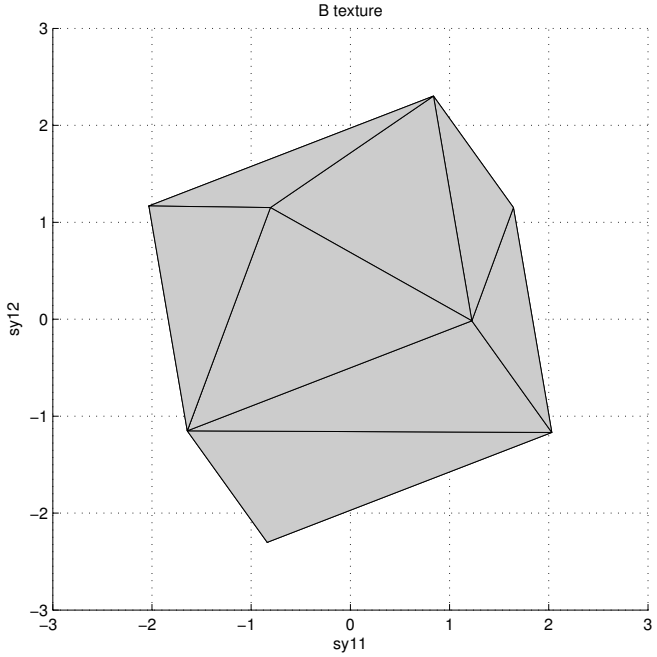

Figure 4.1: Yield surface for brass (B) texture

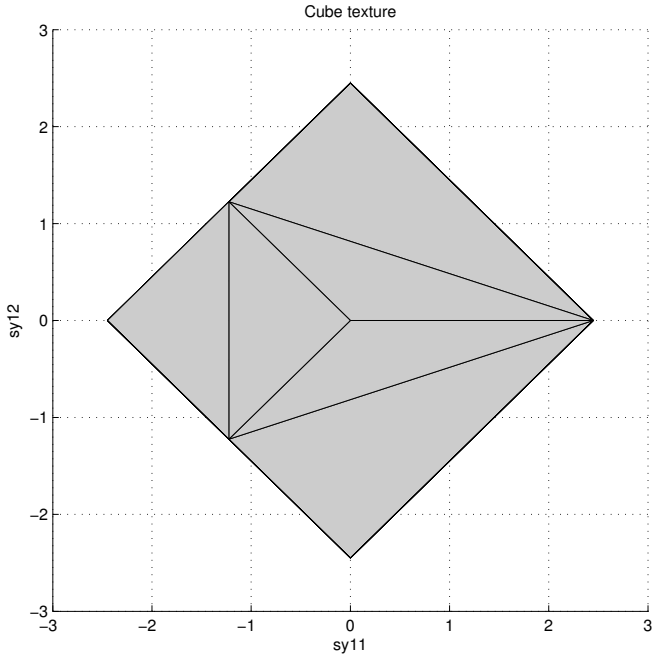

Figure 4.2: Yield surface for cube texture

texture aggravate the performance by making the yield surface smaller; consequently, the failure of the sample is influenced even more strongly by the brass texture.

What would be the case if the sample has an opposite dislocation density profile: the cube texture having the dislocation density of 5e14 m^{-2} and the brass texture having the dislocation density of 1e15 m^{-2}? The cube texture which has a larger yield surface volume, is scaled negatively by the smaller dislocation density; the brass texture having smaller volume is scaled positively by the larger dislocation density. Hence, the lower dislocation density in cube texture reduces its performance, and higher dislocation density in brass texture improves its performance. The overall performance of the sample comes by the competing effect from both the textures. Incorporating the dislocation density information in addition to the texture of samples enables the sensitive evaluation of yield limit.

This type of analysis would be particularly important if local effects dominated the component response, such as in micro-devices. We do not look in detail at such local response in this work.

4.4 Results and Discussions

HREBSD data sets comprising of $\sim$ 2000 grains were used for the evaluation of sample yield limit of the various copper types investigated in this chapter. The estimated dislocation densities and measured (via HREBSD) GND levels of four samples (98% cold worked sample, 58% cold worked sample, 98% cold worked-recrystallized sample, and 58% cold worked-recrystallized sample) are shown in Table 4.5. The estimated dislocation density values are obtained from experimental tensile strength data and the samples averaged Taylor factor (M), through the Taylor relationship ($\tau_{crss} = \frac{\sigma_y}{M}$) and Eq. 4.1. We note that the GND content is typically only a fraction of the total dislocation content (for example, [61] estimates about 35% of total dislocation content for one sample). In this work, we are assuming that the ratio of GND to total dislocation content is effectively constant for the different textures / samples. The accuracy of this assumption has not yet been widely studied, and more work in this area is required in the future.

Observation Table 4.5 suggests that the HREBSD method gives similar trends for dislocation density level compared to the estimated values (estimated from the measured yield points). In

both cases the cold worked samples show significantly higher dislocation density, compared with the recrystallized samples.

Table 4.5: Sample dislocation densities (GND densities)

	Estimated Dislocation Density (Eq. 4.1)	*HREBSD measurement of GND*
98% cold worked	$\sim$ 1e15	7.77e14
98% cold worked and recrystallized	$\sim$ 3.2e13	9.89e13
58% cold worked	$\sim$ 8.6e14	3.96e14
58% cold worked and recrystallized	$\sim$ 2.6e13	3.91e13

Table 4.6: The HBH tensile yield strength

	four-parameter approach yield strength (MPa)	*Orientation bin average GND yield strength (MPa)*	*Sample average GND yield strength (MPa)*
98% cold worked	303.12	314.44	315.54
98% cold worked and recrystallized	109.11	113.51	113.73
58% cold worked	216.61	222.54	223.78
58% cold worked and recrystallized	72.430	74.512	74.612

The uniaxial yield strength estimated by the HBH model is presented in Table 4.6. The results show that the four-parameter approach consistently gives lower yield strength compared to the orientation averaged GND density method and sample average GND density cases. The differences in estimate of yield strength between the four-parameter approach and sample average GND densities yield strength is around 3 to 4%.

The four-parameter approach fully incorporates any correlations between GND content and crystal orientation; thus, it is expected to be the most accurate yield surface calculation method. The method incorporates the effect of the GND measurement at each material point, taking the square root of dislocation density at each point to determine the local critical shear stress.

The binning average method is less accurate compare to four-parameter approach due to taking an average value in each dislocation density bin rather than each material point. When

calculating τ_{crss}, taking the square root of the average density in a bin always gives a slightly higher value than taking the average of square roots for each material point. Although the bin average approach loses some information of GND density as it applies to active corners, the method might be more efficient in certain computation approaches. Calculating yield limit with smaller orientation bin size may alleviate the problem of losing GND information, but smaller binning requires more computational power.

The sample average GND method calculates the yield surface from information of crystal orientation alone, and then scales the surface based upon the overall average GND density. Thus, this method completely ignores any correlations between crystal orientation and GND density that may exist.

If the shape of the yield surfaces for the four-parameter approach and the sample average approach were identical, then this would suggest that either crystal orientation has a negligible effect on yield surface shape, or that there is negligible correlation between GND density and crystal orientation.

Figures 4.1 and 4.2 indicate that for the Cu material the yield surface shape depends strongly upon crystal orientation/texture. Hence any correlations between GND density and crystal structure should result in differences in yield surface shape for the two calculations methods.

Figure 4.3 illustrates the distribution in GND densities for the various crystal orientations in Euler space for the 98% cold worked sample, which displays the greatest correlation between GND and orientation. The gray scales on the maps display the level of GND densities. It is clearly seen that there is significant variation in dislocation density distribution based on crystal orientation for this particular sample.

The variation in GND densities with respect to different crystallographic texture components is shown in Figure 4.4. S texture component show significantly smaller dislocation densities than other texture components such as copper, goss, and brass texture.

Figure 4.5 shows the yield surface of S texture and goss texture based upon their corresponding dislocation densities. Goss texture performs better in tensile direction (Sy_{11}) of applied stress, and S texture performs about the same in both tensile (Sy_{11}) and shear direction (Sy_{12}). The average dislocation density for 98% cold worked sample is 7.8e14m^{-2}. As seen in Figure 4.4 the dislocation density for goss texture is close to the average GND value of the sample. This suggests

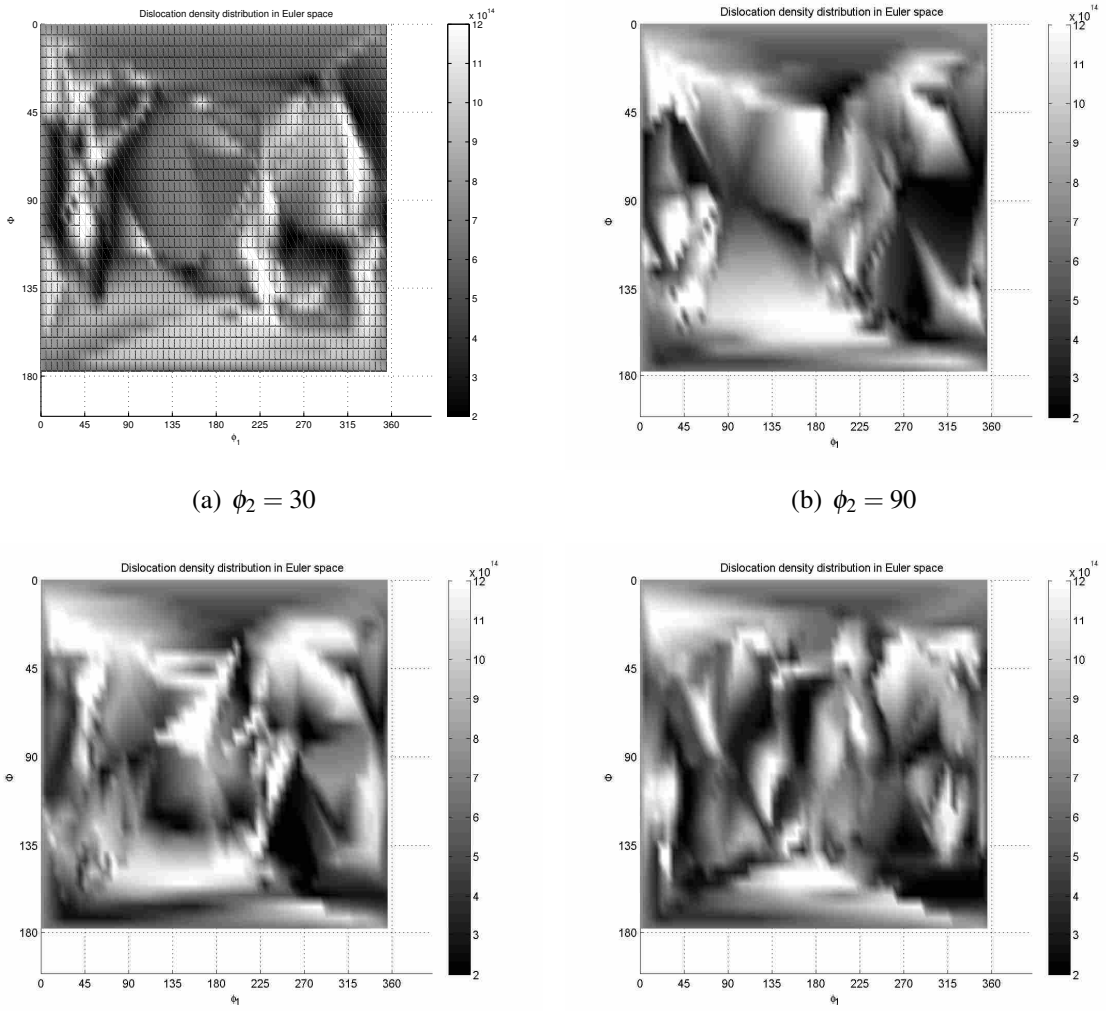

(a) $\phi_2 = 30$

(b) $\phi_2 = 90$

(c) $\phi_2 = 120$

(d) $\phi_2 = 180$

Figure 4.3: GND densities maps in ϕ_2 slice of crystal orientation

that the average dislocation density method works well enough for the estimate of elastic/yield limit in goss texture dominant sample. However, the average dislocation density approach will work very poorly on S texture; the next example will demonstrate this.

Let us assume that grains with goss texture and S texture experience a particular stress state: tensile load in Sy_{11}. S texture has a larger yield surface volume than goss texture (Table 4.4), but its performance in the Sy_{11} is slightly lower (about 17%) than the goss texture if only crystal orientation alone is considered. If the overall average GND density is used for the estimate of the yield surface (i.e. the four parameter approach is not used), for the S texture, the expected

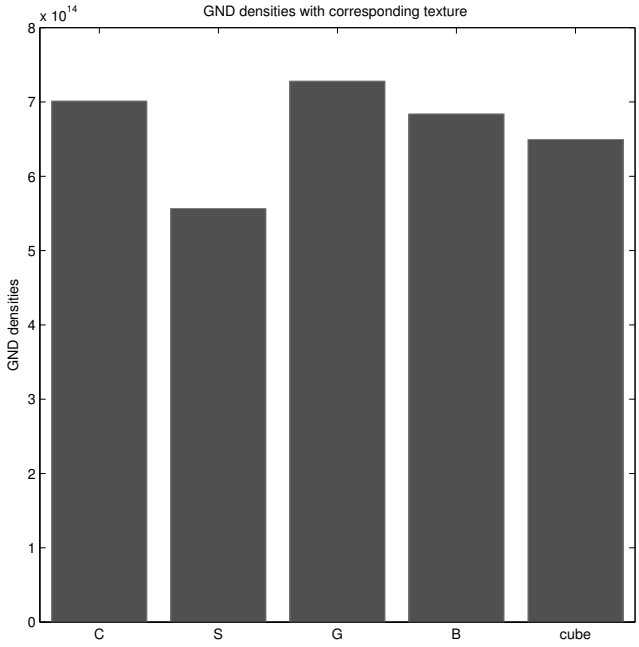

Figure 4.4: GND densities and corresponding texture: 1. C texture, 2. S texture, 3. G texture, 4. B texture, and 5. cube

yield limit in Sy_{11} will be slightly lower (about 17% lower) than the goss texture's limit. In reality, S texture is associated with much lower GND densities than goss texture (Figure 4.4), and its performance in the Sy_{11} lowers based on GND densities. When GND information is incorporated, the performance in Sy_{11} of S texture becomes lower, and the performance of goss texture becomes even higher (Figure 4.5), making a larger difference in performance between the two textures. This demonstrates that average dislocation density method can miss the crucial information for estimating the elastic/plastic limit.

The comparison of yield surface between four-parameter method and sample average GND densities approach is shown by using 98% cold worked sample (Figure 4.6 and Figure 4.7: yield closures are obtained using 9 degree crystal orientation binning with 100 GND densities binning). The shape of yield surface may looks similar in both methods as it is postulated since the crystal orientations used in the computation are the same. However, there are subtle differences relating to the fact that there is some correlation between orientation and GND densities as discussed previously. Some examples of this occur in the right hand side (label B) and the top left side (label

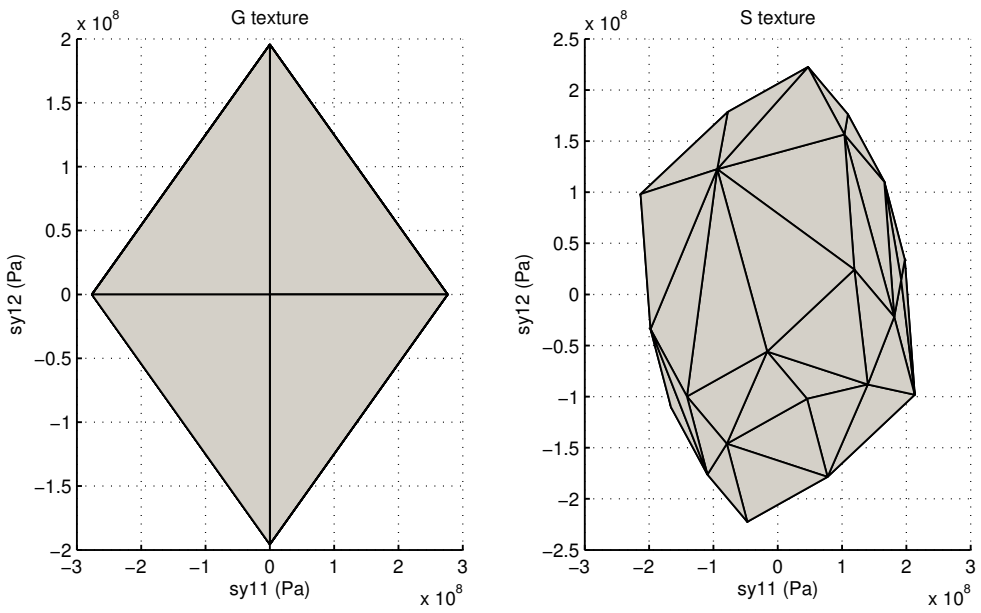

Figure 4.5: Yield surface for G texture and S texture with corresponding dislocation density

A) of the surfaces, as seen in the images; the different triangulation of the surfaces for the two images indicates a slight shape change in the areas for the two yield surfaces. The size of envelope is different (Table 4.7) because the magnitude of GND densities information is incorporated differently. The yield surface of average GND approach evaluates 11% larger envelope than the four-parameter method.

Although the variation may look small, the 11% difference in estimate of yield surface can possibly cause problems in the practice of mechanical design if a design of the part requires precise functionality.

The yield surface for two samples, 98% cold worked and 98% cold worked - recrystallized sample, are shown for a comparison. Figure 4.8 and Figure 4.9 show the yield surface obtained from four-parameter approach. Each of the samples has different texture; thus, the shape of yield surface is different. In addition to the shape, the magnitudes of GND densities are significantly

Table 4.7: Yield surface envelope volume of 98% cold worked sample

	Volume of yield surface envelope
Four-parameter approach HBH method	1.7595e23
Averaged GND HBH method	1.9846e23

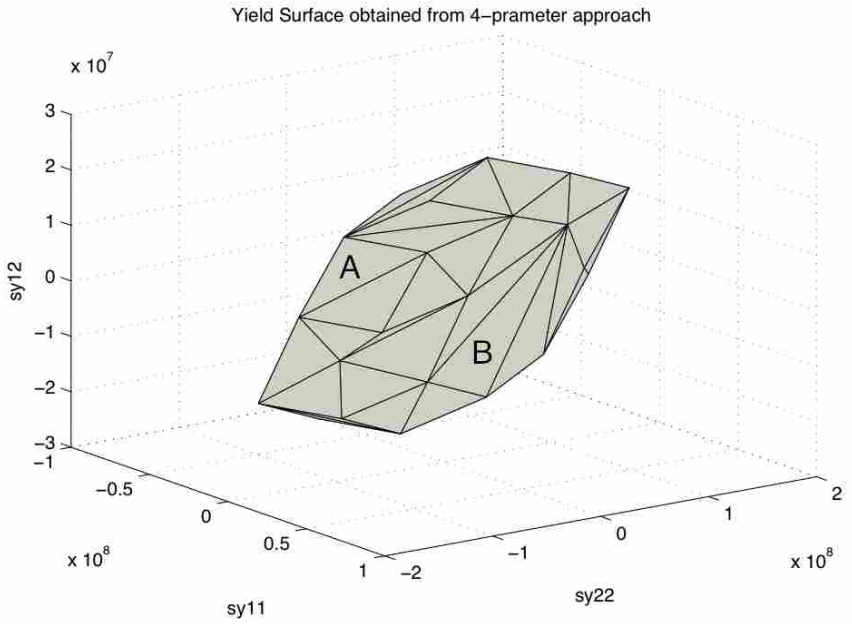

Figure 4.6: Yield surface of 98% cold worked sample using four-parameter HBH model shown in deviatoric stress space

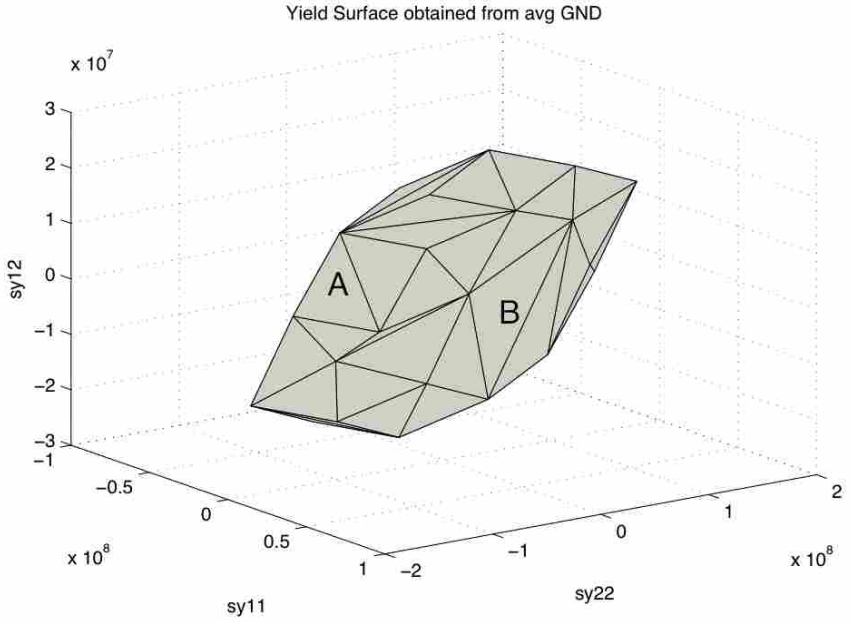

Figure 4.7: Yield surface of 98% cold worked sample using average GND densities HBH model shown in deviatoric stress space

lower in recrystallized sample, making the volume of closure much smaller compare to the cold worked sample.

The shape and volume of envelope suggest interesting outcome for some design feature. A larger closure of cold worked sample suggests that the sample is suited for a design, which simply requires a stronger material. However, if a design property requires material, which function only superior in one direction - to a tensile load, but not shear - the recrystallized sample performs effectively.

4.5 Chapter Summary

This chapter presents a new approach to the evaluation of yield limit by incorporating GND densities as a fourth parameter in addition to crystal orientation in a stress based Hybrid Bishop-Hill model. The HBH model retains the distinctive corner stress states defined for FCC crystals by the classical Taylor-Bishop-Hill model, but differs in focusing the choice of corner stress state upon the macroscopic applied stress. The use of GND densities properly scales the active corner stress states in the HBH model, allowing a better estimate of yield limit.

The yield characteristics are determined by the dominant texture and corresponding GND densities in each sample. The crystal orientation most influences the shape of the yield surface; the dislocation is known to affect the volume of the yield surface via Eq.4.1, but if correlations exist between orientation and dislocation content, then the shape of the yield surface is also changed. These correlations are captured by the four-parameter approach.

Three different methods were used to incorporate GND content into the HBH model: i) the full four-parameter approach (fully accounting for different GND contents at each point of a sample), ii) averaging the GND content in each crystal orientation bin, and iii) using only the overall average GND content. The change in yield surface shape does not alter dramatically between the different approaches, indicating that correlations between GND content and orientation are not strong. However, the example of the 98% cold worked copper demonstrated that there can be significant correlations between orientation and GND density that change the shape of the yield surface, and may be important factors in the analysis of elasto-plastic design. The four-parameter approach possibly improves the evaluation of yield limit in FCC materials, and hence contributes to the enhancement of mechanical design practice.

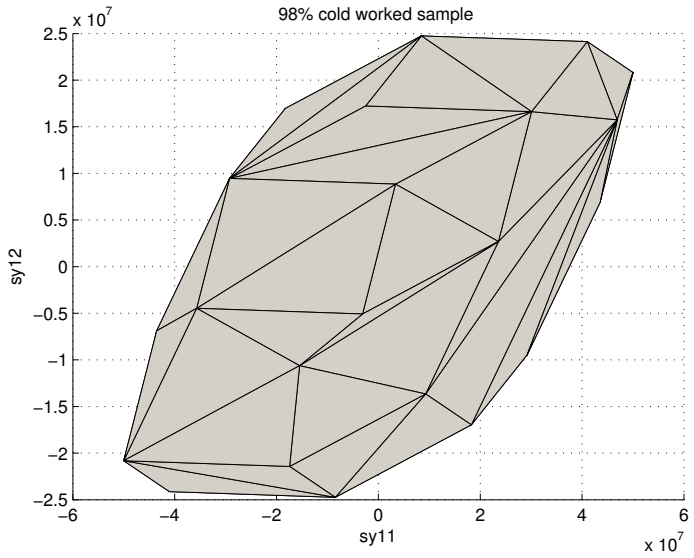

Figure 4.8: Yield surface for 98% cold worked sample obtained from four-parameter approach in deviatoric stress space

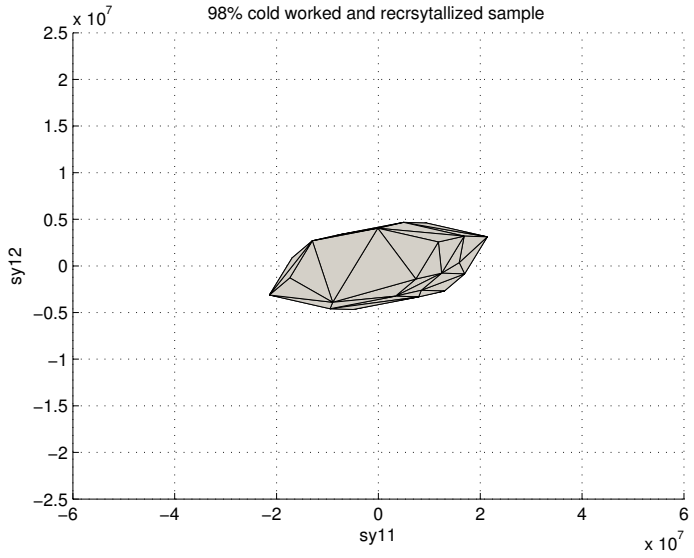

Figure 4.9: Yield surface for 98% cold work-recrystallized sample obtained from four-parameter approach in deivatoric stress space

CHAPTER 5. CONCLUSION

This dissertation presented a new approach for improving the performance of simple mechanical parts by incorporating material microstructure information into a stress-centric framework. Since the stress is much more accessible than the plastic strain, near the yield point of the material, the new method facilitates a much easier approach to yield limited design. This Hybrid Bishop-Hill model is appreciable to yield limit evaluation on FCC materials, and the study indicates that the HBH model gives better estimate of yield prediction than a classical Taylor-Bishop-Hill model.

A simple design problem is simulated with analytical method using the HBH model in chapter 2, and the same geometry is further studied in following chapter by FEA incorporated HBH model. The result reveals that FEA incorporated HBH model gives more accurate prediction than analytical model by utilizing a full 21 components of stiffness tensor.

The idea of safety factors is introduced: a safety factor scales elastic/plastic yield limit of each material to its yield surface. The FEA incorporated HBH model demonstrates that the HBH approach can be easily applied to various geometries and various stress states in mechanical design practice.

Although it is not presented in the work, there is an alternative use of safety factors: percentage of nodes failure within the geometry of interest with given applied load condition. The idea can be considered as practical yielding; this idea gives more freedom to mechanical designers to take control on what is suitable definition of yielding (a decision of how much percent node failure is considered as yielding) in particular design of interest. This approach can be applied to FEA incorporated HBH model in future to demonstrate easier design practice.

The examples of simple design practices with the HBH model in chapter 2 and chapter 3 exhibit that incorporating microstructure information opens up a new design space which are not seen with ordinary design practice.

The chapter 4 explores the possibility of improvements in the HBH model by introducing additional physical parameter. The stress corner in HBH model is defined by the critical shear stress as with the classical TBH model; thus, the detail information on critical shear stress can correctly scale the magnitude of active corner; hence improves the accuracy of the HBH model. The geometrically necessary dislocation density is introduced. The GND densities obtained from EBSD simulations method determines the critical shear stress of each sample. By utilizing the information on GND densities through four-parameter approach HBH model, a prediction on yield surface envelope volume of sample is modified by 11% in this study. This is due to the fact that GND densities have small but certain dependence on crystal orientations. The shape of the yield surface is most specified through the texture of the material, while the volume of the envelope is scaled in accordance with the GND density. The yield surface of material is defined by interactive influence on both the crystal orientations and GND densities. The four-parameter approach has potential for improving estimates of elastic-yield limit in all polycrystalline FCC materials.

The determination of dislocation densities through EBSD method is a currently developing technique. The advancement of this procedure will help the GND estimate of each material, and lead to the improvement of HBH models.

REFERENCES

[1] Bishop, J. F. W., and Hill, R., 1951. "A Theoretical Derivation of the Plastic Properties of a Polycrystalline Face-Centered Metal." *Philosophical Magazine,* **42**, pp. 1298–1307. 1, 4, 10, 27, 28, 40, 60, 67

[2] Bishop, J. F. W., and Hill, R., 1951. "A Theory of the Plastic Distortion of a Polycrystalline Aggregate under Combined Stresses." *Philosophical Magazine,* **42**, pp. 414–427. 1, 4, 10, 27, 28, 60

[3] Ashby, M. F., 2005. *Materials Selection in Mechanical Design*., 3 ed. Butterworth-Heinemann, San Francisco. 3

[4] Juvinall, R. C., 1967. *Engineering Considerations of Stress, Strain, and Strength*. McGraw-Hill, New York. 3

[5] Canova, G. R., Kocks, U. F., Tome, C. N., and Jonas, J. J., 1985. "The Yield Surface of Textured Polycrystals." *Journal of the Mechanics and Physics of Solids,* **33**(4), pp. 371–397. 3

[6] Lequeu, P., Gilormini, P., Montheillet, F., Bacroix, B., and Jonas, J. J., 1987. "Yield Surfaces for Textured Polycrystals - II. Analytical Approach." *Acta Metallurgica,* **35**(5), pp. 1159–1174. 3

[7] Hill, R., 1948. "A Theory of the Yielding and Plastic Flow of Anisotropic Metals." *Proceedings of the Royal Society A: Mathematical, Physical and Engineering Sciences,* **193**(1033), May, pp. 281–297. 3

[8] Taylor, G. I., 1938. "Plastic Strain in Metals." *Journal of the Institute of Metals,* **62**, pp. 307–324. 3, 4, 9, 27, 60

[9] Ahzi, S., and M'Guil, S., 2005. "Simulation of Deformation Texture Evolution Using an Intermediate Model." *Solid State Phenomena,* **105**(July), pp. 251–258. 4, 27

[10] Takahashi, R., Prasai, D., Adams, B. L., and Mattson, C. A., 2012. "Hybrid Bishop-Hill Model for Elastic-Yield Limited Design With Non-Orthorhombic Polycrystalline Metals." *Journal of Engineering Materials and Technology,* **134**(1), p. 011003. 4, 28, 41, 43, 46, 48, 60

[11] Adams, B. L., Kalidindi, S. R., and Fullwood, D. T., 2012, in press. *Microstructure Sensitive Design for Performance Optimization*. Butterworth-Heinemann. in press. 5, 6, 31, 32, 34, 61, 62, 64

[12] Fullwood, D. T., Niezgoda, S. R., Adams, B. L., and Kalidindi, S. R., 2010. "Microstructure Sensitive Design for Performance Optimization." *Progress in Materials Science,* **55**(6), Aug., pp. 477–562. 5, 6, 7, 8, 12, 13, 27, 32, 33, 34, 62, 63, 64

[13] Lekhnitskii, S. G., 1968. *Anisotropic Plates*., 1st ed. Gordon and Breach Science Publishers, New York. 5, 13, 28

[14] Bunge, H. J., 1982. *Texture Analysis in Materials Science: Mathematical Methods*. Butterworth-Heinemann, London. 6, 7, 32, 62

[15] Wright, S. I., Adams, B. L., and Kunze, K., 1993. "Application of a New Automatic Lattice Orientation Measurement Technique to Polycrystalline Aluminum." *Materials Science and Engineering: A,* **160**(2), pp. 229–240. 7, 32, 62

[16] Prager, W., and Hodge, P. G., 1968. *Theory of Perfectly Plastic Solids*. Dover, New York. 9

[17] Chin, G. Y., and Mammel, W. L., 1967. "Computer Solutions of the Taylor Analysis for Axisymmetric Flow." *Trans. Met. Soc. AIME,* **239**, pp. 1400–1405. 10

[18] Clausen, B., Leffers, T., Lorentzen, T., Pedersen, O. B., and Van Houtte, P., 2000. "The Resolved Shear Stress on the Non-Active Systems in Taylor/Bishop-Hill Models for FCC Polycrystals." *Scripta Materialia,* **42**, pp. 91–96. 10

[19] Adams, B. L., Nylander, C., Aydelotte, B., Ahmadi, S., Landon, C., Stucker, B. E., and Ram, G. D. J., 2008. "Accessing the Elastic-Plastic Properties Closure by Rotation and Lamination." *Acta Materialia,* **56**, pp. 128–139. 12, 13, 17, 48

[20] Kalidindi, S. R., Knezevic, M., Niezgoda, S., and Shaffer, J., 2009. "Representation of the Orientation Distribution Function and Computation of First-order Elastic Properties Closures Using Discrete Fourier Transforms." *Acta Materialia,* **57**(13), pp. 3916–3923. 12, 13, 32, 34, 62, 63

[21] Knezevic, M., and Kalidindi, S. R., 2007. "Fast Computation of First-Order Elastic-Plastic Closures for Polycrystalline Cubic-Orthorhombic Microstructures." *Computational Materials Science,* **39**(3), pp. 643–648. 12, 13, 32, 34, 62, 63

[22] Van Houtte, P., 1988. "A Comprehensive Mathematical Formulation of an Extended Taylor-Bishop-Hill Model Featuring Relaxed Constraints, the Renouard-Wintenberger Theory and a Strain Rate Sensitivity Model." *Textures and Microstructure,* **8-9**, pp. 313–350. 16

[23] Kocks, U. F., Tome, C. N., and Wenk, H.-R., 1998. *Texture and Anisotropy: Preferred Orientations in Polycrystals and their Effect on Materials Properties*. Cambridge University Press, New York. 19

[24] Ahzi, S., and M'Guil, S., 2008. "A New Intermediate Model for Polycrystalline Viscoplastic Deformation and Texture Evolution." *Acta Materialia,* **56**(19), pp. 5359–5369. 27

[25] Hutchinson, J. W., 1970. "Elastic-Plastic Behaviour of Polycrystalline Metals and Composites." *Proceedings of the Royal Society A: Mathematical, Physical and Engineering Sciences,* **319**(1537), pp. 247–272. 27

[26] Gambin, W., and Barlat, F., 1997. "Modeling of Deformation Texture Development Based on Rate Independent Crystal Plasticity." *International Journal of Plasticity,* **13**, pp. 75–85. 27

[27] Garmestani, H., Lin, S., Adams, B. L., and Ahzi, S., 2001. "Statistical Continuum Theory for Large Plastic Deformation of Polycrystalline Materials." *Journal of the Mechanics and Physics of Solids,* **49**, pp. 589–607. 27

[28] Delannay, L., Kalidindi, S. R., and Van Houtte, P., 2002. "Quantitative Prediction of Textures in Aluminium Cold Rolled to Moderate Strains." *Materials Science and Engineering: A,* **336**, pp. 233–244. 27

[29] Kalidindi, S. R., Duvvuru, H. K., and Knezevic, M., 2006. "Spectral Calibration of Crystal Plasticity Models." *Acta Materialia,* **54**(7), pp. 1795–1804. 27, 59

[30] Beaudoin, A. J., Dawson, P. R., Mathur, K. K., and Kocks, U., 1995. "A Hybrid Finite Element Formulation for Polycrystal Plasticity With Consideration of Macrostructural and Microstructural Linking." *International Journal of Plasticity,* **11**(5), pp. 501–521. 27, 59

[31] Van Houtte, P., Li, S., Seefeldt, M., and Delannay, L., 2005. "Deformation Texture Prediction: From The Taylor model to The Advanced Lamel Model." *International Journal of Plasticity,* **21**(3), pp. 589–624. 27

[32] Jacobsen, J. O., Chen, G., Howell, L. L., and Magleby, S. P., 2009. "Lamina Emergent Torsional (LET) Joint." *Mechanism and Machine Theory,* **44**(11), pp. 2098–2109. 30

[33] Wilding, S. E., Howell, L. L., and Magleby, S. P., 2012. "Introduction of Planar Compliant Joints Designed for Combined Bending and Axial Loading Conditions in Lamina Emergent Mechanisms." *Mechanism and Machine Theory,* **56**, pp. 1–15. 30

[34] Hill, R., 1952. "The Elastic Behaviour of a Crystalline Aggregate." *Proceedings of the Physical Society. Section A,* **65**(5), May, pp. 349–354. 32, 62

[35] Taylor, G. I., 1934. "The Mechanism of Plastic Deformation of Crystals. Part I. Theoretical." *Proceedings of the Royal Society of London. Series A,* **145**(855), pp. 362–387. 41, 59

[36] Przybyla, C. P., Adams, B. L., and Miles, M. P., 2007. "Methodology for Determining the Variance of the Taylor Factor: Application in Fe-3%Si." *Journal of Engineering Materials and Technology,* **129**(1), p. 82. 41

[37] Harston, S. P., and Mattson, C. A., 2010. "Metrics for Evaluating the Barrier and Time to Reverse Engineer a Product." *Journal of Mechanical Design,* **132**, p. 9. 54

[38] Proust, G., and Kalidindi, S., 2006. "Procedures for Construction of Anisotropic Elastic-Plastic Property Closures for Face-Centered Cubic Polycrystals Using First-Order Bounding Relations." *Journal of the Mechanics and Physics of Solids,* **54**(8), pp. 1744–1762. 59

[39] Bronkhorst, C. A., Kalidindi, S. R., and Anand, L., 1992. "Polycrystalline Plasticity and the Evolution of Crystallographic Texture in FCC Metals." *Philosophical Transactions of the Royal Society A: Mathematical, Physical and Engineering Sciences,* **341**(1662), pp. 443–477. 59

[40] Van Houtte, P., Delannay, L., and Kalidindi, S. R., 2002. "Comparison of Two Grain Interaction Models for Polycrystal Plasticity and Deformation Texture Prediction." *International Journal of Plasticity,* **18**, pp. 359–377. 59

[41] Knezevic, M., Kalidindi, S. R., and Fullwood, D. T., 2008. "Computationally Efficient Database and Spectral Interpolation for Fully Plastic Taylor-Type Crystal Plasticity Calculations of Face-Centered Cubic Polycrystals." *International Journal of Plasticity,* **24**(7), pp. 1264–1276. 59

[42] Knezevic, M., Al-Harbi, H. F., and Kalidindi, S. R., 2009. "Crystal Plasticity Simulations Using Discrete Fourier Transforms." *Acta Materialia,* **57**(6), pp. 1777–1784. 59

[43] Fromm, B. S., Adams, B. L., Ahmadi, S., and Knezevic, M., 2009. "Grain Size and Orientation Distributions: Application to Yielding of α -titanium." *Acta Materialia,* **57**(8), pp. 2339–2348. 59

[44] Kocks, U. F., and Mecking, H., 2003. "Physics and Phenomenology of Strain Hardening: the FCC case." *Progress in Materials Science,* **48**, pp. 171–273. 59, 65

[45] Nix, W. D., and Gao, H., 1998. "Indentation Size Effects in Crystalline Materials: A Law for Strain Gradient Plasticity." *Journal of the Mechanics and Physics of Solids,* **46**(3), pp. 411–425. 59

[46] Gao, H., Hugan, Y., Nix, W. D., and Hutchinson, J. W., 1999. "Mechanism-Based Strain Gradient Plasticity - I. Theory." *Journal of the Mechanics and Physics of Solids,* **47**, pp. 1239–1263. 60

[47] Kysar, J. W., Saito, Y., Oztop, M. S., Lee, D., and Huh, W. T., 2010. "Experimental Lower Bounds on Geometrically Necessary Dislocation Density." *International Journal of Plasticity,* **26**(8), pp. 1097–1123. 65, 67

[48] Nye, J. F., 1953. "Some Geometrical Relations in Dislocated Crystals." *Acta Materialia,* **1**, pp. 153–162. 65

[49] Kroner, E. A., 1958. "Continuum theory of dislocations and self-stresses." *Ergebnisse der Angewandten Mathematik,,* **5**, pp. 1327–1347. 65, 66

[50] Kacher, J., Landon, C., Adams, B. L., and Fullwood, D., 2009. "Bragg's Law Diffraction Simulations for Electron Backscatter Diffraction Analysis." *Ultramicroscopy,* **109**(9), pp. 1148–56. 65, 67

[51] Pantleon, W., 2008. "Resolving the Geometrically Necessary Dislocation Content by Conventional Electron Backscattering Diffraction." *Scripta Materialia,* **58**(11), pp. 994–997. 65, 66

[52] Gardner, C. J., Kacher, J., Basinger, J., Adams, B. L., Oztop, M. S., and Kysar, J. W., 2010. "Techniques and Applications of the Simulated Pattern Adaptation of Wilkinson's Method for Advanced Microstructure Analysis and Characterization of Plastic Deformation." *Experimental Mechanics,* **51**(8), pp. 1379–1393. 66, 67

[53] Basinger, J., 2011. "Detail extraction from electron backscatter diffraction patterns." PhD Dissertation, Brigham Young University, Provo, UT, December. 66, 67

[54] Ruggles, T. J., and Fullwood, D. T., 2011, submitted. "Estimation of Bulk Geometrically Necessary Dislocation Density Using High Resolution EBSD.". 66, 67

[55] Fullwood, D. T., Adams, B. L., Basinger, J., Ruggles, T. J., Khosravani, A., Sorensen, C., and Kacher, J., 2012, in press. *Microstructure Detail Extraction via EBSD*. Imperial College Press. 66, 67

[56] Wilkinson, A. J., Meaden, G., and Dingley, D. J., 2006. "High-Resolution Elastic Strain Measurement from Electron Backscatter Diffraction Patterns: New Levels of Sensitivity." *Ultramicroscopy,* **106**(4-5), pp. 307–13. 67

[57] Wright, S. I., Nowell, M. M., and Field, D. P., 2011. "A Review of Strain Analysis Using Electron Backscatter Diffraction." *Microscopy Microanalysis,* **17**(3), pp. 316–29. 67

[58] Gardner, C. J., Adams, B. L., Basinger, J., and Fullwood, D. T., 2010. "EBSD-Based Continuum Dislocation Microscopy." *International Journal of Plasticity,* **26**(8), pp. 1234–1247. 67

[59] Wilkinson, A. J., Meaden, G., and Dingley, D. J., 2006. "High Resolution Mapping of Strains and Rotations Using Electron Backscatter Diffraction." *Materials Science and Technology,* **22**(11), pp. 1271–1278. 67

[60] Adams, B. L., and Kacher, J., 2009. "EBSD-Based Microscopy Resolution of Dislocation Density." *Computers, Materials and Continua,* **14**(3), pp. 185–196. 67

[61] Field, D. P., Merriman, C. C., Allain-Bonasso, N., and Wagner, F., 2012. "Quantification of Dislocation Structure Heterogeneity in Deformed Polycrystals by EBSD." *Modelling and Simulation in Materials Science and Engineering,* **20**(2), p. 024007. 73

APPENDIX A. POLE FIGURES FOR THE DATABASE

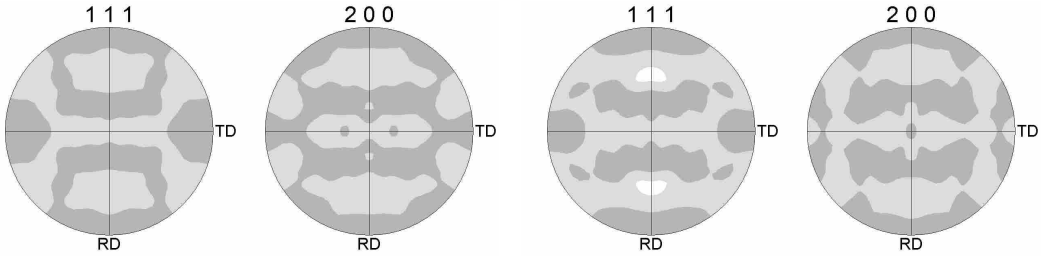

(a) As-received
Maximum intensity: 1.639×random

(b) As-received and annealed
Maximum intensity: 1.748×random

Figure A.1: As-received samples

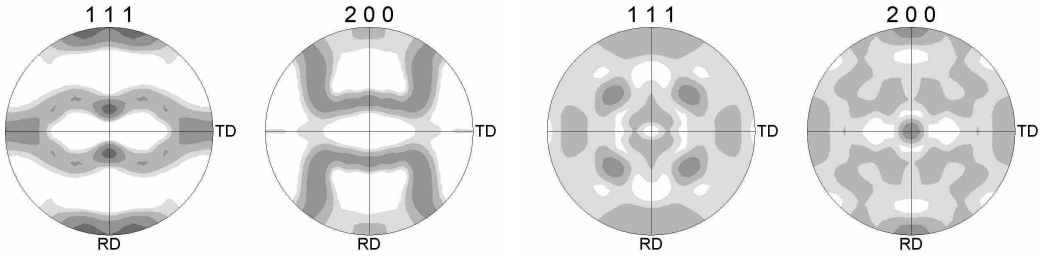

(a) 98% cold worked
Maximum intensity: 5.534×random

(b) 98% cold worked and recrystallized
Maximum intensity: 3.714×random

Figure A.2: 98% cold worked samples

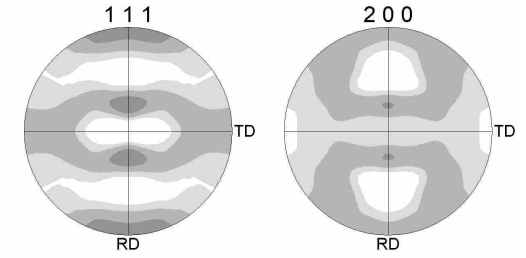

(a) 58% cold worked
Maximum intensity: 3.390×random

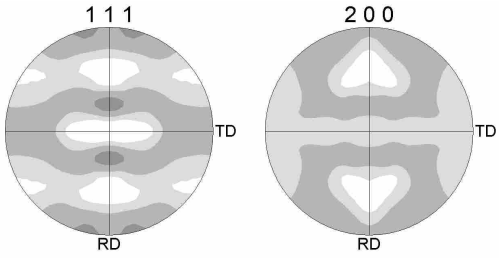

(b) 58% cold worked and annealed
Maximum intensity: 2.827×random

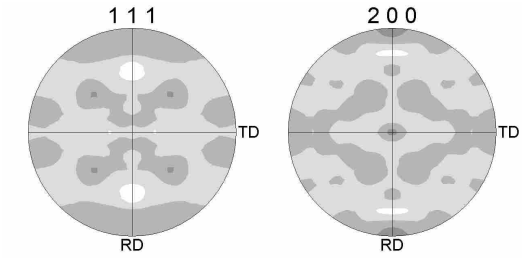

(c) 58% cold worked and recrystallized
Maximum intensity: 2.816×random

Figure A.3: 58% cold worked samples

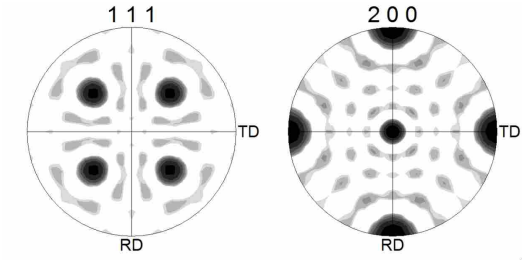

(a) Maximum intensity: 36.796×random

Figure A.4: Cube texture sample

APPENDIX B. TBH CORNER STRESS STATES

Table B.1: TBH corner stress states

	σ^c_{11}	σ^c_{22}	σ^c_{33}	σ^c_{23}	σ^c_{13}	σ^c_{12}
Corner 1	$\sqrt{6}\tau_{crss}$	$-\sqrt{6}\tau_{crss}$	0	0	0	0
Corner 2	0	$\sqrt{6}\tau_{crss}$	$-\sqrt{6}\tau_{crss}$	0	0	0
Corner 3	$-\sqrt{6}\tau_{crss}$	0	$\sqrt{6}\tau_{crss}$	0	0	0
Corner 4	0	0	0	$\sqrt{6}\tau_{crss}$	0	0
Corner 5	0	0	0	0	$\sqrt{6}\tau_{crss}$	0
Corner 6	0	0	0	0	0	$\sqrt{6}\tau_{crss}$
Corner 7	$\frac{\sqrt{6}}{2}\tau_{crss}$	$-\sqrt{6}\tau_{crss}$	$\frac{\sqrt{6}}{2}\tau_{crss}$	0	$\frac{\sqrt{6}}{2}\tau_{crss}$	0
Corner 8	$\frac{\sqrt{6}}{2}\tau_{crss}$	$-\sqrt{6}\tau_{crss}$	$\frac{\sqrt{6}}{2}\tau_{crss}$	0	$-\frac{\sqrt{6}}{2}\tau_{crss}$	0
Corner 9	$-\sqrt{6}\tau_{crss}$	$\frac{\sqrt{6}}{2}\tau_{crss}$	$\frac{\sqrt{6}}{2}\tau_{crss}$	$\frac{\sqrt{6}}{2}\tau_{crss}$	0	0
Corner 10	$-\sqrt{6}\tau_{crss}$	$\frac{\sqrt{6}}{2}\tau_{crss}$	$\frac{\sqrt{6}}{2}\tau_{crss}$	$-\frac{\sqrt{6}}{2}\tau_{crss}$	0	0
Corner 11	$\frac{\sqrt{6}}{2}\tau_{crss}$	$\frac{\sqrt{6}}{2}\tau_{crss}$	$-\sqrt{6}\tau_{crss}$	0	0	$\frac{\sqrt{6}}{2}\tau_{crss}$
Corner 12	$\frac{\sqrt{6}}{2}\tau_{crss}$	$\frac{\sqrt{6}}{2}\tau_{crss}$	$-\sqrt{6}\tau_{crss}$	0	0	$-\frac{\sqrt{6}}{2}\tau_{crss}$
Corner 13	$\frac{\sqrt{6}}{2}\tau_{crss}$	0	$-\frac{\sqrt{6}}{2}\tau_{crss}$	$\frac{\sqrt{6}}{2}\tau_{crss}$	0	$\frac{\sqrt{6}}{2}\tau_{crss}$
Corner 14	$\frac{\sqrt{6}}{2}\tau_{crss}$	0	$-\frac{\sqrt{6}}{2}\tau_{crss}$	$-\frac{\sqrt{6}}{2}\tau_{crss}$	0	$\frac{\sqrt{6}}{2}\tau_{crss}$
Corner 15	$\frac{\sqrt{6}}{2}\tau_{crss}$	0	$-\frac{\sqrt{6}}{2}\tau_{crss}$	$\frac{\sqrt{6}}{2}\tau_{crss}$	0	$-\frac{\sqrt{6}}{2}\tau_{crss}$
Corner 16	$\frac{\sqrt{6}}{2}\tau_{crss}$	0	$-\frac{\sqrt{6}}{2}\tau_{crss}$	$-\frac{\sqrt{6}}{2}\tau_{crss}$	0	$-\frac{\sqrt{6}}{2}\tau_{crss}$
Corner 17	0	$-\frac{\sqrt{6}}{2}\tau_{crss}$	$\frac{\sqrt{6}}{2}\tau_{crss}$	0	$\frac{\sqrt{6}}{2}\tau_{crss}$	$\frac{\sqrt{6}}{2}\tau_{crss}$
Corner 18	0	$-\frac{\sqrt{6}}{2}\tau_{crss}$	$\frac{\sqrt{6}}{2}\tau_{crss}$	0	$-\frac{\sqrt{6}}{2}\tau_{crss}$	$\frac{\sqrt{6}}{2}\tau_{crss}$
Corner 19	0	$-\frac{\sqrt{6}}{2}\tau_{crss}$	$-\frac{\sqrt{6}}{2}\tau_{crss}$	0	$\frac{\sqrt{6}}{2}\tau_{crss}$	$-\frac{\sqrt{6}}{2}\tau_{crss}$
Corner 20	0	$-\frac{\sqrt{6}}{2}\tau_{crss}$	$-\frac{\sqrt{6}}{2}\tau_{crss}$	0	$-\frac{\sqrt{6}}{2}\tau_{crss}$	$-\frac{\sqrt{6}}{2}\tau_{crss}$
Corner 21	$-\frac{\sqrt{6}}{2}\tau_{crss}$	$\frac{\sqrt{6}}{2}\tau_{crss}$	0	$\frac{\sqrt{6}}{2}\tau_{crss}$	$\frac{\sqrt{6}}{2}\tau_{crss}$	0
Corner 22	$-\frac{\sqrt{6}}{2}\tau_{crss}$	$\frac{\sqrt{6}}{2}\tau_{crss}$	0	$-\frac{\sqrt{6}}{2}\tau_{crss}$	$\frac{\sqrt{6}}{2}\tau_{crss}$	0
Corner 23	$-\frac{\sqrt{6}}{2}\tau_{crss}$	$\frac{\sqrt{6}}{2}\tau_{crss}$	0	$\frac{\sqrt{6}}{2}\tau_{crss}$	$-\frac{\sqrt{6}}{2}\tau_{crss}$	0
Corner 24	$-\frac{\sqrt{6}}{2}\tau_{crss}$	$\frac{\sqrt{6}}{2}\tau_{crss}$	0	$-\frac{\sqrt{6}}{2}\tau_{crss}$	$-\frac{\sqrt{6}}{2}\tau_{crss}$	0
Corner 25	0	0	0	$\frac{\sqrt{6}}{2}\tau_{crss}$	$\frac{\sqrt{6}}{2}\tau_{crss}$	$-\frac{\sqrt{6}}{2}\tau_{crss}$
Corner 26	0	0	0	$\frac{\sqrt{6}}{2}\tau_{crss}$	$-\frac{\sqrt{6}}{2}\tau_{crss}$	$\frac{\sqrt{6}}{2}\tau_{crss}$
Corner 27	0	0	0	$-\frac{\sqrt{6}}{2}\tau_{crss}$	$\frac{\sqrt{6}}{2}\tau_{crss}$	$\frac{\sqrt{6}}{2}\tau_{crss}$
Corner 28	0	0	0	$\frac{\sqrt{6}}{2}\tau_{crss}$	$\frac{\sqrt{6}}{2}\tau_{crss}$	$\frac{\sqrt{6}}{2}\tau_{crss}$